



Macêdo, R. (2016) Tunable optical effects in natural hyperbolic magnetic media. PhD thesis.

<http://theses.gla.ac.uk/8147/>

Copyright and moral rights for this work are retained by the author

A copy can be downloaded for personal non-commercial research or study, without prior permission or charge

This work cannot be reproduced or quoted extensively from without first obtaining permission in writing from the author

The content must not be changed in any way or sold commercially in any format or medium without the formal permission of the author

When referring to this work, full bibliographic details including the author, title, awarding institution and date of the thesis must be given

Enlighten:Theses
<http://theses.gla.ac.uk/>
theses@gla.ac.uk

Tunable Optical Effects in Natural Hyperbolic Magnetic Media

R. Macêdo

Presented as a thesis for the
degree of Ph.D.



University
of Glasgow

Materials and Condensed Matter Physics Group
School of Physics and Astronomy
University of Glasgow
United Kingdom

August 2016

<i>"Das muitas coisas</i>	[From the many things]
<i>Do meu tempo de criança</i>	[of my childhood time]
<i>Guardo vivo na lembrança</i>	[I still vividly remember]
<i>O aconchego de meu lar</i>	[the warmth of my house]
<i>No fim da tarde</i>	[after the sunset]
<i>Quando tudo se aquietava</i>	[and it went quiet outside]
<i>A família se ajuntava</i>	[my family all gathered]
<i>Lá no alpendre a conversar</i>	[talking on the porch]
<i>Meus pais não tinham</i>	[my parents didn't have]
<i>Nem escola, nem dinheiro</i>	[money or education]
<i>Todo dia, o ano inteiro</i>	[everyday, the whole year]
<i>Trabalhavam sem parar</i>	[working, nonstop!]
<i>Faltava tudo</i>	[material things lacked]
<i>Mas a gente nem ligava</i>	[But we didn't care]
<i>O importante não faltava</i>	[the most important thing we had]
<i>Seu sorriso, seu olhar</i>	[their smile and peaceful 'eyes']
[. . .]	[. . .]
<i>Correu o tempo</i>	[Time has passed]
<i>Hoje eu vejo a maravilha</i>	[now I see the wonders]
<i>De se ter uma família</i>	[of having a family]
<i>Quando tantos não a tem [. . .] "</i>	[when so many don't...]

— Pe. Zezinho, *Utopia* (Granny's favourite song)

To my family, for all the unconditional love and support they have always given me. When times were hard, they were there to hold my hand and help me to pull through. I would not be who I am or (and) where I am without them!

Acknowledgements

"I would like to thank the judges for picking me, my parents who I love...I love you Houston!"

I would like to deeply express my gratitude to Professor Stamps, who has supervised me during my PhD, always believing in me and pushing me to do things I never thought I could do. During this work he trained my mind with his brilliant thoughts and was always friendly with such natural kindness. Some may take this for granted, but I do not, and will always be thankful for his thoughtfulness. I would also like to thank Professor Dumelow, and I don't even know where to start. He believed in me, a 15 year old kid, almost ten years ago when I was in my first weeks of my BSc. I will never forget the afternoons in the lab talking about the UK - back then not even thinking I'd be here one day. Even though I always asked far too many stupid questions he always answered them all and done so with a big smile on his face.

I am very grateful the UERN. The research office as well as the registration office, in special Ismael Nobre, were always there to sort out admin problems, specially to help me graduate in time to start my PhD. Also the Physics Department staff, such as Prof. Fabio Cabral whose hardest lectures were the ones wherein I learned the most. I also have much to thank to Prof. Joao Maria who always motivated me to pursue science and Prof. Alzamir Costa who always made fun of everything and anything, but when times got rough he was always there to help us out in any way he could.

During my time at the LAMOP (UERN) I made amazing friends such as Rizia Rodrigues who gave me the best career advice ever, which was to always trust and follow Prof. Dumelow, and thanks to that here I am. Also Meirielle Marques who unwittingly taught me very important life lessons: *"Dreaming is believing"* and *"it's okay not to be okay"*. Also from that university, Joao Neto, Icaro Kennedy, Laysa Glicia, Vanessao e Mackson, Nega Jú, as Danis and Mayarinha. I will always remember our nights out and our nights in studying for exams. I could not forget my Math's pals Suyanne, Kleilton, Kel, Franciara, Josi (who's always been an inspiration to me) and Fatinha (who's theorem I used so many times in the makings of this thesis and will keep using in my academic career).

Also thank you to the UFERSA girls: Jusciane Costa who is as good a driver as Beyonce is a good singer. Having said that, she taught me a lot about semiconductors and by example - among many things - she taught me that there are people in the world who are naturally kind and will help you in any way they can, without expecting anything in return. Subenia Karine with whom I had several useful discussions and delightful conversations and Luciana Angelica and Teresa Abreu who gave me many lifts from Mossoró to Fortaleza. These may have seemed like effortless favours to them, but those lifts helped me immeasurably. This also enabled me to have wonderful discussions with Andrey Chaves, to who I could not thank enough. Always very patient, he gave me a desk in his office and I annoyed the life out of him but learnt so much in those afternoons.

I am extremely grateful to the University of Glasgow for all the help and support through the years, in special Heather Lambie and her team, always having believed in me - since the very beginning. It was, most certainly, due to their helpful emails -always extremely kind - that I have chosen this University and due to their continuous support and lovely words, there has not been a day in which I regretted that decision. At the University of Glasgow I have also met some great people who helped me through my PhD: the girls from 408 - Monifa and Yue (and Ray) who have always been extremely kind and put a smile on anyone's face, the guys from 402 - Shabir who initially showed me around the UofG and the West End and Francisco who helped me in so many aspects of my PhD, including reminding me that Portuguese is my first language, Scott from 409 who helped

me so many times with maths and my favourite Geordie - Cheryl Cole oops no...Becky who not only proofread my manuscripts and reports but was always up for nice chats over drinks. I have also had great technical help from Colin How downstairs who's always helped me with my IT stupidity, and done so with a big smile. I could not forget Lucy Murray, who I cannot thank enough for the numerous forms and conference claims she helped me with. Without her I would also never have located my supervisor and probably not have a thesis by now.

I have no words to express my gratitude to the MacQuarrie Family. They were of great help, even before I arrived in Scotland when John helped me with my English. Later his father, Alan, welcomed me to this county and brought me into his home with open arms and gave me a place to stay in Andrew's room (who's John's brother, thanks Andrew!). I will never forget all the Christmases, Easters and family dinners I have had with you all, or the most enjoyable teas/wine with Susan and Anne as well. You all truly made feel welcome in this country and in your family. You are my new found Scottish family, and for that I will always be very thankful.

I would also like to thank some people who have been supporting me since very early in life back in my home town, such as my best pal from primary school Jefferson, always backing me up and we always had a great laugh. Also to Lidianne and her family, who have been there for me ever since our juvenile problems in church groups and to dinha Lila and her family (her parents being my God parents) who always had kind words for me and lovely smiles. The lovely Jakeline and Cybelle for the movies and popcorn nights in as well as the bonfires and crazy cocktails. Not only my dentist, but school friend and chemistry teacher Maurilia who alongside her family have supported me in so many ways throughout the years I cannot even begin to list them all. Also to the crazy crew from the "Pousada" especially Fabiola and Ruxley, who always believed in me and literally sent me on my way to higher education. It is also suitable here to thank Jussara and family as well as Madrinha Socorro and her family for all the support and nice chats along the way. I also could not forget Marianne and Layanne who were always my little bit of home town in Mossoró. Still, I will never forgive you two for my stolen bike. Also thank you to Ricardo e Roberto (from my hometown) who gave me a place to stay when I started Uni and were always there with words of encouragement. Thank you all!

I would also like to thank Kirsty Annand. We have come such a long way over the years and she has become like a sister to me. I cannot image going one day in this building without her. She is the one I go to when I need advice, and even though I don't listen most of the time, I feel so pleased that I have learnt a lot of important things from her - such as the pronunciation of Mary, Marry and Merry. In fact, most of the longest words I know have come from her. Thank you June.

Thank you Veruskinha Benevides - the feistiest young woman I have ever met! We died and came back to life together, ate pasta and sardines so many times. We spent so many sleepless nights awake in the LAMOp studying for exams, but we also spent days having fun in Caraúbas, making tapioca and riding motorcycles. We have been there for one another during so many tough times and she always made me believe in myself, she truly lifts me up when I am down. You are the best!

I would also have to thank here Stephen Orr, for not only having proofread this thesis several times but most importantly for, unknowingly, having kept me sane through the pressure of writing up - plus starting new job. Albeit stressful, it was a time full of hilarious stories, laughter and constant mispronunciation of common words.

Finally, *"It's taken a lot of hard work to get to where I am and I searched all around the world and I found myself. Y'all are my inspiration"* and this thesis is thus a contribution of all of you guys so **Thank You**.

“ [. . .]

I was here, I lived, I loved, I was here

I did, I've done, everything that I wanted

And it was more than I thought it would be . . .

I just want them to know

That I gave my all, did my best

Brought someone some happiness

Left this world a little better just because, I was here

[. . .]”

— Beyoncé Knowles, *I was here*

Abstract

Anisotropic media have been the object of study in the fields of optics and photonics for decades. More recently, we have seen the emergence of a new class of anisotropic materials, the so-called hyperbolic media. These new structures rapidly gained attention for displaying several optical effects such as all-angle negative refraction with low loss.

This thesis presents a theoretical investigation of anisotropic magnetic crystals working as hyperbolic media. These type of structures are not often associated with hyperbolic behaviour. The aim is to show that magnetic crystals are not only an alternative way to obtain hyperbolic dispersion but that they can also be controlled by externally applied fields. The general theory is applied to manganese fluoride (MnF_2), a reasonably well studied antiferromagnet, in a configuration in which spins cant in response to applied magnetic fields. The work can be divided into three main strands.

The first is to treat the surface reflection and illustrate how light beams can be laterally shifted from the position predicted by geometrical optics i.e., the so called Goos-Hänchen effect. In antiferromagnets these shifts can be controlled with an external magnetic field. Moreover, the possibility of nonreciprocal displacements is investigated, for both oblique and normal incidence, due to an inherent nonreciprocity of the polariton phase with respect to the propagation direction. Reciprocal displacements are also studied in the absence of an external field.

The second strand of the work is a study of how all-angle negative refraction can occur in a uniaxial antiferromagnet close to the magnon resonance frequency. This behavior is based on the fact that, in such cases, the antiferromagnet acts as an indefinite permeability medium, i.e., not all its permeability tensor components are of the same sign. If an external magnetic field is applied, the angle of refraction becomes tunable, and can be made to change sign.

The final part of this work proposes tunable slab lensing in natural magnetic media using an externally applied magnetic field. Natural hyperbolic magnetic materials not only display imaging obtained from slab lenses with plane parallel sides but also allow one to modify the focal length of a slab lens with an externally

applied magnetic field. This is possible because antiferromagnets are gyrotropic and support magnetic polaritons whose frequencies are sensitive to magnetic fields. In addition, an investigation of the caustic formation in this type of lenses is presented for low temperatures, when damping should be small. Slab focusing is also studied at higher temperatures.

Declaration

This thesis has been written by myself and details the research I have carried out in the Materials and Condensed Matter Physics (MCMP) group of the School of Physics and Astronomy at the University of Glasgow under the supervision of Prof. Robert L. Stamps and Prof. T. Dumelow. The work discussed here is my own and some of the work reported in this thesis can be found in the following papers:

- R. Macêdo and T. Dumelow. Tunable all-angle negative refraction using antiferromagnets. *Physical Review B* 89, 035135 (2014).
- R. Macêdo, R. L. Stamps and T. Dumelow. Spin canting induced nonreciprocal Goos-Hänchen shifts. *Optics Express* 22, 28467 (2014).
- R. Macêdo, R. L. Stamps and T. Dumelow. Tunable magneto-optical Effects in Antiferromagnetic structures. *Advanced Electromagnetic Materials in Microwaves and Optics IEEE*, 454 (2015).
- R. Macêdo, T. Dumelow and R. L. Stamps. Tunable focusing in natural hyperbolic magnetic media. *ACS Photonics* (2016).
- R. Macêdo, R. L. Stamps and T. Dumelow. Orientation dependence on the focusing by hyperbolic media. *In progress*.

Copyright © 2016.

“The copyright of this thesis rests with the author. No quotations from it should be published without the author’s prior written consent and information derived from it should be acknowledged”.

Contents

Acknowledgements	iv
Abstract	viii
Declaration	xi
1 Introduction	1
1.1 Hyperbolic media	3
1.1.1 Indefinite permittivity and its properties	3
1.2 Phenomena	5
1.2.1 Goos-Hänchen shifts	5
1.2.2 Negative refraction	7
1.2.3 Slab lenses and focusing	8
1.3 Realisation of hyperbolic media	9
1.3.1 Hyperbolic metamaterials	10
1.3.2 Anisotropic single crystals	10
1.4 Objectives of the work	11
1.5 Structure of this Thesis	12
2 Magnetic Polaritons and Indefinite Permeability	13
2.1 Antiferromagnetic Crystals	14
2.2 Antiferromagnetic resonance	16
2.2.1 The indefinite permeability tensor	19
2.3 Field Driven Spin Canting	20
2.3.1 External Field and the Permeability Tensor	23
2.4 Magnetic polaritons	24
2.4.1 Dispersion Relation	25
2.5 Damping Effects	31

2.5.1	Damping temperature dependence	32
3	Spin canting induced Goos-Hänchen shifts	35
3.1	Reflection and Goos-Hänchen shifts	36
3.2	Zero field Goos-Hänchen shifts	38
3.3	Tunable shifts with $\mathbf{B}_0 \neq \mathbf{0}$	42
3.3.1	Oblique incidence	44
3.3.2	Normal incidence	46
3.4	Conclusions	49
4	Antiferromagnets as Negative Refractive Media	51
4.1	Indefinite permeability tensor	52
4.1.1	Hyperbolic dispersion	53
4.2	Power Flow Analysis	55
4.3	Effects of externally applied fields	58
4.4	Snell's Law and Negative Refraction	61
4.4.1	Effective index of refraction in Antiferromagnets	62
4.5	Figure of Merit	63
4.6	Nonreciprocity	64
4.7	Conclusion	66
5	Tunable Focusing	67
5.1	Hyperbolic dispersion	68
5.1.1	Refraction of a Gaussian Beam through an Antiferromagnetic Slab	69
5.2	Image formation in the paraxial limit	71
5.3	Caustics and field tunable focusing	74
5.4	Conclusion	76
6	Easy Axis Orientation Dependence	79
6.1	Easy axis transformation	80
6.2	Rotated Hyperbolic dispersion	81
6.3	Implications on the angle of refraction	82
6.4	Orientation dependence on focusing	85

6.5	Concluding Remarks	86
7	Conclusions and Open Questions	89
7.1	Summary of this thesis	89
7.2	Outlook	91
7.2.1	Subwavelength Imaging	91
7.2.2	Depth Probe Possibilities	92
7.2.3	Other Systems to be Investigated	93
	Appendices	95
A	On the Reflectivity off a semi-infinite Antiferromagnet	97
A.1	Boundary Conditions	97
B	On the Transmission Across an Antiferromagnet Film	103
B.1	Boundary Conditions	103
B.2	Transfer Matrix	105
C	On the Parameters used	107
D	On the Intensity profile Claculations	109
D.1	Semi-infinite crystal	109
D.2	Finite slab	110
D.2.1	Line point source	111
D.2.2	Goos-Hänchen shift on reflection of a finite beam	112
E	On the Power Flow	115

List of Tables

2.1	Physical parameters for antiferromagnets	20
-----	--	----

List of Figures

1.1	Isofrequency curve and relative direction of the wave vector \mathbf{k} and the Poynting vector \mathbf{S} for (a) isotropic material, (b) material with $\epsilon_{xx}\epsilon_{zz} > 0$, and (c) material with $\epsilon_{xx}\epsilon_{zz} < 0$	5
1.2	Schematic diagram of the Goos-Hänchen shift i.e., the lateral displacement, D , of a bounded beam at an interface. The dashed lines show the boundaries of the reflected beam as predicted by geometrical optics theory. (a) Positive and (b) negative displacements.	6
1.3	Directions of wavevectors and Poynting vectors for p-polarisation refraction at an interface between air and a uniaxial medium with $\epsilon_{xx} > 0, \epsilon_{zz} < 0$. (b) Corresponding instantaneous field profile for a gaussian beam.	7
1.4	(a) Image formation by a conventional convex lens, (b) image formation from a negative-index flat lens and (c) image formation from a slab lens made of a hyperbolic medium. Directions of wavevector is show in blue arrows and the Poynting vector is shown in red arrows.	8
2.1	Chemical arrangement of a simple antiferromagnet such as in manganese flouride (MnF_2) crystals with body-centred tetragonal structure: (a) perspective view and (b) side view.	15
2.2	Equilibrium spin orientation for uniaxial antiferromagnet, with antiparallel precession in the absence of an externally applied field.	17
2.3	μ_{zz} for an MnF_2 crystal calculated using the values given in table 2.1.	19
2.4	Disturbed spin orientation for uniaxial antiferromagnet by an externally applied field \mathbf{B}_0 inducing spin canting of the antiparallel precession magnetisations.	22

- 2.5 (a) $\text{Re}(\mu_{zz})$, (b) $\text{Re}(\mu_{xx})$ and (c) $\text{Im}(\mu_{xz})$. Solid curve: ($\mathbf{B}_0 = 0$); dashed curve ($\mathbf{B}_0 = 1.5$ T.) 24
- 2.6 Geometry considered in this work: The sublattice magnetisation and anisotropy fields are parallel to the surface and directed along $+x$ and $-x$ axes. The inset shows the spin anti-parallel arrangement in an antiferromagnetic slab. The incident radiation is considered to be transverse electric (TE) polarised. 26
- 2.7 Polariton dispersion relation around frequencies where the electromagnetic field of TM polarised radiation interacts with the spins of MnF_2 in the absence of an externally applied field. ω_0 is the resonance frequency and ω_s is the frequency where μ_{zz} vanishes. The shaded regions represent propagation inside the material and evanescent waves, without propagation, is seen elsewhere. 28
- 2.8 Polariton dispersion relation around frequencies where the electromagnetic field of TE-polarised radiation interacts with the spins of MnF_2 in the absence of an externally applied field. ω_0 is the resonance frequency and ω_s is the frequency where μ_{zz} vanishes. The shaded regions represent propagation inside the material and evanescent waves, without propagation, is seen elsewhere. 29
- 2.9 Polariton dispersion relation around frequencies where the electromagnetic field of s-polarised radiation interacts with the spins of MnF_2 in the presence of an externally applied field $\mathbf{B}_0 = 1.5$ T. ω_{\perp} is the resonance frequency and ω_s is the frequency where μ_{zz} vanishes. The shaded regions represent propagation inside the material and evanescent waves, without propagation, is seen elsewhere. 30
- 2.10 Effect of temperature induced damping on the real and imaginary parts of μ_{zz} around the magnon-polariton frequency in MnF_2 for (a) $0.06T_N$ and (b) $0.42T_N$ 32

- 3.1 Schematic representation of an oblique incident beam with an angle θ_1 being displaced on the reflection by a distance D at the interface between vacuum and an antiferromagnet, where S_i and S_r are the incident and reflected Poynting vector respectively. . . . 36
- 3.2 (a) Calculations of *s*-polarised oblique incidence ($\theta_1 = \pm 60^\circ$) reflection from the interface between vacuum and MnF_2 and (b) Goos-Hänchen shift D . Reflected (c) phase and (d) amplitude, as a function of in-plane wavevector k_x , at the frequency marked as A in (a) (9.0103 cm^{-1}) for the configuration shown in Fig. 3.1. Dashed lines are calculated for $\Gamma = 0$, whereas solid lines are for calculations in which $\Gamma = 0.0007 \text{ cm}^{-1}$. The shaded regions show where transmission is possible in the absence of damping. In case (a) the curves corresponding to $\theta_1 = \pm 60^\circ$ are coincident, so only a blue curve is seen in the case of the solid lines. Note that, in part (c), $\phi = \pi$ is represented as $\phi = -\pi$ in the $\Gamma = 0$ curve for consistency with the $\Gamma = 0.0007 \text{ cm}^{-1}$ curve. 40
- 3.3 Calculated overall power intensity (in terms of the magnitude of the time-averaged Poynting vector) showing intensities for a beam of width $g = 0.2 \text{ cm}$ obliquely incident ($\theta_1 = +60^\circ$) on a vacuum/ MnF_2 interface at the frequency marked as A in Fig. 3.2 (9.0103 cm^{-1}). The arrows represent the incident and reflected beams, positioned according to Eq. (3.3), with angle of reflection assumed equal to angle of incidence. 41
- 3.4 Goos-Hänchen shift D for different values of applied external field (a) $\mathbf{B}_0 = 0.0 \text{ T}$, (b) $\mathbf{B}_0 = 0.5 \text{ T}$, (c) $\mathbf{B}_0 = 1.0 \text{ T}$ and (d) $\mathbf{B}_0 = 1.5 \text{ T}$. Blue lines are calculated for $\theta_1 = +60^\circ$, whereas red lines are calculated for $\theta_1 = -60^\circ$ 43

- 3.5 (a) Calculations of *s*-polarised oblique incidence ($\theta_1 = \pm 60^\circ$) reflection from the interface between vacuum and MnF_2 in the presence of an external magnetic field of 1.5 T and (b) Goos-Hänchen shift *D*. Reflected (c) phase and (d) amplitude, as a function of in-plane wavevector k_x , at frequency marked as *B* (9.125 cm^{-1}) in (a). Dashed lines are calculated ignoring damping, whereas solid lines are for calculations in which damping is included. The shaded region shows frequencies where transmission can occur in the absence of damping. 44
- 3.6 Calculated overall power intensity (in terms of the magnitude of the time-averaged Poynting vector) showing intensities for a beam of width $g = 0.2 \text{ cm}$ obliquely incident on a vacuum/ MnF_2 interface at frequency *B* ($\omega = 9.125 \text{ cm}^{-1}$) in the presence of a magnetic field $B_0 = 1.5 \text{ T}$. (a) $\theta_1 = +60^\circ$; (b) $\theta_1 = -60^\circ$. The arrows represent the incident and reflected beams, positioned according to Eq. (3.3), with angle of reflection assumed equal to angle of incidence. . . . 46
- 3.7 Normal incidence calculations in the presence of an external magnetic field of 1.5 T. (a) Plane wave reflectivity spectrum; (b) Goos-Hänchen shift *D*. Reflected (a) phase and (b) amplitude, as a function of in-plane wavevector k_x , for *s*-polarised reflection from a MnF_2 crystal at the frequency marked in *C* as (a) (9.1204 cm^{-1}), in the presence of an external magnetic field of 1.5 T. Dashed lines are calculated ignoring damping, whereas solid lines are for calculations in which damping is included. The shaded regions show where transmission can occur in the absence of damping. . . 47
- 3.8 Intensity profiles of the incident (solid curve) and reflected (dashed curve) gaussian beam of width $g = 0.5 \text{ cm}$, at the frequency marked as *C* as Fig. 3.7 (9.1204 cm^{-1}), normally incident on MnF_2 in the presence of a magnetic field $B_0 = 1.5 \text{ T}$, with damping effects taken into account. The vertical solid line represents the center of the incident beam ($x = 0$) and the vertical dashed line represents the center of the reflected beam ($x = -0.04 \text{ cm}$). 48

- 4.1 Real part of μ_{zz} for an MnF_2 single crystal as a function of frequency (expressed in terms of ω_0) around the magnon-polariton resonance frequency. 53
- 4.2 Real parts of the wave-vector component k_{1z} (air) and k_{2z} (MnF_2) as a function of k_x for transmission in a MnF_2 crystal having its extraordinary axis directed along x . (a) Frequency A ($\omega/\omega_0 = 1.00$), (b) frequency B ($\omega/\omega_0 = 1.004$), (c) frequency C ($\omega/\omega_0 = 1.006$) and (c) frequency D ($\omega/\omega_0 = 1.008 = \omega_s$) 54
- 4.3 Angle of refraction θ_2 in MnF_2 for various angles of incidence from vacuum. 57
- 4.4 Contour plots showing intensities (in terms of the magnitude of the time-averaged Poyting vector) for a beam obliquely incident from vacuum on an MnF_2 crystal ($\theta_1 = 40^\circ$). (a) Frequency A ($\omega/\omega_0 = 1.00$), (b) frequency B ($\omega/\omega_0 = 1.004$), (c) frequency C ($\omega/\omega_0 = 1.006$) and (d) frequency D ($\omega/\omega_0 = 1.008 = \omega_s$). 57
- 4.5 Effect of various external applied fields \mathbf{B}_0 on the real part of μ_{zz} for an MnF_2 single crystal as a function of frequency (expressed in terms of ω_0) around the magnon-polariton resonance frequency. 58
- 4.6 Real parts of the wave-vector component k_{1z} (red lines) and k_{2z} (blue lines) as a function of k_x for transmission in a MnF_2 crystal having its extraordinary axis directed along x , at a frequency $\omega/\omega_0 = 1.004$ for (a) $B_0 = 0.0$, (b) $B_0 = 0.5$ T, (c) $B_0 = 1.0$ T and (d) $B_0 = 1.5$ T. 59
- 4.7 Angle of refraction θ_2 as a function of frequency in MnF_2 for an incident angle of $\theta_1 = 45^\circ$ 60
- 4.8 Intensity profile (time averaged power density) of a Gaussian beam obliquely incident at an angle of $\theta_1 = 45^\circ$, passing through an MnF_2 slab at frequency $\omega/\omega_0 = 1.004$ for (a) $B_0 = 0.0$, (b) $B_0 = 0.5$ T, (c) $B_0 = 1.0$ T and (d) $B_0 = 1.5$ T. 61

- 4.9 Angle of refraction θ_2 as a function of angle of incidence θ_1 . The red dashed line shows the behaviour of a medium with $n = -1$. (a) The solid line shows the angle of refraction calculated using Eq. 4.8 and the blue dashed line gives the result of using a paraxial approximation represented by Eq. 4.16 at the interface between air and a MnF_2 in the absence of an external field. (b) Effect of various external fields \mathbf{B}_0 on θ_2 in MnF_2 62
- 4.10 Figure of merite (FOM) as a function of applied field B_0 . Frequency X (8.98 cm^{-1}). 64
- 4.11 Angle of refraction θ_2 in MnF_2 as a function of applied field B_0 at frequency X (8.98 cm^{-1}). 65
- 5.1 Real part of μ_{zz} for an MnF_2 single crystal as a function of an externally applied field \mathbf{B}_0 varying from 0.0 to 2.5 T. 69
- 5.2 Real parts of the wave-vector component k_{1z} (blue lines) and k_{2z} (green lines) as a function of k_x (expressed in units of k_0), for transmission in a MnF_2 crystal having its extraordinary axis directed along x , in s-polarisation at a frequency $\omega/\omega_0 = 1.005$. (a) $B_0 = 0.0$, (b) $B_0 = 0.2 \text{ T}$ and (c) $B_0 = 0.4 \text{ T}$. Dashed lines: $T = 0.06 T_N$. Solid lines: $T = 0.42 T_N$ 70
- 5.3 Intensity profile (time averaged power density) of a Gaussian beam obliquely incident at an angle of incidence $\theta_1 = 45^\circ$, passing through an MnF_2 slab at frequency $\omega/\omega_0 = 1.005$ where $\omega_0 = 8.67 \text{ cm}^{-1}$ ($T = 0.06 T_N$). (a) $B_0 = 0.0$, (b) $B_0 = 0.2 \text{ T}$ and (c) $B_0 = 0.4 \text{ T}$. The intensity scale is in arbitrary units. 71
- 5.4 Path of a single ray from a source S passing through a slab of thickness d_2 72

- 5.5 (a) Schematic of focusing due to a source S placed above an MnF_2 slab in the absence of an external field ($B_0 = 0.0$). The incident angle is restricted to the range -10^0 to $+10^0$. The distance d_1 is equal to 0.25 cm and d_2 is equal to 1.0 cm. The extraordinary axis is directed along x and incident radiation at $\omega/\omega_0 = 1.005$. Effect of an externally applied magnetic field \mathbf{B}_0 are shown for (b) the effective index of refraction n_{eff} and (c) the image distance d 73
- 5.6 s-polarisation image formation at $T = 0.06 T_N$ due to a line source placed above an MnF_2 slab. The distance d_2 is $20\lambda'$ (≈ 1.0 cm), where λ' represents the wavelength within the antiferromagnet at normal incidence (about half the free-space wavelength). The distance d_1 is equal to $d_2/4$ (≈ 0.25 cm). The extraordinary axis is directed along x and the frequency of the incident radiation is $\omega/\omega_0 = 1.005$. (a) Schematic showing the path of multiple rays passing through an MnF_2 slab for $B_0 = 0.0$. (b) Power flow intensity for the setup shown in (a). Effect of a magnetic field on the intensity profile for (c) $B_0 = 0.2$ T and (d) $B_0 = 0.4$ T. The intensity scale is in arbitrary units. The intensity scale is in arbitrary units. 74
- 5.7 Calculation of transmittance as a function of incidence angle (θ_1) for an MnF_2 slab of thickness $d_2 = 20\lambda'$ (≈ 1.0 cm) whose easy axes lies along x . The incident radiation, at a frequency $\omega/\omega_0 = 1.005$, is s-polarised. (a) $B_0 = 0.0$, (b) $B_0 = 0.2$ T and (c) $B_0 = 0.4$ T. Dashed lines: $T = 0.06 T_N$. Solid lines: $T = 0.42 T_N$ 75
- 5.8 s-polarisation image formation at $T = 0.42 T_N$ due to a line source placed above of an MnF_2 slab. The distance d_2 is $20\lambda'$ (≈ 1.0 cm) and d_1 is equal to $d_2/4$ (≈ 0.25 cm). The extraordinary axis is directed along x and incident radiation at $\omega/\omega_0 = 1.005$. (a) Schematic showing the path of multiple rays passing through an MnF_2 slab for $B_0 = 0.0$. (b) Power flow intensity for the setup shown in (a). Effect of a magnetic field on the intensity profile for (c) $B_0 = 0.2$ T and (d) $B_0 = 0.4$ T. The intensity scale is in arbitrary units. 76

6.1 (a) Geometry of easy axis rotation along the xz plane by an angle φ . 80

6.2 Real parts of the wave-vector component k_{1z} (air) and k_{2z} (MnF_2) as a function of k_x for transmission in a MnF_2 crystal having its extraordinary axis rotated along the xz plane by (a)-(b) $\varphi = 0$, (c)-(d) $\varphi = 45^\circ$ and (e)-(f) $\varphi = 90^\circ$. The curves on the left hand-side are for a frequency below ω_0 and at the right hand-side we see frequencies above ω_0 83

6.3 Effect of a nonzero rotation angle φ on the angle of refraction θ_2 and a function of the incident angle θ_1 at (a) $\omega < \omega_0$ (b) $\omega_0 < \omega < \omega_s$. 84

6.4 Real parts of the wave-vector component k_{1z} (air) and k_{2z} (MnF_2) as a function of k_x for transmission in a MnF_2 crystal at a frequency $\omega < \omega_0$ having its extraordinary axis rotated along the xz plane by (a) $\varphi = 0$, (b) $\varphi = 10^\circ$ and (c) $\varphi = 20^\circ$ 85

6.5 Real parts of the wave-vector component k_{1z} (air) and k_{2z} (MnF_2) as a function of k_x for transmission in a MnF_2 crystal at a frequency $\omega_0 < \omega < \omega_s$ having its extraordinary axis rotated along the xz plane by (a) $\varphi = 0$, (b) $\varphi = 10^\circ$ and (c) $\varphi = 20^\circ$ 86

6.6 Schematic of Image formation due to a line source placed above of an MnF_2 slab at a frequency $\omega_0 < \omega < \omega_s$ having its extraordinary axis rotated along the xz plane by (a) $\varphi = 0$, (b) $\varphi = 10^\circ$ and (c) $\varphi = 20^\circ$ 86

7.1 (a) Real part of the principal component of the permeability tensor of MnF_2 around the magnon-polariton frequency. (b) Real part of the wavevector component k_{2z} as a function of k_x (expressed in units of k_0), for transmission in an MnF_2 crystal having its easy axes directed along x , at the resonance frequency ω_0 ($\omega/\omega_0 = 1.00$). (c) Schematic showing the general setup of imaging due to a two-slit source at the surface of a slab of MnF_2 at frequency ω_0 . . . 92

- A.1 Reflection geometry. The material occupies the lower half plane, $z > 0$, and the surface is in the xz plane. The saturation magnetisation is along x and the external field \mathbf{B}_0 is perpendicular to both the incidence plane and the easy axis (along y). The angle of incidence, θ_i , is the angle the wavevector of the incident wave makes with the normal to the surface. H_i and H_r represent the incident and reflected magnetic fields, respectively, which are polarized in the xz plane. E_i and E_r represent the incident and reflected electric fields, respectively, which are polarized in the y axis. 98
- B.1 Reflection geometry. The material occupies the lower half plane, $z > 0$, and the surface is in the xz plane. The saturation magnetisation is along x and the external field \mathbf{B}_0 is perpendicular to both the incidence plane and the easy axis (along y). The angle of incidence, θ_i , is the angle the wavevector of the incident wave makes with the normal to the surface. H_i and H_r represent the incident and reflected magnetic fields, respectively, which are polarized in the xz plane. E_i and E_r represent the incident and reflected electric fields, respectively, which are polarized in the y axis. 104

Introduction

1.1 Hyperbolic media	2
1.1.1 Indefinite permittivity and its properties	2
1.2 Phenomena	5
1.2.1 Goos-Hanchen shifts	5
1.2.2 Negative refraction	6
1.2.3 Slab lenses and focusing	8
1.3 Realisation of hyperbolic media	9
1.3.1 Hyperbolic metamaterials	9
1.3.2 Anisotropic single crystals	10
1.4 Objectives of the work	11
1.5 Structure of this Thesis	12

Photonic technologies are central to our society. For instance, optical fibres deliver telephone and internet traffic around the globe, while sub-millimetre wave based devices have been a key factor in recent imaging advances for medical and scientific applications [1]. The list of practical photonic devices is endless, however, the principle behind these technologies is one: to control, manipulate and shape the flow of electromagnetic waves. To achieve such functionalities, it is therefore necessary to use suitable media, which interacts with light in extraordinary ways.

One particular way to manipulate light in optical devices is to use refractive media as the basis for the apparatus. The index of refraction of a medium is a

property which determines the direction in which light is going to propagate within that material. The refractive index is known to always be positive [2]. However, recent advances in fabrication techniques have enabled the construction of new optical active materials with physical properties non-existent in nature with revolutionary optical capabilities, such as a negative index of refraction [3, 4]. To this new type of media was given the name “metamaterials” since their characteristics go beyond existent materials [5, 6]. This class of artificial media displays negative refractive index due to both magnetic permeability μ and dielectric permittivity ϵ being negative, a condition which is not possible to find in nature [7].

The concept of a medium with negative refractive index was first theorized by Soviet Physicist Victor Veselago in 1967. He predicted that if such a medium existed it would brake light in the reverse sense to that normally expected from classical geometric optics [8]. At first glance this theory was thought to be bizarre and preposterous [9]. However, the realization of metamaterials has enabled numerous new optical effects and it has opened up many new paths in the field of optical physics and device engineering [10, 11, 12, 13].

Fabricating structures that exhibit negative refraction, however, presents many difficulties in terms of structural growth. Aside from the manufacturing difficulties, to have both negative magnetic and electric response presents another significant challenge, it leads to high absorption at the operating frequencies, which can significantly impair these devices functionality.

As an alternative approach to metamaterials having simultaneous negative μ and ϵ , several different new media have been proposed [14]. Of particular note are the so-called hyperbolic media, which have rapidly gained attention for all-angle negative refraction with low losses [15]. In subsequent sections a detailed description is given on the role of hyperbolic media and its fascinating physical properties.

1.1 Hyperbolic media

Hyperbolic media have blossomed in the past decade as a route to obtain exotic new optical effects without complicated procedures in fabrication or large effects of absorption [16]. This class of media is characterized by being highly anisotropic and typically nonmagnetic with $\mu = 1$, but the permittivity tensor is indefinite, i.e., it has components with opposing signs along the principal axes. They are said to have hyperbolic dispersion due to the unusual relationship between the wavevector components resulting from indefinite permittivity [17][3].

1.1.1 Indefinite permittivity and its properties

The propagation of electromagnetic waves through a given medium may not show the same physical behaviour in all directions - in other words, the medium may be anisotropic. A classic example of anisotropic material is birefringent crystals, which are known for having different refractive indexes for the different polarisation of the incident light. The electrons bound within the atoms of a medium are not uniformly distributed, but are restricted in their motion by the potentials which confine them [14]. In response to incident electromagnetic fields, they may therefore move a greater or lesser distance, depending upon the strength of their confinement in the field direction. These can be classified as anisotropic forces and as a result, the induced polarisation varies not only with the strength of the incident electromagnetic fields, but also with its direction. The permittivity – and properties which depend upon it, such as the refractive index – cannot be characterized by a single scalar value and are usually characterized by a permittivity tensor [18].

In such media, the constitutive relations connecting the electric displacement \mathbf{D} , electric fields \mathbf{E} and the permittivity tensor $\overset{\leftrightarrow}{\epsilon}(\omega)$ can be written as

$$\mathbf{D} = \epsilon_0 \overset{\leftrightarrow}{\epsilon}(\omega) \mathbf{E} \quad (1.1)$$

where ϵ_0 is the vacuum permeability and $\overleftrightarrow{\epsilon}(\omega)$ is given by

$$\overleftrightarrow{\epsilon}(\omega) = \begin{pmatrix} \epsilon_{xx} & 0 & 0 \\ 0 & \epsilon_{yy} & 0 \\ 0 & 0 & \epsilon_{zz} \end{pmatrix}, \quad (1.2)$$

in a Cartesian frame of reference oriented along the so-called principal axes of the crystal. The three diagonal components are usually positive, and in general depend on the angular frequency ω ; the crystal is then classified as biaxial when $\epsilon_{xx} \neq \epsilon_{yy} \neq \epsilon_{zz}$, uniaxial when $\epsilon_{xx} = \epsilon_{yy} \neq \epsilon_{zz}$, and becomes isotropic when $\epsilon_{xx} = \epsilon_{yy} = \epsilon_{zz}$.

Now, consider radiation passing through an interface between vacuum and a uniaxial nonmagnetic medium whose uniaxis lies along z , normal to the interface. The in-plane wave-vector component k_x is then given by

$$k_x = \frac{\omega}{c} \sin \theta_i, \quad (1.3)$$

where θ_i is the angle of incidence. Boundary conditions dictate that this k_x value holds both sides of the interface.

Maxwell's equations may be applied in the two layers to find the z components of the wave vector. In vacuum, this gives

$$k_z^2 = \frac{\omega^2}{c^2} - k_x^2 \quad (1.4)$$

In the second layer, however, we need to consider that propagation of waves may happen in different ways for different polarisations. As we are considering a nonmagnetic medium transverse electric (TE) polarised waves are of no interest, since the magnetic field of light does not couple with elementary excitation in the material. Therefore, we concentrate on transverse magnetic (TM) polarised waves. We may characterize their propagation in a uniaxial crystal by the dispersion relation

$$\frac{k_x^2}{\epsilon_{zz}} + \frac{k_z^2}{\epsilon_{xx}} - \frac{\omega^2}{c^2} = 0. \quad (1.5)$$

When set to zero, the equations above correspond to a circle in k -space if the

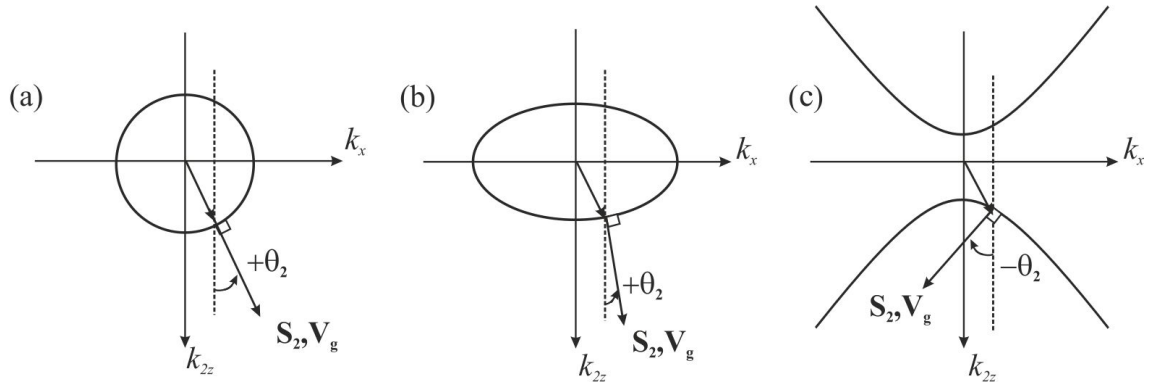


Figure 1.1: Isofrequency curve and relative direction of the wave vector \mathbf{k} and the Poynting vector \mathbf{S} for (a) isotropic material, (b) material with $\epsilon_{xx}\epsilon_{zz} > 0$, and (c) material with $\epsilon_{xx}\epsilon_{zz} < 0$.

medium is isotropic [Fig. 1.1(a)] and an ellipse if the medium is anisotropic with positive values for ϵ_{xx} and ϵ_{zz} [Fig. 1.1(b)]. However, that is not always the case. For instance, in a medium with active-phonon resonance polarised along one direction, i.e. extreme anisotropy, ϵ_{zz} may be negative for a given range of frequency (taking the phonon polarisation direction to be z). Media with such an optical signature are termed indefinite from the point of view of algebra [19], since their permittivity tensor represents an indefinite nondegenerate quadratic form, and exhibit a number of unconventional properties. One of these properties is hyperbolic isofrequency curves as seen in Fig. 1.1(c) – hence the physical denomination hyperbolic media - which only happens when the permittivity tensor components possess opposing signs.

1.2 Phenomena

Anomalous reflection and refraction phenomena have been revealed at the interface between air and hyperbolic media, such as negative refraction and focusing in flat slab as well as lateral displacements on a reflected light beam.

1.2.1 Goos-Hänchen shifts

The Goos-Hänchen effect is an optical phenomenon in which a light beam undergoes a lateral shift from the position predicted by geometrical optics, when totally reflected from an interface between two media. Even though the effect was

named after the scientists Hermann Fritz Gustav Goos and Hilda Hänchen [20], who demonstrated its existence experimentally, the first theoretical prediction of lateral displacements at reflection dates back to the 18th century with Isaac Newton.

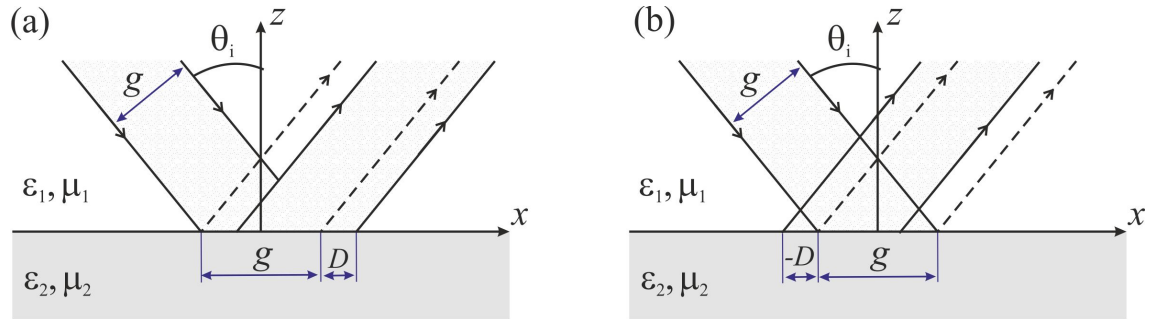


Figure 1.2: Schematic diagram of the Goos-Hänchen shift i.e., the lateral displacement, D , of a bounded beam at an interface. The dashed lines show the boundaries of the reflected beam as predicted by geometrical optics theory. (a) Positive and (b) negative displacements.

The concept of lateral displacement has had several interpretations over the years [21, 22]. However, the basic theory dictates that when a light beam of width g is totally reflected at an interface between two distinct media, a lateral displacement D of the beam arises in the plane of the interface where it is reflected. This displacement is generally classified within two categories: shifts of a positive order i.e., forward displacement as shown in Fig. 1.2(a), and shifts of a negative order i.e., backward displacement as seen in Fig. 1.2(b).

The first investigations of this effect have been associated with total internal reflection [20]. However, most recent studies have shown that lateral displacements can happen at external reflection of a beam incident from air onto a highly reflective surface.

The Goos-Hänchen effect is not necessarily associated with hyperbolic behaviour in the reflecting medium. It is understood that this type of displacement can happen in any highly reflective surfaces, such as metallic materials. However, making use of resonances in the second interface can be a simple, but little studied, way of obtaining Goos-Hänchen shifts on external reflection [23, 24, 25]. In this case, hyperbolic media may be particularly interesting, since resonant components of the permittivity tensor may lead to high reflection regions close to those resonance poles. Recent studies have shown that resonant features in the

dielectric function in hyperbolic multilayers can be a suitable way to obtain lateral shifts using the nonlocal optical response of the indefinite material [26]. It has also been shown that Goos–Hänchen shifts may arise from phonon resonances in uniaxial crystals such as quartz [27]. Similar effects have also been studied in the reflection from antiferromagnets [28]. In these systems, the effect stems from the fact that, at terahertz frequencies, the magnetic component of electromagnetic radiation can interact with the spin precession near magnon-polariton resonances. The resulting shift may become nonreciprocal in the presence of an suitably applied external field \mathbf{B}_0 . Up to now, studies of Goos–Hänchen shifts in reflection from antiferromagnets have considered only the situation where \mathbf{B}_0 is applied along the anisotropy axis, perpendicular to the plane of incidence [29, 30].

1.2.2 Negative refraction

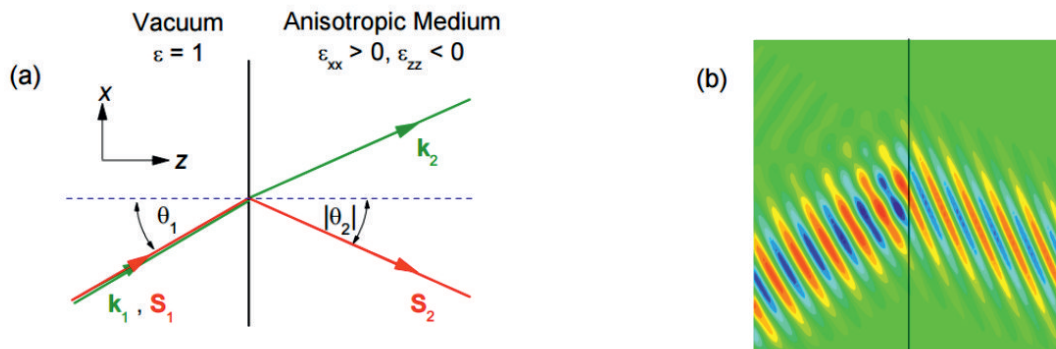


Figure 1.3: Directions of wavevectors and Poynting vectors for p-polarisation refraction at an interface between air and a uniaxial medium with $\epsilon_{xx} > 0$, $\epsilon_{zz} < 0$. (b) Corresponding instantaneous field profile for a gaussian beam.

Negative refraction of transverse magnetic (TM) polarised waves was probably the first phenomenon associated to hyperbolic metamaterials to be studied [16]. Negative refraction in hyperbolic media can be explained by considering the interface between a nonmagnetic hyperbolic medium and vacuum. We assume that the component of the dielectric tensor perpendicular to the interface plane is negative and that the other two components are positive, and consider a TM-polarised plane wave incident on the interface with an in-plane wave vector k_x . We further assume that the electric field and the wave vector lie in the xz plane, and that the interface lies in the xz plane (Fig. 1.3(a)). In this geometry the angle

of refraction, interpreted in terms of the direction of the time averaged power flow $\langle \mathbf{S} \rangle$ in the anisotropic medium, is given by [31]

$$\tan \theta_r = \frac{S_{x2}}{S_{z2}} = \frac{\text{Re}(k_x/\epsilon_{zz})}{\text{Re}(k_{z2}/\epsilon_{xx})} \quad (1.6)$$

where ϵ_{xx} and ϵ_{zz} are the principal components of the dielectric function in the anisotropic media.

In the situation for which $\epsilon_{xx} > 0$ and $\epsilon_{zz} < 0$ there should be propagation into the sample. In addition, we see from Eq. 1.6 that θ_r is negative for θ_i positive, i.e. negative refraction should occur, as shown in Fig 1.3(a). Thus, although the wavevector is refracted positively, power flow is refracted negatively. The physical interpretation of this in terms of a finite gaussian beam is shown in Fig. 1.3(b). The wavevector direction is normal to the wavefronts, but the ray direction is determined by the power flow direction.

An alternative way of interpreting negative refraction in this type of system is shown in Fig. 1.1(c). Since the direction of the Poynting vector is identical to the direction of the group velocity vector $\mathbf{v}_g = \nabla_{\mathbf{k}}\omega(\mathbf{k})$. This means that \mathbf{S} should be normal to an equifrequency surface in \mathbf{k} space. Negative refraction of the Poynting vector direction is clearly seen, and it is obvious that such behavior will occur for a both positive and negative incident angles (positive and negative k_x).

1.2.3 Slab lenses and focusing

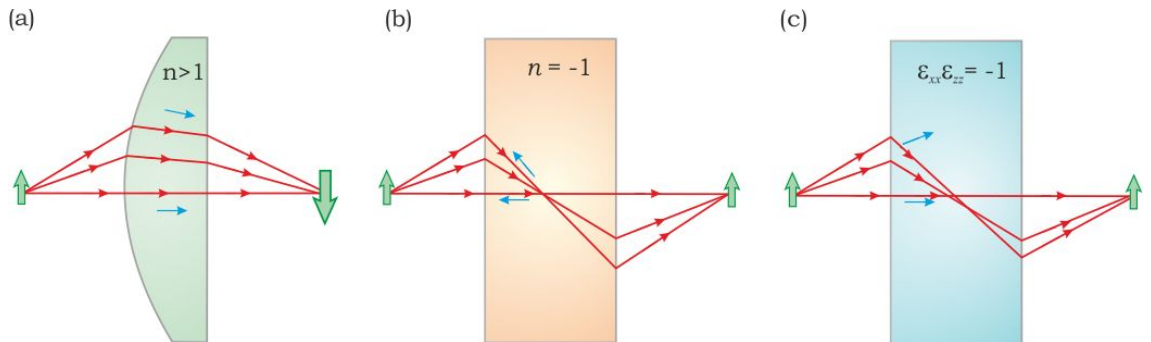


Figure 1.4: (a) Image formation by a conventional convex lens, (b) image formation from a negative-index flat lens and (c) image formation from a slab lens made of a hyperbolic medium. Directions of wavevector is show in blue arrows and the Poynting vector is shown in red arrows.

Particular attention has been paid to all-angle negative refraction as it has enabled

focusing of radiation and perfect imaging in a flat slab made of metamaterials. Focusing of light, however, has been investigated for centuries, specially in curved glass lenses such as the one shown in Fig 1.4(a). In this system the rays are guided onto a focus by the curvature of the lens which creates a real but imperfect inverted image since not all beams meet at the same point.

In metamaterials with $\mu = \varepsilon = -1$, which gives $n = -1$ (where n is the index of refraction), all beams are focused at the same point in the center of the lens and outside of it. Another important feature of this type of lens is that evanescent waves, which usually decay exponentially inside a medium which has $n > 0$, are enhanced inside a metamaterial. These evanescent waves carry the details of an object, which means the image formed is perfect with minute details and unlimited sharpness.

Negative refraction in hyperbolic media raises the possibility of realizing a lens analogues to a superlens made from negative-index metamaterials [32]. A crucial difference is that the group velocity and power flow are always antiparallel in negative index metamaterials, whereas in hyperbolic media the group velocity and power flow directions depend on the propagation direction relative to the principal axis. The ray-tracing diagram in Fig. 1.4(c) shows that at small angles of incidence, a lens made of hyperbolic media focuses rays in a similar manner to a negative-index slab, whereas rays with larger angles of incidence remain defocused.

Another important point to make is that in hyperbolic media, the evanescent waves are not amplified. However a real image is formed on the other side of the slab, in the same way as the lenses proposed by Veselago.

1.3 Realisation of hyperbolic media

Clearly, the special nature of indefinite permittivity systems leads to a number of exotic effects. Here arises a natural question: how can we obtain such a response from physical materials? There are several ways to obtain indefinite permittivity in physical media. However, they all fit into two general categories: artificial media and natural anisotropic crystals.

1.3.1 Hyperbolic metamaterials

A common method of obtaining indefinite permittivity is to combine two types of media. One of the most simple ways is to produce a system of alternating metal and dielectric layers [33, 34, 35, 36, 15, 37]. In this case, each layer can be described by homogeneous and isotropic permittivity and permeability parameters and when the layers are sufficiently thin, the whole system can be treated as a single anisotropic medium with dielectric permittivity tensor components given by

$$\varepsilon_{xx} = \varepsilon_{yy} = \frac{\varepsilon_1 + \eta\varepsilon_2}{1 + \eta} \quad (1.7)$$

and

$$\frac{1}{\varepsilon_{zz}} = \frac{1}{1 + \eta} \left(\frac{1}{\varepsilon_1} + \frac{\eta}{\varepsilon_2} \right), \quad (1.8)$$

where ε_1 and ε_2 are corresponding permittivities for each medium and η is the ratio of the two layer widths given by $\eta = d_2/d_1$.

When η is small, the parameters are dominated by the first medium, while for large η , they resemble those of the second medium. By choosing a suitable value of η the condition $\varepsilon_{xx} > 0$ and $\varepsilon_{zz} < 0$ can be satisfied.

Other examples of artificial structures include aligned parallel nanowire structures [38]. These are also metal based since in metals, the dielectric function is negative below the plasma frequency.

1.3.2 Anisotropic single crystals

Even though hyperbolic media have been classified as a class of metamaterials [16], indefinite permittivity has attracted interest since much earlier [39]. However, the study of natural crystals as hyperbolic media is fairly recent [40]. Examples of such materials can easily be found in the infrared and THz spectral bands. For instance, in the far infrared wavelengths, this behaviour can be found in crystal quartz. In quartz a strong phonon-polariton resonance leads to a large anisotropy in the dielectric tensor comparable to that of the artificially grown superlattices. This has been shown at room temperature and the condition $\varepsilon_{xx} > 0$ and $\varepsilon_{zz} < 0$

is satisfied in the region between 510 and 540 cm^{-1} [41, 42].

Similar behaviour has been suggested in triglycine sulphate (TGS) at 5K [31]. In this medium, however, due to low temperature the imaginary part of ϵ becomes significantly small, which extremely minimizes absorption. Whereas the phonon anisotropy of TGS exists in the low-THz domain, for other materials, it may occur in a different spectral band. Recent experiments using sapphire ($\alpha\text{-Al}_2\text{O}_3$) have yielded results pointing to all-angle negative refraction based on this property [43] at several different frequency ranges from 400 to 910 cm^{-1} . Other materials considered include Hg_2I_2 [44] and magnesium fluoride (MgF_2) [45]. The main effect in sapphire occurs around the same frequency as that of quartz, but it has a somewhat larger absorption. Hg_2I_2 , whose phonon resonance frequencies are considerably lower, also has a larger absorption than quartz, but, in compensation, the phonon response is considerably more direction dependent. It is important to point out here that all these materials have been reported at room temperature.

1.4 Objectives of the work

Hyperbolic dispersion relations due to indefinite permittivity has been demonstrated in several natural nonmagnetic crystals. Phenomena based on hyperbolic dispersion in media with indefinite permeability, i.e., principal components of the permeability tensor have opposing signs, have received rather less attention. However, we should expect the magnon-polariton response in certain natural magnetic media to lead to opposing sign components in the permeability tensor, in a manner analogous to phonon-polariton response leads to indefinite permittivity in anisotropic crystals.

The main objective of this thesis is to demonstrate the possibility of novel optical effects in natural magnetic hyperbolic crystals which can be tunable when using externally applied magnetic fields. We are interested in three main topics: (1) lateral shifts on the reflection, (2) tunable negative refraction and (3) focusing by a natural hyperbolic magnetic crystal.

1.5 Structure of this Thesis

We start by discussing some basic concepts in Chapter 2 which are essential to the understanding of waves propagating through magnetic crystals. We also present the theoretical demonstration of how antiferromagnets act as indefinite permeability media, i.e., not all its permeability tensor components are of the same sign. In addition, we show the effects of an externally applied magnetic field \mathbf{B}_0 on the permeability tensor and its physical implications.

In Chapter 3, we show how light beams reflected from the surface of an antiferromagnet can be laterally shifted from the position predicted by geometrical optics. In antiferromagnets this shifts can be controlled with an external magnetic field. Moreover, we show that nonreciprocal displacements are possible due to inherent nonreciprocity of the polariton phase with respect to the propagation direction. In the absence of an external field, reciprocal displacements occur.

We show how all-angle negative refraction can occur in a uniaxial antiferromagnet close to the magnon-polariton resonance frequency in Chapter 4. If an external magnetic field is applied, the angle of refraction becomes tunable, and can be made to change sign. Optical effects such as negative refraction have been vastly studied in terms of imaging obtained from slab lenses with plane parallel sides. In chapter 5, we discuss how antiferromagnetic crystals not only display similar effects but also allow one to modify the focal length of a slab lens with an externally applied magnetic field. In addition, a rich caustic structure emerges at low temperatures, when damping should be small. These materials also produce slab focusing at higher temperatures, although the caustic structure disappears. A look into future ideas is given in 6, where we present a first glimpse on how the focusing in slab lenses with parallel sides made of a hyperbolic magnetic media can be highly affected by changes in the crystal's easy axis direction. The final remarks are presented in Chapter 7.

Magnetic Polaritons and Indefinite Permeability

2.1 Antiferromagnetic Crystals	14
2.2 Antiferromagnetic resonance	15
2.2.1 The indefinite permeability tensor	18
2.3 Field Driven Spin Canting	20
2.3.1 External Field and the Permeability Tensor	23
2.4 Magnetic polaritons	24
2.4.1 Dispersion Relation	25
2.5 Damping Effects	31
2.5.1 Damping temperature dependence	32

When an electromagnetic wave propagates through a condensed medium, its properties are modified by the coupling of the electric and magnetic fields of the wave to the elementary excitations of the medium [46]. The coupled excitation is frequently referred to as a polariton and consists of a photon coupled to a plasmon, optical phonon, magnon, or an exciton which polarises the crystal. Polaritons are understood to be either surface polaritons (the electromagnetic field is localized at the surface of the medium) or bulk polaritons (the electromagnetic field propagates through the medium) [47].

The behaviour of these bulk (and also surface) electromagnetic modes of physical media – including dielectric crystals, ferrites, antiferromagnets and artificial dielectric – may be described in terms of dyadic permittivity $\overleftrightarrow{\epsilon}(\omega)$ and (or) permeability $\overleftrightarrow{\mu}(\omega)$ [48]. For instance, in non-magnetic crystals the electric field

of light will couple with infrared active phonons, which can be described by the frequency dependence of the relevant dielectric function $\overset{\leftrightarrow}{\epsilon}(\omega)$. On the other hand, in magnetic crystals spin waves will be excited by the magnetic field of light and that can be expressed using the frequency dependent magnetic permeability $\overset{\leftrightarrow}{\mu}(\omega)$ [46].

Recently, problems of radiation from stationary sources travelling through media displaying anisotropy have gained in importance due to the materials' capability of shape or guide the waves in unexpected ways. Special attention has been paid to indefinite media, i.e. anisotropic media in which not all of the principal components of the $\overset{\leftrightarrow}{\epsilon}(\omega)$ tensors have the same sign [3, 17] as addressed in Chapter 1.

Up to now, studies of indefinite media have mostly concentrated on nonmagnetic crystals where it is assumed that there is no contribution of the magnetic permeability μ . However, in magnetic crystals, $\overset{\leftrightarrow}{\mu}(\omega)$ will in general be a tensor quantity, which, may be indefinite close to magnetic resonance frequency [49].

It is the purpose of this Chapter to investigate indefinite permeability (i.e. a permeability tensor containing components of opposing signs), which can be achieved in a similar manner to the indefinite permittivity found in certain anisotropic crystals. We use the example case of antiferromagnetic crystals whose resonance, associated with magnetic excitations and known as magnons, may lead to negative permeability components. It is also in the scope of this Chapter to present the consequences of waves propagating in an antiferromagnetic crystal possessing indefinite permeability.

2.1 Antiferromagnetic Crystals

The term "antiferromagnetic" is used to describe materials in which an antiparallel arrangement of the magnetic moments of atoms or molecules, usually related to the spins of electrons, is favoured [50]. Such behaviour was first suggested by Néel,¹ who originally investigated a simple material whose spins are aligned in

¹Louis Néel (1904-200) was a French physicist who was awarded a Nobel Prize in 1970 for his pioneering studies of the magnetic properties of solids. In 1930 he demonstrated a new form of magnetic behaviour, called antiferromagnetism, as opposed to ferromagnetism.

a regular pattern with neighbouring spins pointing in opposite directions. The spins have equal magnetic moments so that the net magnetisation is zero such as the schematic shown in Fig 2.1(b). Such spin ordering is temperature dependent, vanishing at and above a certain temperature, which has been named the Néel temperature T_N [51].

The antiferromagnetic class of materials include systems with two or more sublattices as well as those with triangular, spiral or canted spin arrangements. We consider here the two-sublattice uniaxial antiferromagnet MnF_2 . The magnetic structure of MnF_2 , which has been determined by several experimental methods, including neutron diffraction studies [52], is shown in Fig. 2.1(a). This crystal belongs to an important group of antiferromagnetic salts (MnF_2 , FeF_2 and CoF_2), which have been widely studied [46]. In this type-system the unit cell has tetragonal symmetry formed by the magnetic ion sites and they may be conveniently pictured as a body-centered cube compressed along the c axis. The spins at the corner sites point along $+x$, and those at the body centred sites point along $-x$ [46, 53]. The magnetic unit cell has the same dimensions as the chemical unit cell.

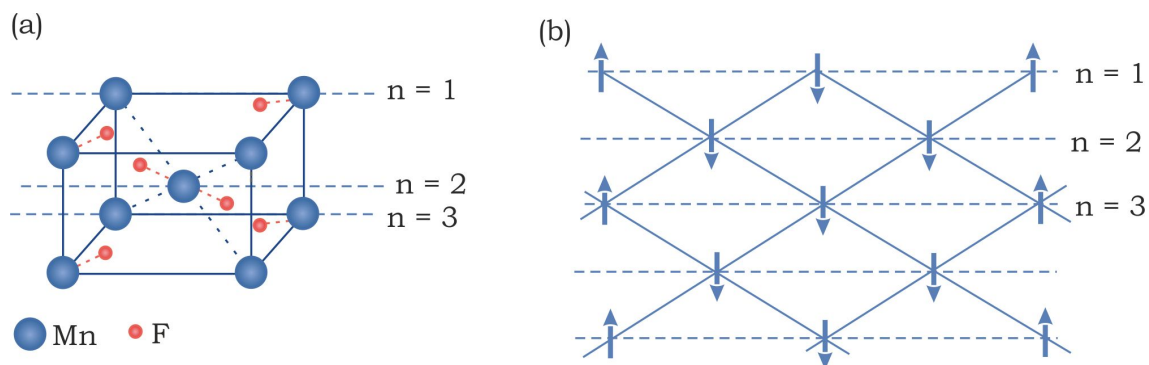


Figure 2.1: Chemical arrangement of a simple antiferromagnet such as in manganese fluoride (MnF_2) crystals with body-centred tetragonal structure: (a) perspective view and (b) side view.

Such systems, as shown in Fig. 2.1(b), are usually known as “pure uniaxial antiferromagnets”. In a crystal arrangement the magnetic ions are arranged on two identical interpenetrating sublattices [54]. If there is no contribution from an external magnetic field, the spins on each sublattice order ferromagnetically, i.e. all spins on a given sublattice are parallel, but not aligned with other sublattices [46, 53].

The spins in a simple antiferromagnets are aligned by exchange interactions

so that they spontaneously order. As a result, the magnetic moment (M_S) is zero.[55, 56].

2.2 Antiferromagnetic resonance

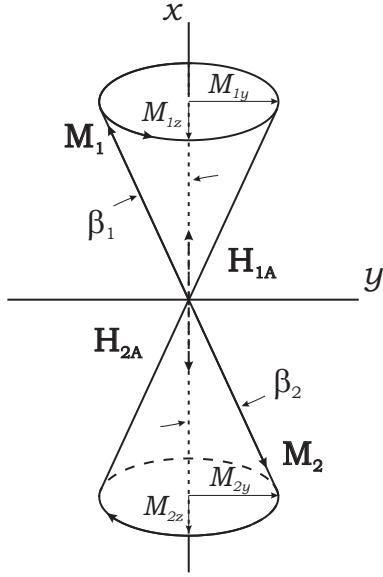
When an electromagnetic wave strikes the surface of an antiferromagnet, the magnetic field of the radiation (\mathbf{H}) interacts with the spins in the material, inducing precessional motion [57]. The spin magnetic moments $\boldsymbol{\mu}$ associated with the spins it is subjected to a torque \mathbf{L} when placed in a uniform field such as \mathbf{H} , and is given by

$$\mathbf{L} = -\frac{\partial W}{\partial \theta} = \boldsymbol{\mu} \mathbf{H} \sin \beta, \quad (2.1)$$

where β is the angle between $\boldsymbol{\mu}$ and \mathbf{H} , and energy $W = -\boldsymbol{\mu} \cdot \mathbf{H}$. In vectors, remembering that the cross product anticommutes, this can be rewritten as

$$\mathbf{L} = \boldsymbol{\mu} \times \mathbf{H} \quad (2.2)$$

The dynamic response to a time varying magnetic field in antiferromagnets is depicted in in Fig. 2.4 which shows spins precessing in opposite directions. At low temperatures the dissipation of precession, and consequent resonance linewidths, decreases strongly by suppressing scattering from lattice fluctuations. We consider a temperature low enough so that the magnetisation in each sublattice is saturated, which we call \mathbf{M}_s . The magnetic field of light induces antiparallel magnetic moments and these may the be computed by means of the torque equation so that Eq. (2.1) now becomes Eqs. (2.3) and (2.4) for each of the sublattices.



$$\frac{d\mathbf{M}_1}{dt} = \gamma(\mu_0\mathbf{M}_1 \times \mathbf{H}_{\text{eff}}^{(1)}) \quad (2.3)$$

$$\frac{d\mathbf{M}_2}{dt} = -\gamma(\mu_0\mathbf{M}_2 \times \mathbf{H}_{\text{eff}}^{(2)}) \quad (2.4)$$

Figure 2.2: Equilibrium spin orientation for uniaxial antiferromagnet, with antiparallel precession in the absence of an externally applied field.

where γ is the gyromagnetic ratio, $\mathbf{M}_s = |\mathbf{M}_1| = |\mathbf{M}_2| = (\Sigma\mu)$ are the magnetisation associated with each sublattice and \mathbf{H}_{eff} is the effective fields acting on the sublattice given by

$$\mathbf{H}_{\text{eff}}^{(i)} = \mathbf{H}_{iA} + \mathbf{H}_{iE} + \mathbf{H} \quad (2.5)$$

where \mathbf{H}_{iA} measures the anisotropy force, \mathbf{H}_{iE} is the exchange force exerted on each ion by the ions forming the other sublattice and i is the given sublattice. There are the internal effective fields constraining the sublattice magnetisations to the preferred axis ($+x$ and $-x$). As the precession is identical, but in opposing directions $\mathbf{H}_{1A} = |\mathbf{H}_{2A}| = |\mathbf{H}_A|$, $\mathbf{H}_{1E} = |\mathbf{H}_{2E}| = |\mathbf{H}_E|$ and $\beta_1 = \beta_2$.

We then assume the transverse components of the magnetisation to vary time as \mathbf{H} given by

$$\mathbf{H} = \hat{z}h_z e^{i\omega t} \quad (2.6)$$

polarised along z , so its disturbance in the spin system is in the yz plane. We can, therefore, linearize the torque equations of motion by replacing \mathbf{M}_1 and \mathbf{M}_2 by $\pm\mathbf{M}_s$, $\mathbf{H}_E = \mathbf{B}_E/\mu_0$ and $\mathbf{H}_A = \mathbf{B}_A/\mu_0$. The torque Equations (2.3) and (2.4) then

become

$$-\frac{i\omega}{\gamma}M_{1y} = M_{1z}B_A + (M_{1z} + M_{2z})B_E - \mu_0 M_S h_z \quad (2.7a)$$

$$-\frac{i\omega}{\gamma}M_{1z} = -M_{1y}B_A - (M_{1y} + M_{2y})B_E \quad (2.7b)$$

$$-\frac{i\omega}{\gamma}M_{2y} = -M_{2z}B_A - (M_{1z} + M_{2z})B_E + \mu_0 M_S h_z \quad (2.7c)$$

$$-\frac{i\omega}{\gamma}M_{2z} = M_{2y}B_A + (M_{1y} + M_{2y})B_E. \quad (2.7d)$$

Substitution of the circular polarised magnetisation

$$M_y = M_{1y} + M_{2y} \quad (2.8a)$$

$$M_z = M_{1z} + M_{2z} \quad (2.8b)$$

into Eq. (2.7) yields

$$\omega_0 = \pm\gamma(2B_A B_E + B_A^2)^{1/2}. \quad (2.9)$$

This is the frequency at which the amplitude of precession peaks and it depends on the interactions responsible for the antiferromagnetic order and the magnetic anisotropy of the crystal [58, 59]. The sign \pm can be chosen according to the precession modes, there are thus two possible solutions, opposite in the sense of precession as seen in Fig. 2.4. This resonance determines frequency poles in the magnetic susceptibility $\overset{\leftrightarrow}{\chi}(\omega)$, which is expressed as

$$M_z = \overset{\leftrightarrow}{\chi}(\omega)h_z \quad (2.10)$$

It is convenient to employ the permeability rather than the susceptibility for

further calculations. Since $\overset{\leftrightarrow}{\mu}(\omega) = 1 + \overset{\leftrightarrow}{\chi}(\omega)$ we can turn Eq.(2.8) into

$$\mu_{yy} = \mu_{zz} = 1 + \frac{M_z}{h_z} = 1 + \frac{2\mu_0\gamma^2 M_S B_A}{\omega_0^2 - \omega^2}. \quad (2.11)$$

As the sublattices are perfectly aligned anti-parallel to one another and denoting these orientations as $+x$ and $-x$, the precession - and corresponding dynamic response - is in the transverse z and y directions. This means that μ_{xx} is unity at all frequencies.

2.2.1 The indefinite permeability tensor

We have seen how to obtain the permeability components from $\overset{\leftrightarrow}{\mu}(\omega) = 1 + \overset{\leftrightarrow}{\chi}(\omega)$. If we now define $\mathbf{1}$ the unity tensor, when there is no externally applied field \mathbf{B}_0 , we can write all components as a permeability tensor of the form

$$\overset{\leftrightarrow}{\mu}(\omega) = \begin{pmatrix} \mu_{xx} & 0 & 0 \\ 0 & \mu_{yy} & 0 \\ 0 & 0 & \mu_{zz} \end{pmatrix}, \quad (2.12)$$

where $\mu_{xx} = 1$ and $\mu_{yy} = \mu_{zz}$, which are both given by Eq. (2.11). We now turn to the example material MnF_2 which is a well characterized antiferromagnet that can be readily prepared and studied experimentally. Using the parameters given in table 2.1 we can calculate the values of μ_{zz} , which is shown in Fig. 2.3.

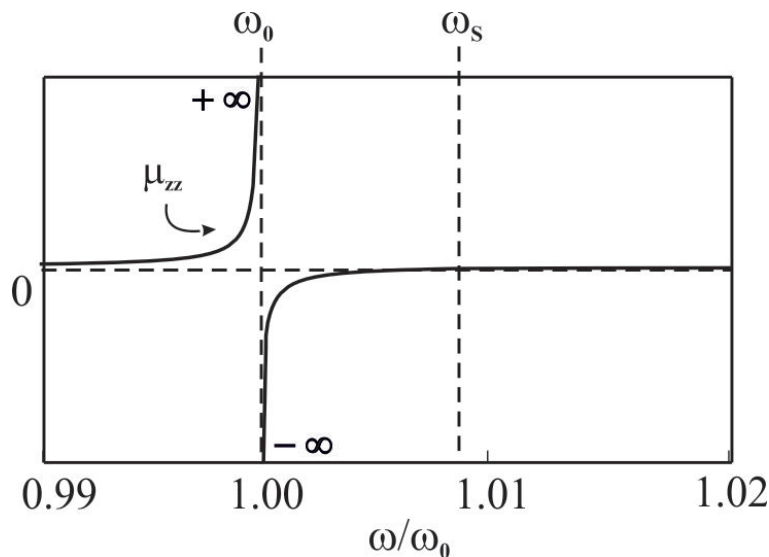


Figure 2.3: μ_{zz} for an MnF_2 crystal calculated using the values given in table 2.1.

A strong magnon-polariton resonance occurs at $\omega/\omega_0 = 1.00$ and appears in the transverse components being negative from $\omega/\omega_0 = 1.00$ (ω_0) to approximately 1.007 (ω_s).

If we restrict our analysis to the frequency regime $\omega_0 \leq \omega \leq \omega_s$ we can sum up the signs of the tensor components, shown in Eq. (2.12), as follows

$$\overset{\leftrightarrow}{\mu}(\omega) = \begin{pmatrix} + & 0 & 0 \\ 0 & - & 0 \\ 0 & 0 & - \end{pmatrix}, \quad (2.13)$$

In this frequency regime, the antiferromagnetic crystal can be classified as *never cutoff* [19]. *Never cutoff* media have been classified, by Smith and Schurig, as possessing $\mu_{xx}/\mu_{zz} < 0$.

This behaviour can be taken as the magnetic analogue of a highly anisotropic non-magnetic media where the effective permittivity tensor $\overset{\leftrightarrow}{\epsilon}(\omega)$, has components of different signs, e.g., $\epsilon_{ord} > 0$ and $\epsilon_{ext} < 0$ close to the polariton resonance.

Table 2.1: Physical parameters for antiferromagnets

Antiferromagnetic crystal parameters			
	MnF ₂	GdAlO ₃	FeF ₂
Néel Temperature T_N (K)	67	3.87	79
Exchange field B_E (T)	55	1.88	53.3
Anisotropy Field B_A (T)	0.787	0.365	19.7
Sublattice Magnetisation M_S (A/m)	6.0×10^5	6.24×10^5	5.6×10^5

2.3 Field Driven Spin Canting

In the simple case discussed in Section 2.2, the antiferromagnetic resonance of the two spin wave modes are degenerate with frequency ω_0 , i.e. the resonance in the two sublattices are exactly the same but in opposing directions, making this a symmetric system. If an external magnetic field is present, it brakes the time reversal symmetry [60]. The influence of a magnetic field has been investigated in many aspects, a particular one, is when a static field \mathbf{B}_0 lies along the easy axis

direction. In this case, the sublattices are no longer equivalent so that there are two resonance frequencies instead of one. Such geometry has been vastly studied in terms of nonreciprocal effects associated with reflection and surface waves, since propagation is forbidden around the resonance frequency.

Here, we are interested in a geometry as such that a static field \mathbf{B}_0 is applied perpendicular to the spins alignment direction and along y . In order to analyse such behaviour we need to derive the form of the dynamic permeability for the two-sublattice antiferromagnet in similar manner as that employed in Section 2.2. We proceed by examining the classical equations of motion for the magnetisation of each sublattice given by Eqs. (2.3) and (2.4). However, $\mathbf{H}_{\text{eff}}^{(i)}$ has to be modified in order to accommodate \mathbf{B}_0 and it is now given by

$$\mathbf{H}_{\text{eff}}^{(i)} = \frac{1}{\mu_0}(\mathbf{B}_0 + \mathbf{B}_{iA} + \mathbf{B}_{iE}) + \mathbf{H} \quad (2.14)$$

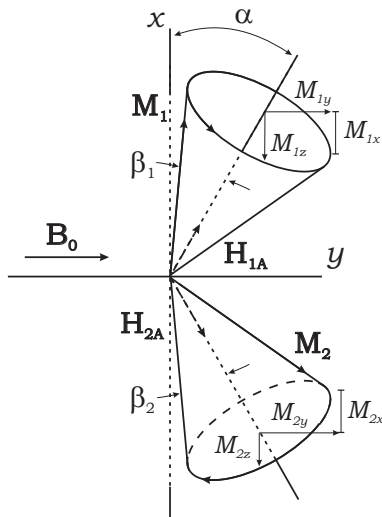
As depicted in Fig. 2.4, we also need to consider that the magnetisations \mathbf{M}_1 and \mathbf{M}_2 are given in terms of the angle α , which can be calculated by

$$B_0(1 - \sin \alpha) - B_E \sin(2\alpha) - \frac{1}{2}B_A \sin(2\alpha) = 0 \quad (2.15a)$$

or

$$B_0(1 + \sin \alpha) - B_E \sin(2\alpha) + \frac{1}{2}B_A \sin(2\alpha) = 0 \quad (2.15b)$$

which yields



$$\sin \alpha = \frac{B_0}{B_A + 2B_E} \quad (2.16)$$

Figure 2.4: Disturbed spin orientation for uniaxial antiferromagnet by an externally applied field \mathbf{B}_0 inducing spin canting of the antiparallel precession magnetisations.

The angle α is a direct representation of the canting of the sublattice magnetisations in order to align to the magnetic field direction. The direct effect of spin canting is precessional components along all coordinate axes and the net magnetisation is no longer zero. Given the angle α , the derivation of the normalized sublattice magnetisation differ from those show in Eq. 2.8 and are now given by

$$-\frac{i\omega}{\gamma}M_{1x} = \cos \alpha [B_E(M_{2y} - M_{1y}) + B_A M_{1y} - \gamma h_{1y}], \quad (2.17a)$$

$$-\frac{i\omega}{\gamma}M_{1y} = B_0 M_{1y} + \cos \alpha [B_E(M_{1y} - M_{2y}) + \gamma h_{1y}], \quad (2.17b)$$

$$\begin{aligned} -\frac{i\omega}{\gamma}M_{1z} = & -B_0 M_{1x} + \cos \alpha [B_E(M_{2x} - M_{1x} + M_{1z} - M_{2z}) \\ & + B_A(M_{1z} - M_{1x}) + (h_{1z} - h_{1x})] \end{aligned} \quad (2.17c)$$

and

$$-\frac{i\omega}{\gamma}M_{1x} = \cos \alpha [B_E(M_{1y} - M_{2y}) + B_A M_{2y} - \gamma h_{1y}], \quad (2.17d)$$

$$-\frac{i\omega}{\gamma}M_{2y} = B_0 M_{2y} + \cos \alpha [B_E(M_{2y} - M_{1y}) + \gamma h_{1y}], \quad (2.17e)$$

$$\begin{aligned} -\frac{i\omega}{\gamma}M_{2z} = & -B_0 M_{2x} + \cos \alpha [B_E(-M_{2x} - M_{1x} - M_{1z} + M_{2z}) \\ & + B_A(M_{2z} - M_{2x}) + (h_{1x} - h_{1z})] \end{aligned} \quad (2.17f)$$

The combinations of these formulas yields a quadratic equation for ω^2 , and thus we have two distinct resonance frequencies. This means that not all components of the susceptibility, and hence permeability, are resonance at the same frequency. These resonance frequencies are given in terms of ω_0 and the angle α , assuming

the form

$$\omega_{\parallel}^2 = \omega_0^2 \cos^2 \alpha \quad (2.18)$$

and

$$\omega_{\perp}^2 = \omega_0^2 \cos^2 \alpha + 2B_E B_0 \sin \alpha, \quad (2.19)$$

which also depends on the strength of the applied field \mathbf{B}_0 .

Therefore, it is a matter of algebra to construct the new permeability components using Eq. (2.10). Then we find

$$\mu_{xx} = 1 + \frac{2\mu_0\gamma^2 M_S B_0 \sin \alpha}{\omega_{\perp}^2 - \omega^2}, \quad (2.20)$$

$$\mu_{yy} = 1 + \frac{2\mu_0\gamma^2 M_S B_E \cos^2 \alpha}{\omega_{\parallel}^2 - \omega^2}, \quad (2.21)$$

$$\mu_{zz} = 1 + \frac{2\mu_0\gamma^2 M_S (B_0 \sin \alpha + B_A \cos 2\alpha)}{\omega_{\perp}^2 - \omega^2}, \quad (2.22)$$

while

$$\mu_{xz} = -\mu_{zx} = -i \frac{2\mu_0\gamma^2 M_S \omega \sin \alpha}{\omega_{\perp}^2 - \omega^2}. \quad (2.23)$$

2.3.1 External Field and the Permeability Tensor

Distinct from non-magnetic crystals, the indefinite behaviour in magnetic media can be controlled with a magnetic field, which affects the magnon-polariton resonance frequency. If a magnetic field \mathbf{B}_0 is applied perpendicular to the zero field sublattice directions (here taken as y), the sublattice magnetisations will cant in order to align to the magnetic field direction as discussed in Section 2.2.

As the spin canting induces precessional motion along all directions the permeability tensor $\overleftrightarrow{\mu}(\omega)$ has to be modified as to include the off-diagonal elements

μ_{xz} and μ_{zx} . It now takes the form

$$\overset{\leftrightarrow}{\mu}(\omega) = \begin{pmatrix} \mu_{xx} & 0 & \mu_{xz} \\ 0 & \mu_{yy} & 0 \\ -\mu_{xz} & 0 & \mu_{zz} \end{pmatrix}, \quad (2.24)$$

The main effect of \mathbf{B}_0 is to shift the resonance ω_0 to higher frequencies. Therefore the resonance and its features, such as $\mu_{xx} > 0$ and $\mu_{zz} < 0$, are also tuned to different frequencies [49]. Fig. 2.5(a) shows the effect of a magnetic field on μ_{zz} . The values of $Re(\mu_{zz})$, $Re(\mu_{xx})$ and $Im(\mu_{xz})$ are compared in Fig 2.5, with and without an applied field. The resonance frequency is now shifted to higher frequencies depending on the magnitude of the external field.

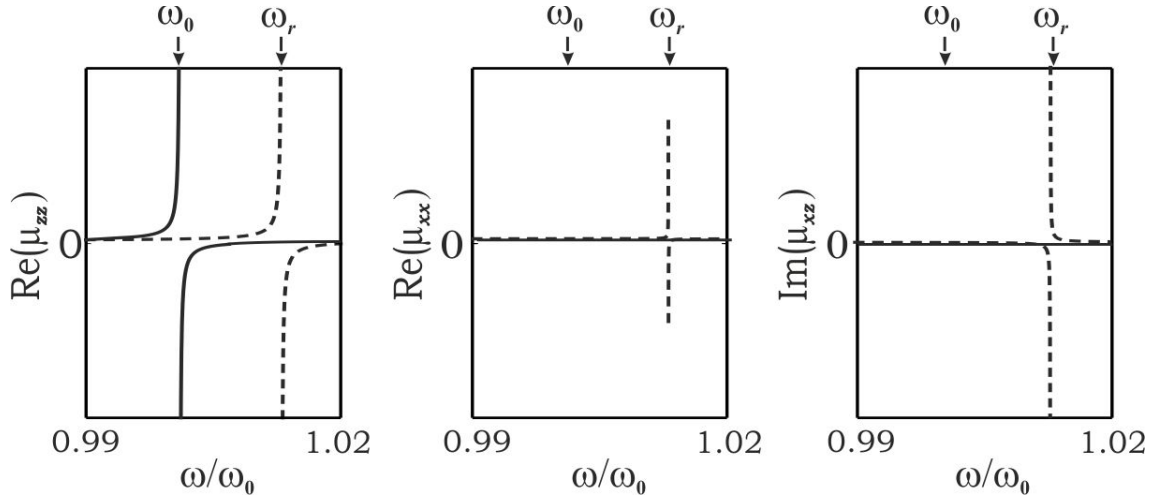


Figure 2.5: (a) $Re(\mu_{zz})$, (b) $Re(\mu_{xx})$ and (c) $Im(\mu_{xz})$. Solid curve: ($\mathbf{B}_0 = 0$); dashed curve ($\mathbf{B}_0 = 1.5$ T.)

For a nonzero \mathbf{B}_0 , all plots show resonances at ω_{\perp} , but the resonances in μ_{xx} and μ_{xz} are much weaker than that in μ_{zz} since the canting angle is small ($\mathbf{B}_0 = 1$ T corresponds to a canting angle of $\alpha = 0.54^{\circ}$). Note that we show $Im(\mu_{xz})$ rather than $Re(\mu_{xz})$ because in this geometry the real part consists of a weak peak at ω_{\perp} and it is the imaginary component that shows up the characteristic resonant.

2.4 Magnetic polaritons

The dynamic response of antiferromagnets to optical waves is determined by competition between components of the permeability tensor. Having now discussed the nature of resonances and general structure of the tensor, we now turn

to the electromagnetic problem.

2.4.1 Dispersion Relation

Properties of propagating electromagnetic waves in a medium begin with Maxwell's equations. In the material, Maxwell's equations without sources or currents hold. Thus:

$$\nabla \cdot \vec{D} = 0, \quad (2.25a)$$

$$\nabla \times \vec{E} = -\frac{\partial \vec{B}}{\partial t}, \quad (2.25b)$$

$$\nabla \cdot \vec{B} = 0, \quad (2.25c)$$

$$\nabla \times \vec{H} = \frac{\partial \vec{D}}{\partial t} \quad (2.25d)$$

Considering that the medium responds to the incident field in a linear manner, we have the constructive relations

$$\vec{D} = \epsilon_0 \overset{\leftrightarrow}{\epsilon}(\omega) \vec{E}, \quad (2.26)$$

and

$$\vec{B} = \mu_0 \overset{\leftrightarrow}{\mu}(\omega) \vec{H}, \quad (2.27)$$

where the permeability and permittivity inside the medium are given by $\overset{\leftrightarrow}{\epsilon}(\omega)$ and $\overset{\leftrightarrow}{\mu}(\omega)$.

One of the exciting aspects of indefinite permeability media is the propagation of waves around the magnon-polariton resonance. In order to illustrate this, we start by considering electromagnetic waves propagating from vacuum onto a uniaxial antiferromagnet in the geometry shown in Fig. 2.6. The antiferromagnetic crystal lies in the half-space $z \geq 0$, and its principal axes lie along the Cartesian axes x , y , and z . xz is the plane of incidence and z is normal to the slab surface.

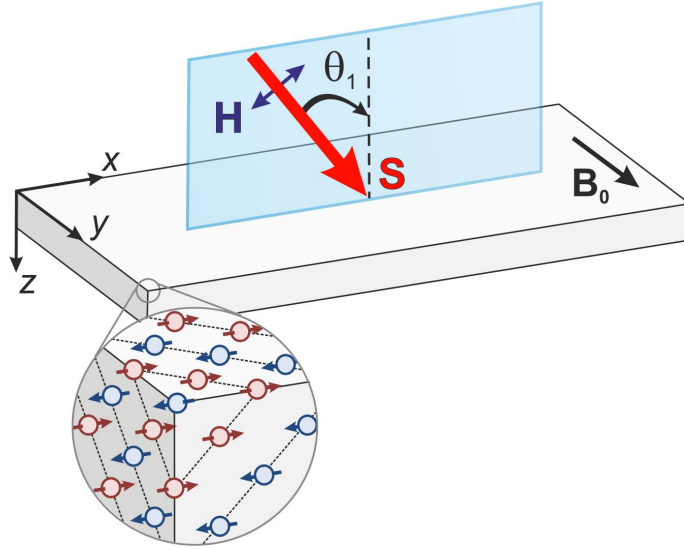


Figure 2.6: Geometry considered in this work: The sublattice magnetisation and anisotropy fields are parallel to the surface and directed along $+x$ and $-x$ axes. The inset shows the spin anti-parallel arrangement in an antiferromagnetic slab. The incident radiation is considered to be transverse electric (TE) polarised.

We assume radiation of wave vector \mathbf{k} propagating in the incidence plane xz . Thus, to derive the form of the dispersion relation we need to decompose \mathbf{k} . If the angle of incidence is represented as θ_1 , the in-plane wave vector component k_x is the same across all layers and is given by

$$k_x = \frac{\omega}{c} \sin \theta_1 \quad (2.28)$$

The z component of the wave vector, however, assumes distinct forms through the different layers. Maxwell's equations may be employed in the two media to find the z component of the wave vector. For the first (vacuum) layer lying in the $z \leq 0$ half-space, one has the usual wave equation for $\vec{E}(\vec{x}, t)$:

$$\left(\nabla^2 + \frac{\omega^2}{c^2} \right) \vec{E}(\vec{x}, t) = 0. \quad (2.29)$$

Considering a TE propagating electromagnetic wave we have:

$$\vec{E}(\hat{x}, t) = \hat{y} E^< e^{ik_x x} e^{-ik_{z1} z} e^{-i\omega t}. \quad (2.30)$$

Replacing $\vec{E}(\hat{x}, t)$ in the wave equation shown in Eq. 2.29, we then find

$$k_x^2 + k_{z1}^2 = \frac{\omega^2}{c^2}. \quad (2.31)$$

In the second (antiferromagnet) layer, it is necessary to rewrite the constructive relations show in Eq. 2.26 and 2.27. We consider the general case when an external field is non-zero so that the permeability has to be replaced by Eq. 2.24. The behaviour of propagating waves in the material also depends on the plane of polarisation of the incident waves.

First consider the modes in which the magnetic field lies transverse (TM) to the incidence plane (electric field along y axis). In this case the propagating magnetic field is given by

$$\vec{H}(\vec{x}, t) = \hat{y} H e^{ik_x x} e^{ik_z z} e^{-i\omega t} \quad (2.32)$$

and the corresponding \vec{D} field is [from Eq. 2.25d]

$$\vec{D}(\vec{x}, t) = \left(-\hat{i} \frac{i}{\omega} \frac{\partial H(x, y)}{\partial z} + \hat{k} \frac{i}{\omega} \frac{\partial H(x, y)}{\partial x} \right) e^{-i\omega t}. \quad (2.33)$$

Using Eqs. (2.26)–(2.27) and Eqs. (2.32)–(2.33) in Eq. (2.25b) we obtain the following equation:

$$\left(\frac{1}{\varepsilon_0 \mu_0} \left(\frac{\partial^2}{\partial z^2} + \frac{\partial^2}{\partial x^2} \right) + \mu_{yy} \varepsilon \omega^2 \right) E(x, y) = 0 \quad (2.34)$$

Using Eqs. 2.34 and 2.32, and considering $c = (\mu_0 \varepsilon_0)^{-1/2}$, we obtain the dispersion relation for TM modes :

$$k_x^2 + k_z^2 = \frac{\omega^2}{c^2} \varepsilon \mu_{yy} \quad (2.35)$$

Thus, for each value of the wave vector, two frequencies are allowed. In Fig. 2.7, we present a plot of the TM polariton dispersion curve described by equation 2.39. As one can see from a glance at the figure, the dispersion relation differs from a constant, this happen due to the contribution of the μ_{yy} permeability tensor component which is resonant.

We see in Fig. 2.7 two regions where bulk polaritons may exist, and the gap between these regions is the evanescent region where polaritons are forbidden to propagate. This region is the frequency gap between ω_0 and ω_s which is where μ_{yy} is negative and ω_s is the frequency at which μ_{yy} vanishes.

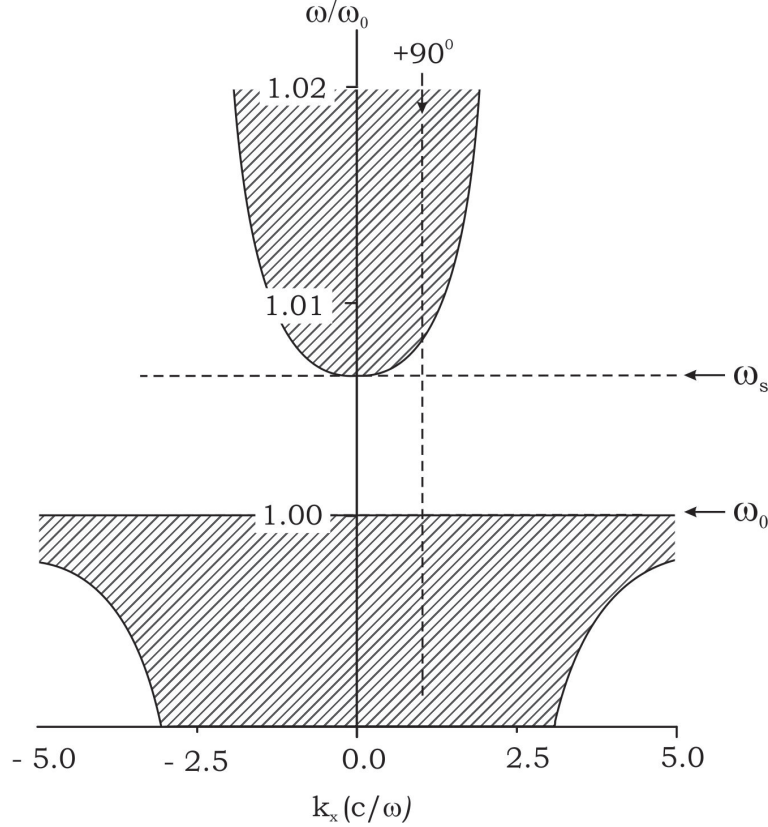


Figure 2.7: Polariton dispersion relation around frequencies where the electromagnetic field of TM polarised radiation interacts with the spins of MnF_2 in the absence of an externally applied field. ω_0 is the resonance frequency and ω_s is the frequency where μ_{zz} vanishes. The shaded regions represent propagation inside the material and evanescent waves, without propagation, is seen elsewhere.

This behaviour is the same as the one shown for a single phonon-polariton resonance. The evanescent region appears in the limit $k_x \rightarrow \infty$ since $k_x \gg \epsilon_{\parallel} \mu_{yy}$, k_{z2} becomes wholly imaginary when there is no damping.

Now we turn to the modes in which the electric field lies transverse (TE) to the incidence plane (along the y axis). In this case the propagating \vec{E} field is given by

$$\vec{E}(\vec{x}, t) = \hat{y} E e^{ik_x x} e^{ik_{z2} z} e^{-i\omega t} \quad (2.36)$$

and the corresponding \vec{B} field is [from Eq. 2.25d]

$$\vec{B}(\vec{x}, t) = \left(\hat{i} \frac{ic}{\omega} \frac{\partial E(x, y)}{\partial z} - \hat{k} \frac{ic}{\omega} \frac{\partial E(x, y)}{\partial x} \right) e^{-i\omega t}. \quad (2.37)$$

We assume that E is a function of x and z but not y . This is reasonable since we only considered propagation in the z direction with no dependence in y .

As in this plane of polarisation the magnetic fields interacts with all resonant components of the permeability given by Eq. 2.24 the dispersion relation is more complicated. It can, however, be and can be found using Maxwell's equations, previously written in Eqs. (2.26)–(2.27), combined with the propagating fields in the material given by Eqs. (2.36)–(2.37) in a similar manner as the one employed by Camley and Mills [61]. Thus, we obtain the following relation:

$$\left(\frac{1}{\mu_{xx}\mu_{zz} + \mu_{xz}^2} \left(\mu_{zz} \frac{\partial^2}{\partial z^2} + \mu_{xx} \frac{\partial^2}{\partial x^2} \right) + \frac{\omega^2}{c^2} \varepsilon \right) E(x, y) = 0 \quad (2.38)$$

Using Eqs. 2.38 and 2.32 we obtain

$$k_{zz}^2 \mu_{zz} + \mu_{xx} k_x^2 = \frac{\omega^2}{c^2} \varepsilon (\mu_{xx} \mu_{zz} - \mu_{xz}^2) \quad (2.39)$$

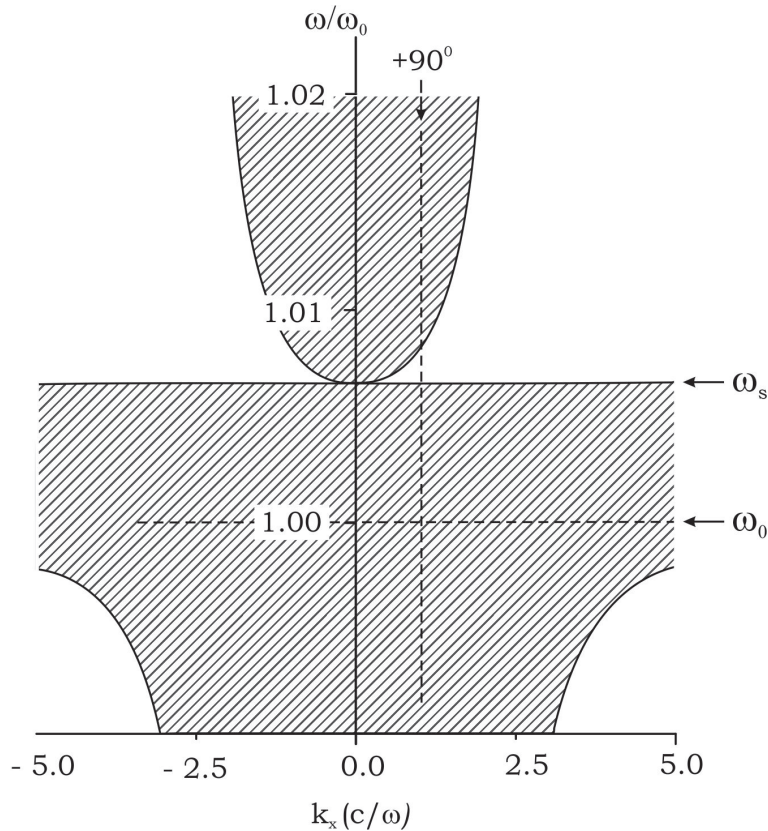


Figure 2.8: Polariton dispersion relation around frequencies where the electromagnetic field of TE-polarised radiation interacts with the spins of MnF_2 in the absence of an externally applied field. ω_0 is the resonance frequency and ω_s is the frequency where μ_{zz} vanishes. The shaded regions represent propagation inside the material and evanescent waves, without propagation, is seen elsewhere.

Here, in a geometry which allows the spins to cant there are two bulk continuum

regions, shown as shaded in Fig. 2.8. These regions are characterized by k_{z2} wholly real, which means radiation can propagate through the crystal. Bulk polaritons are known to be reciprocal in k_x ($\omega(+k_x) = \omega(-k_x)$), i.e., they propagate with the same frequency in both directions $+k_x$ or $-k_x$. Differently from the classic Voigt geometry (magnetic field parallel to the easy axis) studied by Camley and Mills [61], in our case propagation is possible for all frequencies when $k_x = 0$.

The antiferromagnetic resonance (ω_0) can be seen below the transition and the frequency where the permeability vanishes (ω_s) is located at the transition which means the region in between ω_0 and ω_s is where μ_{zz} is negative.

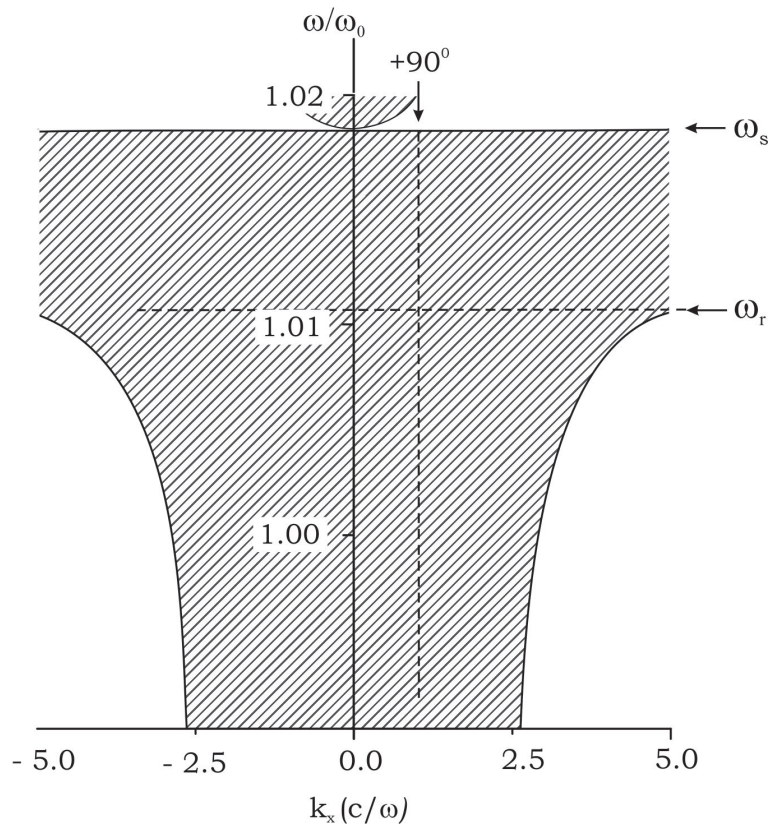


Figure 2.9: Polariton dispersion relation around frequencies where the electromagnetic field of s-polarised radiation interacts with the spins of MnF_2 in the presence of an externally applied field $\mathbf{B}_0 = 1.5$ T. ω_\perp is the resonance frequency and ω_s is the frequency where μ_{zz} vanishes. The shaded regions represent propagation inside the material and evanescent waves, without propagation, is seen elsewhere.

Fig. 2.8 shows that the application of an external field does not radically alter the shape of the bulk bands. However, the resonance frequency ω_r is now at higher frequencies which makes the transition between the two bulk bands also

go to higher frequencies. This is in contrast to MnF_2 in a different geometry, where the external field \mathbf{B}_0 lies parallel to the spin alignment direction [61], which shows a radical alteration in the dispersion curves when an external field \mathbf{B}_0 is applied. In the classic Voigt geometry, there are three bulk bands separated by two nonpropagating regions in which k_{z2} is wholly imaginary and there is no propagation. This corresponds to a split in the magnetic resonance in that geometry due to nondegeneracy of spin precession. In the geometry we are interested in here, however, there is a small nonpropagating gap in between the bulk bands for $k_x = 0$, which only happens in the presence of an external magnetic field due to the contribution of the extra non-diagonal components μ_{xz} and μ_{zx} .

2.5 Damping Effects

Up to now, we only explored the properties of antiferromagnets as non-dissipative media. This has been appropriate for enumerating the properties of these excitations as true eigenmodes of the magnetic system and has simplified the analysis of the bulk polaritons and propagation by allowing k_z to be either wholly real or wholly imaginary.

In reality, however, there are a number of important physical processes which need to be taken into consideration, such as scattering events. These are mechanisms of energy transfer out of one spin wave mode into other spin wave mode and ultimately other excitations in the crystal lattice. Such phenomena may generate relaxation of the precessional motion of the spins and in order to consider this we introduce a phenomenological Bloch relaxation time τ . τ is directly proportional to ω_0 and it can be used to determine the damping parameter Γ

$$\Gamma = \frac{1}{\tau}, \quad (2.40)$$

which is been vastly used when fitting experimental spectra. The damping parameter Γ can dramatically decrease the magnitude of the magnon-polariton resonance. This type of effect can specially be seen in real systems as dissipation of energy is commonly seen inside real crystals. It is, thus, essential to include a

damping parameter Γ in the permeability tensor components by means of the replacement $\omega \rightarrow \omega + i\Gamma$. Γ is used in all further calculations for either low or high temperatures and its values are given in Appendix C.

2.5.1 Damping temperature dependence

At temperatures below T_N , the magnetic moment of the spins has anti-parallel alignment. The lower the temperature, the more perfect this alignment will be. However as temperature increases not only the alignment may be affected but also interactions of energy exchange among the spins can happen more easily. As a consequence the damping parameter Γ is extremely dependent on the temperature. As the spin precession and alignment may be affected by these temperature changes, the frequency of resonance ω_0 can be shifted as the temperature varies, and its position has been reported to be inversely proportional to the temperature [55].

In Fig. 2.10 we show the effect of increasing temperature, and hence Γ , on the permeability tensor for MnF_2 . As seen from Fig. 2.3, when $\Gamma = 0$, the branches of the μ_{zz} go to infinity as the frequency approaches ω_0 and its value is never imaginary.

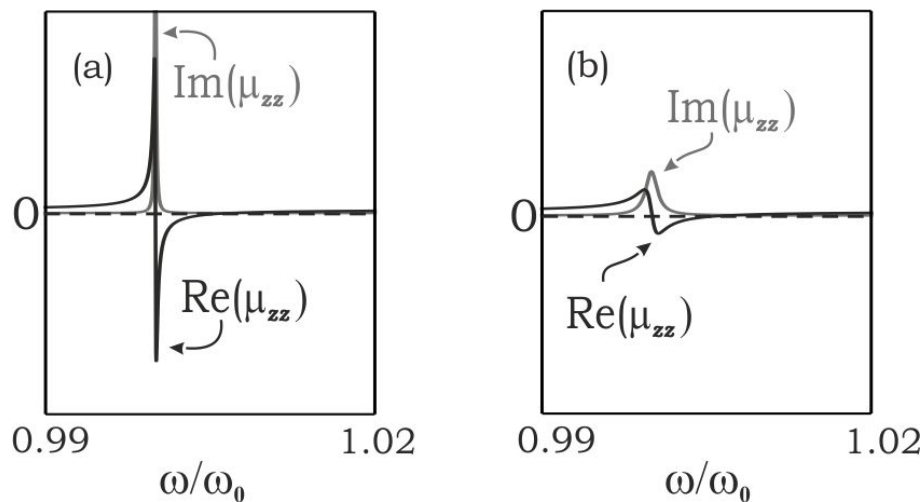


Figure 2.10: Effect of temperature induced damping on the real and imaginary parts of μ_{zz} around the magnon-polariton frequency in MnF_2 for (a) $0.06T_N$ and (b) $0.42T_N$.

When the damping parameter is included ($\Gamma \neq 0$), however, it leads to complex permeability components. The real part of the permeability governs electromagnetic wave propagation in the material and the imaginary part determines the

absorption of electromagnetic energy by the material. For the case show in Fig. 2.10(a), for $0.06T_N$ the imaginary part of μ_{zz} is extremely small over almost the entire range, suggesting that, transmission across that range of frequencies should be extremely efficient.

When the temperature is risen to $0.42T_N$, not only the imaginary part widens up, becoming comparable to the real part of μ_{zz} , but also the peak on the real part becomes much weaker.

In both cases MnF_2 still works as an indefinite medium. However, if the temperature rises considerably, closer to T_N , this behaviour may disappear since the resonance may never cross into negative values.

Spin canting induced Goos-Hänchen shifts

3.1 Reflection and Goos-Hänchen shifts	36
3.2 Zero field Goos-Hänchen shifts	38
3.3 Tunable shifts with $\mathbf{B}_0 \neq 0$	42
3.3.1 Oblique incidence	44
3.3.2 Normal incidence	46
3.4 Conclusions	49

There has been interest in the reflection from magnetic crystals such as antiferromagnets, because the reflection can be non-reciprocal, i.e., reversing the direction of the incident waves or externally applied field leads to a different reflection coefficient [60, 62]. Nonreciprocal reflection has been vastly studied theoretically [62, 60, 63, 53, 64, 65] and experimentally [66, 67, 68, 69] in the antiferromagnet classic Voigt geometry, which is when the plane of incidence is perpendicular to the magnetic field and the field is parallel to spin orientation (easy axis). In such geometry, nonreciprocity happens when a magnetic field is externally applied as the field induces non-degeneracy of the spins precession.

Nonreciprocity in magnetic crystal can be of particular interest when investigating optical effects such as lateral shifts on the externally reflected beam, the so called Goos-Hänchen shift [30]. In the case of the Goos-Hänchen shift associated with reflection from antiferromagnets, the effect stems from the fact that, at terahertz frequencies, the magnetic component of electromagnetic radiation can interact with the spin precession near magnon-polariton resonances. The resulting shift

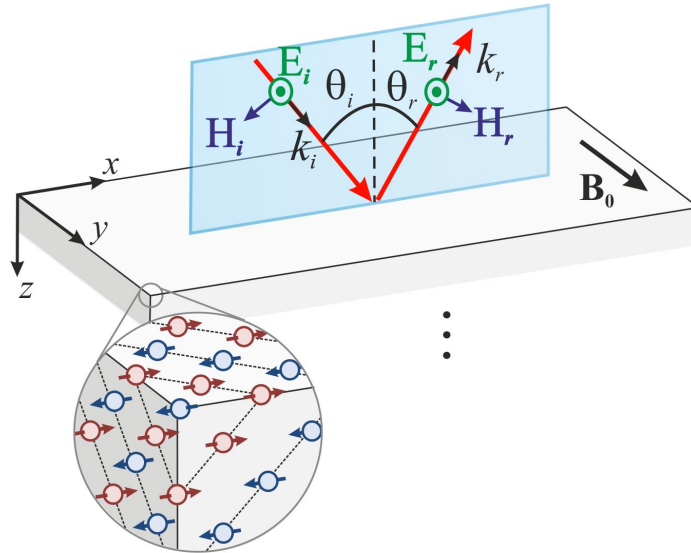


Figure 3.1: Schematic representation of an oblique incident beam with an angle θ_1 being displaced on the reflection by a distance D at the interface between vacuum and an antiferromagnet, where S_i and S_r are the incident and reflected Poynting vector respectively.

may become nonreciprocal in the presence of an suitably applied external field \mathbf{B}_0 . Up to now, studies of Goos-Hänchen shifts in reflection from antiferromagnets have considered only the situation where \mathbf{B}_0 is applied along the anisotropy axis, perpendicular to the plane of incidence [30, 28, 29].

In this work we are interested in a geometry in which the easy axis is parallel to the plane of incidence and the external field is applied perpendicular to the both of them, which makes the spins to cant towards the field direction (as discussed in Chapter 2). In this geometry, nonreciprocity happens because the precession may not happen in-phase when the spins are canted.

3.1 Reflection and Goos-Hänchen shifts

We are interested in the Goos-Hänchen shift for reflection at the boundary between vacuum and a semi-infinite antiferromagnetic crystal as aligned in the coordinate system depicted in Fig. 3.1. The material occupies the $z > 0$ half space with the easy axis along x . The plane of incidence is xz , z being normal to the interface and the principal axes of the crystal tensor lie along the Cartesian axes x , y and z . An applied magnetic field lies perpendicular to both the easy axis and the plane of incidence (along y).

We consider the incident radiation to be plane polarised. In the case of a TE polarised beam (\mathbf{E} field normal to the plane of incidence), the radiation interacts with μ_{xx} , μ_{zz} and $\mu_{xz} - \mu_{xx}$ and μ_{zz} being of opposite signs close to the magnon-polariton resonance (frequency regime $\omega_r \leq \omega \leq \omega_s$).

If the angle of incidence is θ_1 , the in-plane wavevector component k_x of a plane wave will be given by

$$k_x = \frac{\omega}{c} \sin \theta. \quad (3.1)$$

We can conveniently consider a finite beam as a sum of plane waves with varying k_x . For each k_x value, we have a complex reflection coefficient r which may be represented in the form

$$r(k_x) = \rho(k_x) e^{i\phi(k_x)}, \quad (3.2)$$

where $\rho(k_x)$ is the reflection amplitude and $\phi(k_x)$ is the associated phase change on reflection. Since this phase change may vary with k_x , interference between the reflected plane waves can lead to a change in the profile of the reflected beam. In fact, using this angular spectrum approach, McGuirk and Carniglia [22] have shown that, to a first approximation, this profile change simply amounts to a lateral shift D of the reflected beam, and that this shift is given by

$$D = - \left. \frac{d\phi}{dk_x} \right|_{k_x=k_{x0}}. \quad (3.3)$$

which is also the result obtained by Artmann [21], who considered interference between two plane waves. The result was originally obtained for the case of total reflection (i.e. $\rho = 1$), but is valid even when this condition does not apply [70]. A simple way of evaluating D makes use of the fact that both ρ and ϕ are, by definition, real. If the logarithm of 3.2 is taken, it is straightforward to resolve the equation into real and imaginary parts, and 3.3 becomes [71]

$$D = -Im \left(\frac{1}{r} \frac{dr}{dk_x} \right). \quad (3.4)$$

In order to understand how the above shift will occur in practice, we look at the

explicit expressions for the complex reflection coefficient r . Combining Maxwell's equations we can find the components of \vec{E} in terms of $\vec{\mu}(\omega)$, which is given by Eq. 2.5, and the components of wave vector \vec{k} . From there we can calculate the reflectance which is defined as

$$r = \frac{E_r}{E_i} \quad (3.5)$$

3.2 Zero field Goos-Hänchen shifts

As a first approach, in order to investigate lateral shifts on the reflection from an antiferromagnetic crystal, we take $\mathbf{B}_0 = 0$. The permeability tensor is then diagonal and r reduces to

$$r = \frac{(\mu_{xx}k_{z1} - k_{z2})}{(\mu_{xx}k_{z1} + k_{z2})} \quad (3.6)$$

with k_{z1} and k_{z2} represent the z components of the wavevectors in the two media and are given by

$$k_{z1}^2 = \frac{\omega^2}{c^2} - k_x^2 \quad (3.7)$$

$$k_{z2}^2 = \varepsilon\mu_{xx}\frac{\omega^2}{c^2} - \frac{\mu_{xx}}{\mu_{zz}}k_x^2 \quad (3.8)$$

here ε represents the dielectric constant of the antiferromagnet.

Replacing the equations above for r into 3.3 it gives

$$D = -Im \left[\frac{2\mu_{xx}k_x(\mu_{xx}k_{1z}^2 - \mu_{zz}k_{2z}^2)}{\mu_{zz}k_{1z}k_{2z}(\mu_{xx}^2k_{1z}^2 - k_{2z}^2)} \right] \quad (3.9)$$

In order to get a more intuitive picture of the implications of these equations, it is useful to consider the beam behaviour in the absence of absorption, in which case all the dielectric tensor components will be real and k_{2z} will always be wholly real or wholly imaginary as discussed in Chapter 2. When k_{2z} is real, we can see from Eq. (3.6) that r will always be real. The phase is thus either zero or $\pi/2$, so that D is always zero (see (3.4)). Thus we see that an imaginary k_{2z} , leading a

“reststrahl” region, i.e., total reflection, is necessary to obtain a lateral shift. When TE polarised waves shine on an antiferromagnetic surface a sign combination of μ_{xx} , μ_{zz} and the incident angle θ need to be taken into consideration when determining whether k_{2z} is real or imaginary. These conditions have been discussed before and are summarized by the dispersion relation shown in Fig. 2.7, in which the unshaded regions correspond to imaginary k_{2z} (total reflection). In the shaded regions there is transmission within the crystal.

Since, in the absence of absorption, we are only interested in the totally reflecting regions where k_{2z} is imaginary, in this region Eq. 3.9 turns into:

$$D = \frac{2\mu_{xx}^2 k_x (1/\mu_{xx} - 1)}{k_{1z} k_{2z} (\mu_{xx}^2 k_{1z}^2 + k_{2z}^2)}. \quad (3.10)$$

In the presence of absorption, the tensor components will, in general, be complex, as will k_{2z} . There will thus not be a strict division between propagating and reflecting regions.

We now apply our theory to reflection of TM-polarised radiation obliquely incident at a vacuum/MnF₂ interface. MnF₂ is a well characterized antiferromagnet that can be readily prepared and studied experimentally. In Fig. 3.2(a) we present the calculated plane wave reflectance $R = rr^*$ spectra, obtained using Eq. (3.6), for incident angles of $\pm 60^\circ$. Results with and without damping Γ are shown. In each case, there is no difference between the $\theta_1 = +60^\circ$ and the $\theta_1 = -60^\circ$ reflectivity, i.e. the reflectivity is reciprocal $R(\theta_1) = R(-\theta_1)$. This is expected from simple symmetry arguments [62].

In the case when $\Gamma = 0$, k_{2z} is either wholly real or imaginary. In the case of k_{2z} real, propagation through the antiferromagnet can occur. These regions are indicated by shading in the figures. In the case of k_{2z} imaginary, reflection is total, with no propagation into the antiferromagnet. These are reststrahlen regions. For μ_{xx} positive, the reststrahlen condition is $0 < \mu_{zz} < (1/\epsilon) \sin^2 \theta_1$ which, providing $\theta_1 \neq 0$, is satisfied in a narrow frequency region [49] just above the zero in μ_{zz} . In the configuration considered here, the reststrahlen region only exists at oblique incidence, and its width depends on the angle of incidence. In Fig. 3.2(a) it is seen that, in the zero damping case (dashed lines), the reflectivity is unity within this region and smaller elsewhere.

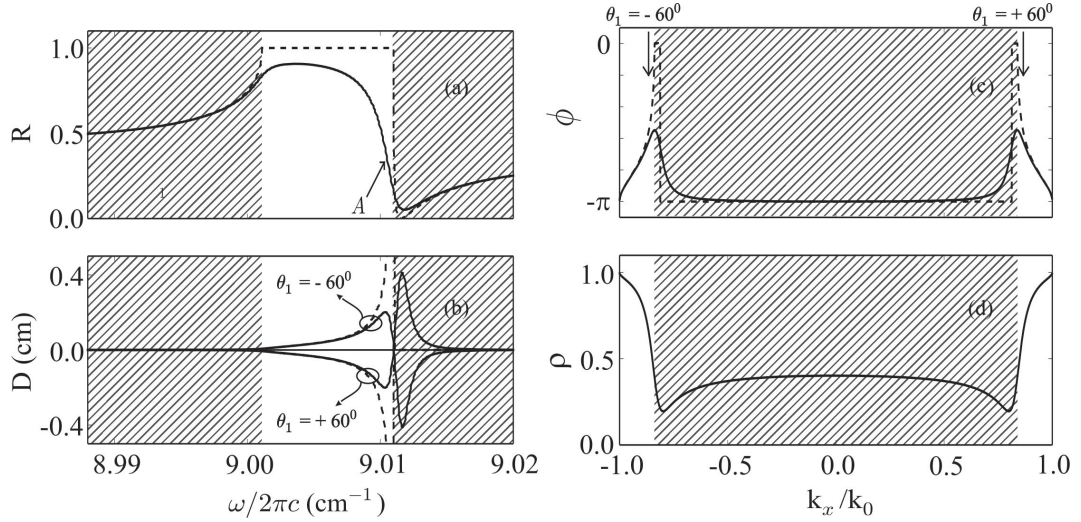


Figure 3.2: (a) Calculations of s -polarised oblique incidence ($\theta_1 = \pm 60^\circ$) reflection from the interface between vacuum and MnF_2 and (b) Goos-Hänchen shift D . Reflected (c) phase and (d) amplitude, as a function of in-plane wavevector k_x , at the frequency marked as A in (a) (9.0103 cm^{-1}) for the configuration shown in Fig. 3.1. Dashed lines are calculated for $\Gamma = 0$, whereas solid lines are for calculations in which $\Gamma = 0.0007 \text{ cm}^{-1}$. The shaded regions show where transmission is possible in the absence of damping. In case (a) the curves corresponding to $\theta_1 = \pm 60^\circ$ are coincident, so only a blue curve is seen in the case of the solid lines. Note that, in part (c), $\phi = \pi$ is represented as $\phi = -\pi$ in the $\Gamma = 0$ curve for consistency with the $\Gamma = 0.0007 \text{ cm}^{-1}$ curve.

In Fig. 3.2(b) we show the Goos-Hänchen shifts calculated according to Eq. (3.3). In a similar manner to the result seen for reflectivity, these shifts are found to be reciprocal, which in this case corresponds to the relation $D(+\theta_1) = -D(-\theta_1)$. In the absence of damping, the shifts are nonzero only in the reststrahlen region. This is similar to the behavior of Goos-Hänchen shifts associated with the phonon response in dielectric crystals [27], and can be explained by the fact that in the propagation regions the phase is either 0 or π (i.e. r is wholly real) but in the reststrahlen regions it takes on other values.

Since the displacement D depends on the derivative of the reflected phase (Eq. (3.4)), it is useful to plot ϕ and ρ as functions of k_x . In Fig. 3.2(c) we show $\phi(k_x)$ at the frequency marked as A in Fig. 3.2(a) (9.0103 cm^{-1}), and in Fig. 3.2(d) we show the corresponding amplitude values ρ , highlighting the values of k_x corresponding to $\theta_1 = \pm 60^\circ$. In the absence of damping, there are important differences between the behavior for $k_x^2/k_0^2 < \epsilon\mu_{zz}$ (i.e. $\sin^2 \theta_1 < \epsilon\mu_{zz}$) and $k_x^2/k_0^2 > \epsilon\mu_{zz}$. In the former case, corresponding to propagation regions, the amplitude ρ is less than 1 and the phase ϕ is constant at 0 or π , so that there is no displacement. In the latter case, corresponding to reststrahlen region behavior, the

amplitude is unity, corresponding to total reflection, and the phase is continuously varying, leading to nonzero displacement. $\theta_1 = \pm 60^\circ$ corresponds to reststrahlen behavior, resulting in the nonzero shift seen in Fig. 3.2 at frequency A . In the presence of damping, the phase in the bulk region is no longer strictly constant, so a Goos-Hänchen shift is also possible for lower angles of incidence, albeit most markedly in low reflectivity regions.

The lateral displacement of a Gaussian beam obliquely incident on a MnF_2 surface is shown in Fig. 3.3. In this case the beam is given by Eq. (D.1) with [29, 45, 49]

$$\psi(k_x) = -\frac{g}{2 \cos \theta_1 \sqrt{\pi}} \exp \left[-\frac{g^2 (k_x - k_{x0})^2}{4 \cos^2 \theta_1} \right], \quad (3.11)$$

where $2g$ represents the beam width at the sample surface and θ_1 is the incident angle.

We take $g \approx 2\lambda$, where λ is the free space wavelength of the radiation. The results in Fig. 3.3 are for the same frequency as that used in Figs. 3.2(c) and 3.2(d), i.e. Frequency A (9.0103 cm^{-1}). At this frequency, even when damping is considered, the reflectivity is large enough to be seen in Fig. 3.3, without using logarithmic scale for the intensity. We clearly see that the incident beam is positively shifted with a large displacement of around $D = 0.2 \text{ cm}$ (approximately 2λ), in line with the results predicted from Fig. 3.2(b).

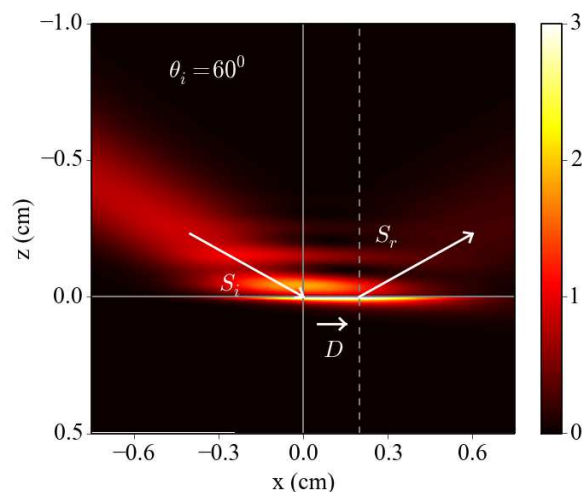


Figure 3.3: Calculated overall power intensity (in terms of the magnitude of the time-averaged Poynting vector) showing intensities for a beam of width $g = 0.2 \text{ cm}$ obliquely incident ($\theta_1 = +60^\circ$) on a vacuum/ MnF_2 interface at the frequency marked as A in Fig. 3.2 (9.0103 cm^{-1}). The arrows represent the incident and reflected beams, positioned according to Eq. (3.3), with angle of reflection assumed equal to angle of incidence.

3.3 Tunable shifts with $\mathbf{B}_0 \neq 0$

Due to the effect of an externally applied field \mathbf{B}_0 on the spins in antiferromagnetic crystals the complex reflection coefficient r can be express in the form

$$r = \frac{k_{z1}(\mu_{xx}\mu_{zz} + \mu_{xz}^2) - k_{z2}\mu_{zz} - k_x\mu_{xz}}{k_{z1}(\mu_{xx}\mu_{zz} + \mu_{xz}^2) + k_{z2}\mu_{zz} + k_x\mu_{xz}}. \quad (3.12)$$

The overall reflectivity is given by $R = rr^*$. For this situation the wave-vector component k_{z2} is calculated from Eq. 2.39 and is given by

$$k_{z2}^2 = \frac{\epsilon k_0^2(\mu_{xx}\mu_{zz} + \mu_{xz}^2) - k_x^2\mu_{xx}}{\mu_{zz}}. \quad (3.13)$$

Without an external magnetic field the effects associated with external reflection from an antiferromagnetic surface are reciprocal. When a field is applied, nonreciprocal effects, either considered with respect to reversing the sign of the incident angle or that of the applied field, are introduced.

The nonreciprocal behavior considered here is associated with the off-diagonal elements μ_{xz} and μ_{zx} of the permeability tensor. They are nonzero only due to the canting of the spins, which results in a small spin component along the applied field direction.

For the geometry shown in Fig. 3.1, spin precession is mainly restricted to the yz plane, with the spins on the two sublattices precessing in opposite directions. However, when the spins are canted toward the y axis, one can consider that there is also a small amount of precession in the xz plane. In this plane, the precession direction is the same for both sublattices, but changes direction when the field direction is reversed. The antiferromagnet is thus gyromagnetic, with nonzero permeability components μ_{xz} and μ_{zx} whose signs depend on the field direction. If the incident field of the electromagnetic radiation has a magnetic component in the xz plane, therefore, nonreciprocal effects, such as nonreciprocal Goos-Hänchen shifts, may be expected in reflection.

Nonzero μ_{xz} and μ_{zx} values are also responsible for the nonreciprocal Goos-Hänchen shifts in the previously studied configuration in which the easy axis is taken parallel to the applied field, along y [30, 28, 29]. In such a configuration,

however, they become nonzero without the necessity of spin canting. Noticeably higher fields are therefore necessary in the present case than in the previously studied one.

In Fig. 3.4 we show the effect on the Goos-Hänchen shifts of applying an external magnetic field for the same geometry as represented in Fig. 3.1. The figure shows how the applied field shifts the resonance, and associated reststrahlen region, to higher frequency. The shift itself becomes distinctly nonreciprocal $D(+\theta_1) \neq -D(-\theta_1)$, as predicted above. However, it is clear that the relationship between the size of the shifts and the applied field is far from linear. This appears to be related to the coupling of the incident beam to surface resonances. A full analysis of this relationship is beyond the scope of the present thesis. Here we analyze in some detail the general behavior of the nonreciprocal shift, using a field of $B_0=1.5$ T as our example.

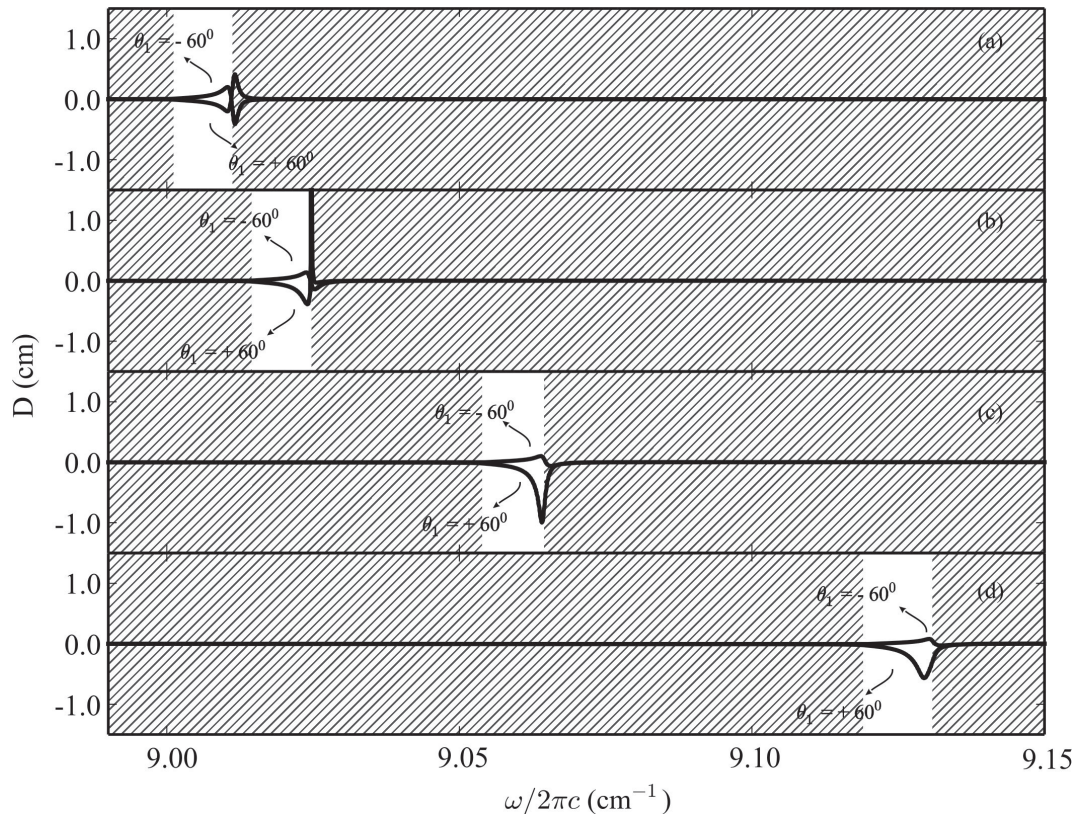


Figure 3.4: Goos-Hänchen shift D for different values of applied external field (a) $B_0 = 0.0$ T, (b) $B_0 = 0.5$ T, (c) $B_0 = 1.0$ T and (d) $B_0 = 1.5$ T. Blue lines are calculated for $\theta_1 = +60^\circ$, whereas red lines are calculated for $\theta_1 = -60^\circ$

3.3.1 Oblique incidence

In Fig. 3.5(a) we show the reflectivity R for oblique incidence ($\theta_1 = \pm 60^\circ$) reflection from an MnF_2 surface with an external magnetic field $\mathbf{B}_0 = 1.5$ T. All features are now at higher frequencies than in Fig. 3.2 due to the higher resonance frequency ω_\perp (Eq. (2.19)). In the case of $\Gamma = 0$ (dashed lines), both positive and negative angles of incidence give the same result. However, when $\Gamma \neq 0$, $R(+\theta_1)$ and $R(-\theta_1)$ are no longer identical. This is an example of the well-known result that the reflectivity is reciprocal in the absence of damping but can be nonreciprocal when damping is present [66, 62, 63, 67].

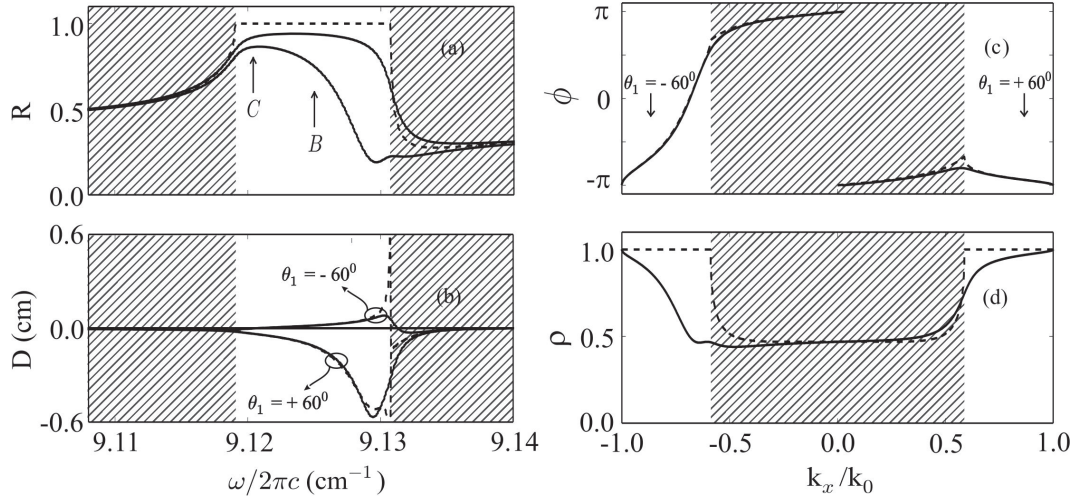


Figure 3.5: (a) Calculations of s-polarised oblique incidence ($\theta_1 = \pm 60^\circ$) reflection from the interface between vacuum and MnF_2 in the presence of an external magnetic field of 1.5 T and (b) Goos-Hänchen shift D . Reflected (c) phase and (d) amplitude, as a function of in-plane wavevector k_x , at frequency marked as B (9.125 cm $^{-1}$) in (a). Dashed lines are calculated ignoring damping, whereas solid lines are for calculations in which damping is included. The shaded region shows frequencies where transmission can occur in the absence of damping.

In Fig. 3.5(b) we show the corresponding Goos-Hänchen shifts. It is immediately seen that the shifts are distinctly nonreciprocal $D(+\theta_1) \neq -D(-\theta_1)$, either with or without damping. Furthermore, there are nonreciprocal shifts some way into the propagation region. Indeed, in the absence of damping, we observe the somewhat counterintuitive property $D(+\theta_1) = D(-\theta_1)$ in this region. Alternatively one could say that, for some given incident angle, reversing the field direction would change the sign of D without changing its amplitude. This result has also been shown for the case of the easy axis perpendicular to the plane of incidence [30].

In Fig. 3.5(c) we show the reflected phase ϕ as a function of k_x at the frequency marked as B in Fig. 3.5(a) (9.125 cm^{-1}). In 3.5(d) we show the corresponding amplitude ρ . The nonreciprocal phase behavior is similar to that discussed by Dumelow *et. al.* [65], and leads to nonreciprocal Goos-Hänchen shifts. For smaller incident angles, corresponding to transmission region behavior ($-0.6 < k_x/k_0 < 0.6$), the amplitude is less than unity in the absence of damping, as in the zero field case. However, the phase is no longer simply 0 or π in this region. It is in fact antisymmetric about $k_x = 0$, so that $\phi(k_x) = -\phi(-k_x)$. This can be shown by resolving Eq. (3.12) into real and imaginary terms (recalling that μ_{xz} is imaginary in the absence of damping, all other terms being real), and leads to equal derivatives for positive and negative k_x , giving the result discussed above ($D(+\theta_1) = D(-\theta_1)$) for the transmission region frequencies.

For the situation shown in Fig. 3.5 we are interested in the phase derivative at $\theta_1 = \pm 60^\circ$ (shown as red arrows in Fig. 3.5(c)). This corresponds to reststrahlen behavior, as anticipated from Fig. 3.5. $d\phi/dk_x$ is clearly nonzero and its magnitude is different for positive and negative angles, in agreement with Fig. 3.5(b), in which nonreciprocity in the Goos-Hänchen shift can be seen. In the absence of damping the amplitude values ρ for positive and negative values of k_x are exactly the same, confirming the results already discussed in relation to Fig. 3.5(b).

Using the plane wave spectrum model represented by Eqs. (D.1) and (3.11), we can simulate a Gaussian beam reflected from an antiferromagnet specimen (as in Fig. 3.3) in the presence of a nonzero external magnetic field. In the present case we are using the same conditions as in Fig. 3.5(c). In Fig. 3.6(a), we show results for a positive incident angle $\theta_1 = +60^\circ$, corresponding to a small displacement of approximately $+0.03 \text{ cm}$, as expected from Fig. 3.5(b). In Fig. 3.6(b) we show the case for $\theta_1 = -60^\circ$. In this case we can observe a displacement of about -0.1 cm (i.e., $D \simeq -\lambda$), which also agrees with the results shown in Fig. 3.5(b). Thus, although the sign of the displacement has changed, as expected, the amplitude is considerably larger than in the $\theta_1 = +60^\circ$ case, confirming that the Goos-Hänchen shift is nonreciprocal.

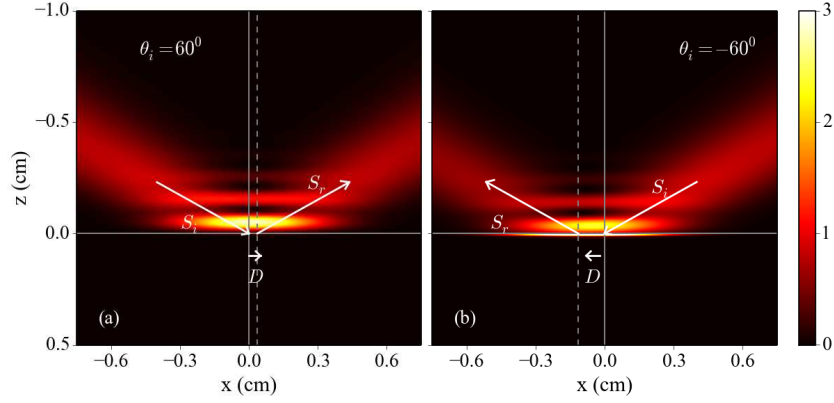


Figure 3.6: Calculated overall power intensity (in terms of the magnitude of the time-averaged Poynting vector) showing intensities for a beam of width $g = 0.2$ cm obliquely incident on a vacuum/ MnF_2 interface at frequency B ($\omega = 9.125 \text{ cm}^{-1}$) in the presence of a magnetic field $B_0 = 1.5$ T. (a) $\theta_1 = +60^\circ$; (b) $\theta_1 = -60^\circ$. The arrows represent the incident and reflected beams, positioned according to Eq. (3.3), with angle of reflection assumed equal to angle of incidence.

3.3.2 Normal incidence

We now consider the possibility of a normal incidence Goos-Hänchen shift of the type discussed by Lima *et. al.* [28, 29] for the case of the antiferromagnet easy axis parallel to the applied field. In the absence of an external field, the reflected phase is reciprocal [i.e., $\phi(+k_x) = \phi(-k_x)$], so $d\phi/dk_x$ will be zero at normal incidence ($k_x = 0$), resulting in a zero shift. In fact, as discussed in Section II, there is no reststrahlen region associated with normally incident radiation, and no magnon-polariton related phenomena are expected. In the presence of a nonzero external field, however, due to the more complex nature of the permeability tensor represented by Eq. (2.24), a narrow reststrahlen region does appear at normal incidence. This can be seen from Fig. 3.7(a), which shows the normal incidence reflectivity in the presence of a an applied field of 1.5 T, i.e., the same configuration as in the Fig. 3.5 but at normal incidence. We can see that there is a narrow reststrahlen region, centered around 9.12 cm^{-1} . In this region, the reflectivity is unity in the absence of damping, although it is considerably less in the presence of damping.

Figure 3.7(b) shows the normal incidence Goos-Hänchen shift, which is nonzero both inside and outside the reststrahl region. At frequency B , in the bulk region, there is small negative shift, as predicted from Fig. 3.5(c). At frequency C (9.1204 cm^{-1}), within the reststrahlen region, however, a considerably larger

displacement of about -0.05 cm is observed with a reasonable reflectivity.

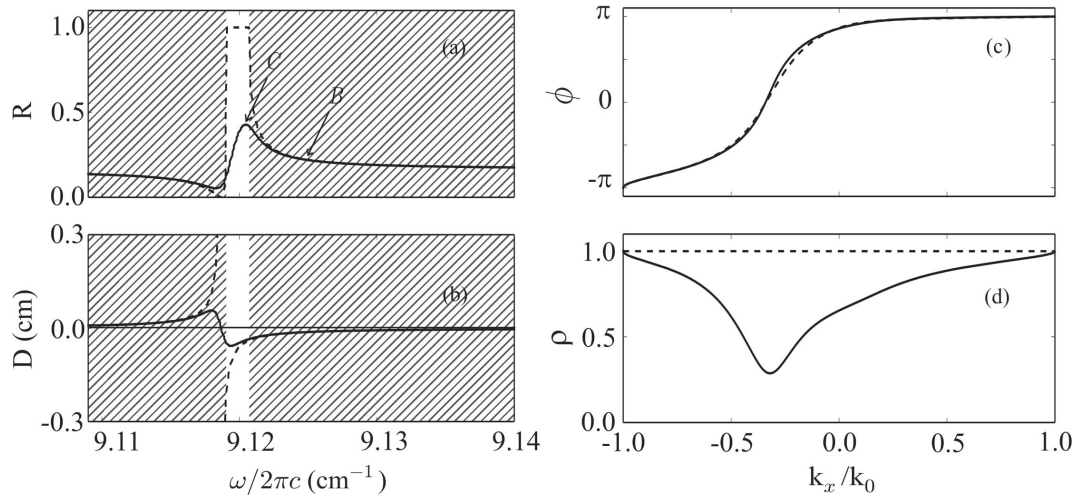


Figure 3.7: Normal incidence calculations in the presence of an external magnetic field of 1.5 T. (a) Plane wave reflectivity spectrum; (b) Goos-Hänchen shift D . Reflected (a) phase and (b) amplitude, as a function of in-plane wavevector k_x , for s -polarised reflection from a MnF_2 crystal at the frequency marked in C as (a) (9.1204 cm^{-1}), in the presence of an external magnetic field of 1.5 T. Dashed lines are calculated ignoring damping, whereas solid lines are for calculations in which damping is included. The shaded regions show where transmission can occur in the absence of damping.

The reflected phase ϕ (Fig. 3.7(c)) and the amplitude ρ (Fig. 3.7(d)) are shown, as a function of k_x , for frequency C. The dashed lines show results without damping and the solid lines show results with damping included. At this frequency, reststrahlen behavior is present for all incident angles, so the amplitude is always unity, ignoring damping. It is seen that $\phi(k_x)$ is nonreciprocal and has nonzero derivative when k_x is zero, with or without damping. This results in a significant nonzero Goos-Hänchen shift consistent with Fig. 3.7(b).

The lateral displacement at frequency C (see Fig. 3.7(a)) can be seen in Fig. 3.8 where we show the beam intensity profile (i.e. $|E|^2$) of a normally incident beam. For this simulation we use the model described by Eqs. (D.1) and (3.11). However, when θ_1 is equal to zero, the function ψ reduces to

$$\psi(k_x) = -\frac{g}{2\sqrt{\pi}} \exp\left(-\frac{g^2 k_x^2}{4}\right). \quad (3.14)$$

For a normal incidence we increase the width of the beam to $g \approx 5\lambda$ in order to better simulate the wide beam approximation inherent in Eq. (D.17). We can see clearly from the resulting profile in Fig. 3.8 that there is a shift of the reflected beam at the sample surface in accurate agreement with the result shown in Fig.

3.7, based on Eq. (3.3). The vertical solid line represents the center of the incident beam at $x = 0$, and the vertical dashed line represents the center of the reflected beam, which is slightly dislocated to the left ($x = -0.04$ cm).

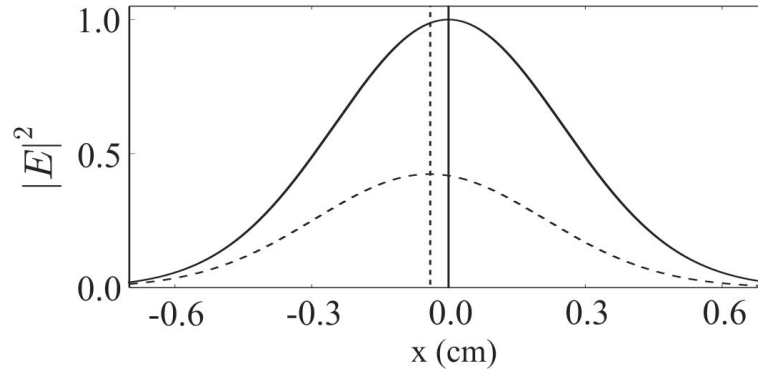


Figure 3.8: Intensity profiles of the incident (solid curve) and reflected (dashed curve) gaussian beam of width $g = 0.5$ cm, at the frequency marked as C as Fig. 3.7 (9.1204 cm^{-1}), normally incident on MnF_2 in the presence of a magnetic field $B_0 = 1.5$ T, with damping effects taken into account. The vertical solid line represents the center of the incident beam ($x = 0$) and the vertical dashed line represents the center of the reflected beam ($x = -0.04$ cm).

In addition to using Fig. 3.7(c) in interpreting normal incidence results, we make some additional observations with regard to its use in interpreting Goos-Hänchen shifts at oblique incidence at frequency C . Firstly, at this frequency, it is seen that $d\phi/dk_x$ is always positive regardless of the sign of k_x , so the sign of the shift should always be negative regardless of the sign of the incident angle (alternatively, reversing the sign of the applied field would always change the sign of the shift). We can see this using the example of $\theta_1 = \pm 60^\circ$, already considered in the previous section. Figure 3.5(b) confirms that the expected behavior does indeed occur at frequency C . For $\theta_1 = +60^\circ$, there is a very small negative displacement, reflecting the fact that the derivative of $\phi(k_x)$ is small and positive. For $\theta_1 = -60^\circ$, there is a somewhat larger negative displacement, as predicted from the derivative of the $\phi(k_x)$ curve in Fig. 3.7(a).

A second observation with regard to this figure concerns a comparison of the phase behavior in Fig. 3.7(c) with the amplitude behavior in Fig. 3.7(d). As can be seen, the amplitude turns out to be extremely nonreciprocal when damping effects are included. In fact it reaches a minimum within the negative k_x regime where the phase has a large derivative, i.e. where the shift D will be large. When this occurs, both k_x and D are negative, i.e., they are both in the same direction,

resulting in what would normally be described as a positive Goos-Hänchen shift. This implies an increased penetration into the antiferromagnet, so it is reasonable to expect a higher absorption. In the case of a negative Goos-Hänchen shift (positive k_x) there is less penetration, and hence less absorption [30]. The reflectivity dip at negative k_x is actually an example of coupling to a surface resonance, and the associated phase behavior confirms that this coupling has a drastic effect on the nonreciprocal Goos-Hänchen shifts.

3.4 Conclusions

We have considered the reflection of terahertz radiation from an uniaxial antiferromagnetic crystal (MnF_2) with its uniaxis in the plane of incidence, parallel to the antiferromagnet surface. We find that large Goos-Hänchen shifts ($D \approx 0.2 \text{ cm}$) for external reflections from an antiferromagnetic crystal are possible. Using an s -polarised terahertz beam, we show that, in the absence of an external magnetic field, these shifts are reciprocal ($D(+\theta_1) = -D(-\theta_1)$), and only occur in the reststrahlen regions. These regions only exist at oblique incidence and are much narrower than when the spins are perpendicular to the plane of incidence (the case studied by Lima *et. al.* [30]).

We have shown that a magnetic field B_0 externally applied perpendicular to the uniaxis can induce nonreciprocity. This nonreciprocity is associated with a spin component parallel to the applied field. This particular spin component only exists due to canting of the spins, and for this effect to be evident somewhat higher fields than in the previously studied case, in which the uniaxis is parallel to the field, are necessary. The magnitude of non-reciprocal effects is largely associated with coupling of the incident radiation to surface resonances, and this aspect deserves further study.

Even though resonances in natural crystals have been previously used to obtain lateral displacements on reflection, considering the dielectric function in isotropic crystals [72], the use of resonances in the magnetic permeability of antiferromagnets still presents some limitations for experimental works. In the geometry considered in this work, as well as the one presented by Lima *et. al.*, the

need for low temperatures limits the possibilities for experimentation. However, antiferromagnetic crystals at room temperature possessing high reflection regions, such as NiO may be a suitable candidate for experiments.

Antiferromagnets as Negative Refractive Media

4.1 Indefinite permeability tensor	52
4.1.1 Hyperbolic dispersion	53
4.2 Power Flow Analysis	55
4.3 Effects of externally applied fields	57
4.4 Snell's Law and Negative Refraction	61
4.4.1 Effective index of refraction in Antiferromagnets . . .	61
4.5 Figure of Merit	63
4.6 Nonreciprocity	64
4.7 Conclusions	66

The origins of the concept of a medium that could refract waves negatively dates back to the work done by Veselago in 1968 [8]. He showed that when electromagnetic waves propagate through a medium possessing $\mu < 0$ and $\varepsilon < 0$ they are bent backwards to the opposite direction, differently from what would be predicted by geometric optics. When this condition is satisfied, the \mathbf{E} , \mathbf{H} and \mathbf{k} vectors form a left-handed triplet. As a result the wave vector \mathbf{k} and the Poynting vector \mathbf{S} are oriented in opposite directions and that is the definition of negative index materials $n < 0$.

As an alternative approach to materials with $n < 0$, negative refraction of the power flow has been demonstrated in highly anisotropic nonmagnetic media due to hyperbolic dispersion [73, 74]. However, similar behaviour should be expected in magnetic media displaying indefinite permeability (i.e. have a

permeability tensor containing components of opposing signs) in similar manner to the indefinite permittivity found in certain anisotropic crystals. In this type of media hyperbolic dispersion and similar effects to those found for indefinite permittivity media should be possible.

In the present Chapter, we investigate hyperbolic properties in antiferromagnetic media. We concentrate on the case of uniaxial antiferromagnets, confirming that all-angle negative refraction should indeed be possible in such materials. In addition, we show that, differently from nonmagnetic crystals, the angle of refraction should be tunable by applying an external magnetic field. We investigate absorption effects by investigating a large figure of merit as well as nonreciprocity of the angle of refraction when an external field is applied.

4.1 Indefinite permeability tensor

The principle behind indefinite permeability in antiferromagnets has been discussed in some detail in chapter 2. Here we summarize the basic principle.

In magnetic media, spins may be resonant at a certain frequency ω_0 as a response to an incident electromagnetic field. In the undamped limit $\Gamma = 0$, the condition $\mu_{xx} > 0$ and $\mu_{zz} < 0$ will be satisfied in the frequency interval $\omega_0 < \omega < \omega_s$. In the more realistic case where $\Gamma \neq 0$, μ_{zz} becomes complex, and we can in practice replace the negative refraction condition $\mu_{xx} > 0$ and $\mu_{zz} < 0$ by $\text{Re}(\mu_{xx}) > 0$ and $\text{Re}(\mu_{zz}) < 0$, which occurs over approximately the same frequency interval.

In Fig. 4.1 it is shown the real and imaginary parts of μ_{zz} , close to the magnon-polariton resonance frequency ω_0 , for MnF_2 at 4.2 K. We show the frequency scale in terms of the resonance frequency ω_0 . $\text{Re}(\mu_{zz})$ is seen to be negative in the frequency region between A and C , which are ω_0 and ω_s respectively. Since $\mu_{xx} = 1$, this region can be considered as an indefinite permeability region.

Since we are discussing effects related to propagation of waves, it is relevant to look at the $\text{Im}(\mu_{zz})$ shown in Fig. 4.1. The Imaginary part of the resonant permeability tensor of a material is directly related to the absorption inside the medium. In MnF_2 , $\text{Im}(\mu_{zz})$ is extremely small over almost the entire range, suggesting that, this medium would be an excellent candidate for transmission

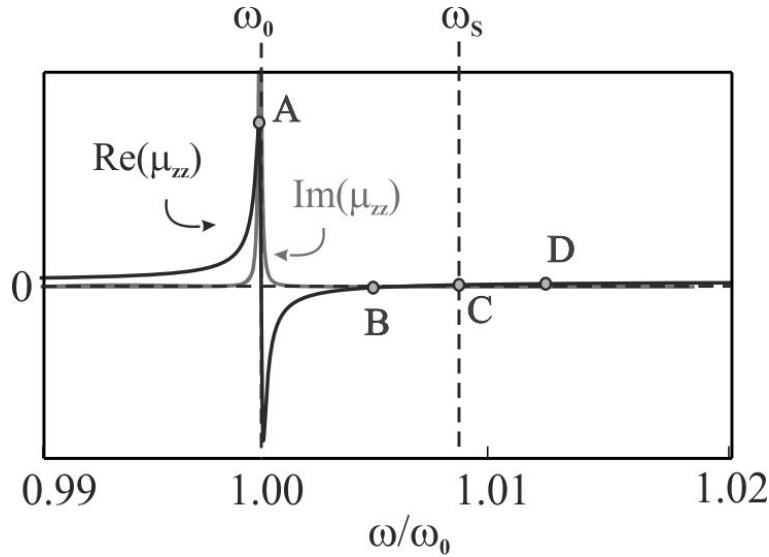


Figure 4.1: Real part of μ_{zz} for an MnF_2 single crystal as a function of frequency (expressed in terms of ω_0) around the magnon-polariton resonance frequency.

of electromagnetic radiation.

4.1.1 Hyperbolic dispersion

Hyperbolic media derive their name from the topology of their isofrequency curves, which are calculated from the dispersion relation between the frequency ω and the wave vector \mathbf{k} . In order to analyse this behaviour we consider refraction of electromagnetic waves at an interface between vacuum and MnF_2 . If the angle of incidence is represented as θ_1 , the in-plane wave-vector component k_x is given by

$$k_x = \frac{\omega}{c} \sin \theta_1. \quad (4.1)$$

The z component of the incident wave vector from vacuum, is given by the linear relation:

$$k_x^2 + k_{z1}^2 = \frac{\omega^2}{c^2}. \quad (4.2)$$

We assume that the incident radiation, from vacuum, is transverse electric (TE) polarised (\mathbf{E} along y) with $k_y = 0$.

Within the antiferromagnet, the permeability is a tensor $\overset{\leftrightarrow}{\mu}(\omega)$ with frequency dependent components in the form shown by Equation (2.5). In this case, waves with

transverse electric (TE) polarisation have a behaviour described by a dispersion relation in the form

$$\frac{k_{zz}^2}{\mu_{xx}} + \frac{k_x^2}{\mu_{zz}} = \frac{\omega^2}{c^2} \epsilon. \quad (4.3)$$

Examples of isofrequency curves, which relate the principal components of the wave vector, are shown in Fig. 4.2 for the different frequencies marked as A, B, C and D on Fig. 4.2. The group velocity, and hence the Poynting vector, are perpendicular to the constant ω plots, and are shown in Fig. 4.2 as red arrows.

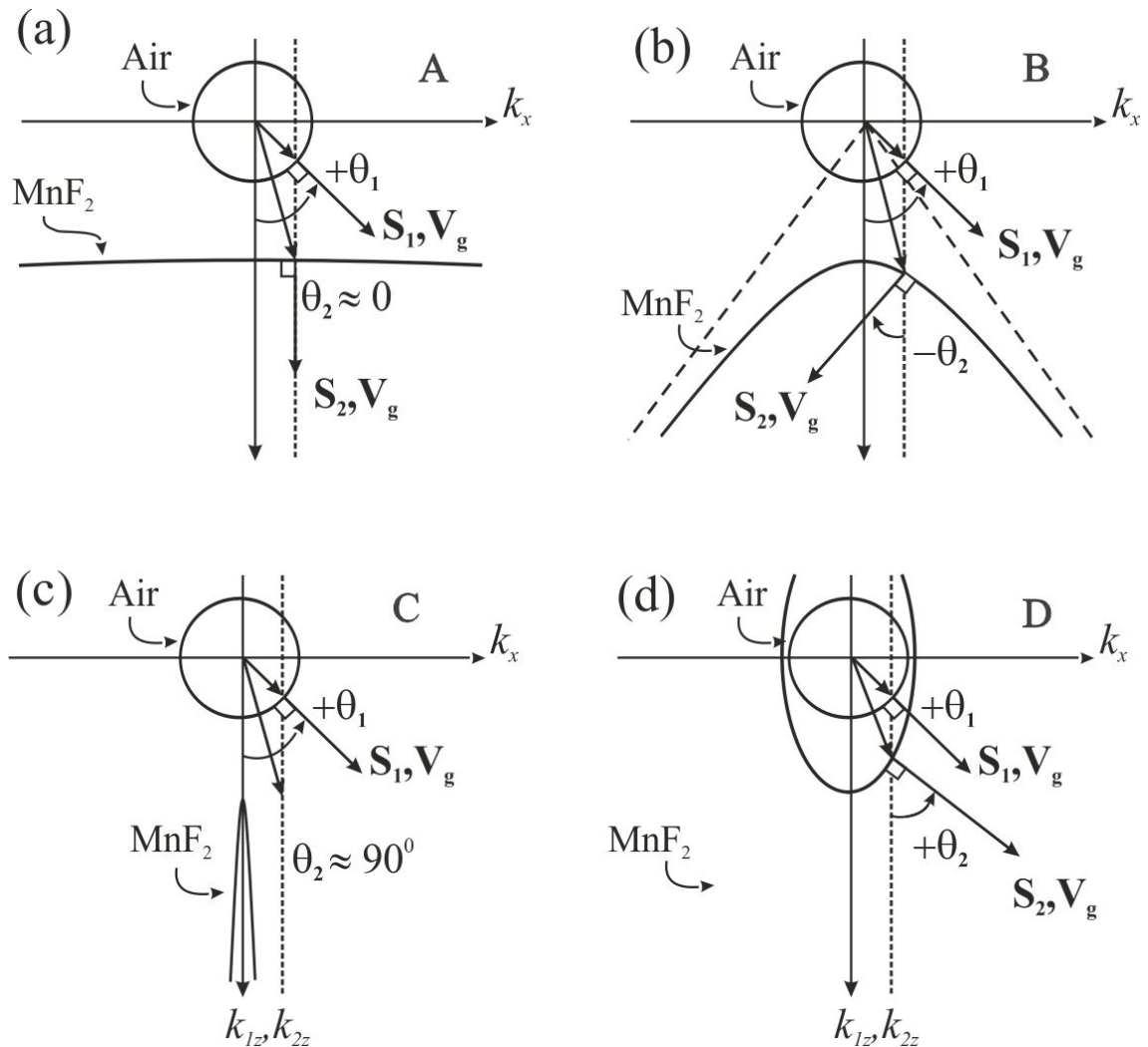


Figure 4.2: Real parts of the wave-vector component k_{1z} (air) and k_{2z} (MnF_2) as a function of k_x for transmission in a MnF_2 crystal having its extraordinary axis directed along x . (a) Frequency A ($\omega/\omega_0 = 1.00$), (b) frequency B ($\omega/\omega_0 = 1.004$), (c) frequency C ($\omega/\omega_0 = 1.006$) and (c) frequency D ($\omega/\omega_0 = 1.008 = \omega_s$)

In air (curves shown in Fig. 4.2) the linear dispersion and isotropic behaviour of propagating waves implies a circular isofrequency curve and it is given by

Equation (4.2). The direction of the incident beam (\mathbf{S}_1) is always perpendicular to the circular surface regardless of the incident beam's frequency. The circular isofrequency curve of air distorts to two branched straight lines at the magnon-polariton resonance frequency ω_0 , as shown in Fig. 4.2(a) at frequency A , where $\mu_{zz} \rightarrow \infty$ and Eq. 4.3 becomes independent of the of k_x , and hence the incident angle θ_1 . In this case, the x component of the Poynting vector (\mathbf{S}_2) approaches zero and the power flow propagation is perpendicular to the crystal's surface.

After the magnon-polariton resonance, in the frequency regime $\omega_0 < \omega < \omega_s$, such that $\mu_{xx} \cdot \mu_{zz} < 0$ the isofrequency curve opens into a hyperbola as seen in Fig. 4.2(b) at frequency B . Therefore, the x component of the Poynting vector (\mathbf{S}_2) inside the antiferromagnet is in the opposite direction to that of the incident beam (\mathbf{S}_1). That means negative refraction of the power flow may be achieved in antiferromagnetic crystals in the frequency regime $\omega_0 < \omega < \omega_s$. Such effect is called backwards refraction of rays, but no backward characteristics are exhibited by the wavevectors \mathbf{k} , and hence the directions of advance of the phase fronts.

At frequency C , close to ω_s i.e. the frequency where μ_{zz} vanishes, the two branches of the hyperbolas become very close as shown in Fig. 4.2(c). In this situation, the power flow (\mathbf{S}_2) makes an angle of approximately 90° with the normal, therefore the incident radiation propagates along the sample surface and there is no propagation into the crystal.

And finally, the behaviour seen in Fig. 4.2(d) at frequency D , is similar to an isotropic medium with positive ε and μ components, so that the circular isofrequency curve of air distorts to an ellipse. Here, the propagating power flow is positively refracted.

4.2 Power Flow Analysis

In order to analyse negative refraction of electromagnetic waves, it is important to look at the power flow \mathbf{S} , which, for the incident and refracted rays are represented as S_{1z} and S_{2z} respectively. In the first medium (vacuum), the power flow is parallel to the wave vector. In the second medium, however, that is not always true. In order to determine this direction, we represent the power flow by

the Poynting vector:

$$\mathbf{S} = \mathbf{E} \times \mathbf{H}^* \quad (4.4)$$

For TM polarised waves, the \mathbf{E} field is confined along y , so the Poynting vector is most easily represented in terms of the E_y field. Making use of the conversion $\mathbf{k} \times \mathbf{E} = \omega\mu_0\mu\mathbf{H}$, the resulting time-averaged Poynting vector $\langle S \rangle = 1/2\text{Re}(\mathbf{E} \times \mathbf{H}^*)$ inside the material has components

$$\langle S_{2x} \rangle = \frac{|E_y|^2}{2\omega\mu_0} \text{Re} \left(\frac{k_x}{\mu_{zz}} \right), \quad (4.5)$$

$$\langle S_{2y} \rangle = 0, \quad (4.6)$$

$$\langle S_{2z} \rangle = \frac{|E_y|^2}{2\omega\mu_0} \text{Re} \left(\frac{k_{2z}}{\mu_{xx}} \right) \quad (4.7)$$

In this configuration the power flow direction (or angle of refraction θ_2) can be calculating by geometry and is given by

$$\tan \theta_2 = \frac{\langle S_{2x} \rangle}{\langle S_{2z} \rangle} = \frac{\text{Re}(k_x / \mu_{zz})}{\text{Re}(k_{2z} / \mu_{xx})} \quad (4.8)$$

The power flow behaviour demonstrated in Fig. 4.2 can be confirmed by calculating the angle of refraction. In Fig. 4.3 we show the angle of refraction, calculated using Eq. 4.8, and confirms that θ_2 is equal to 0 and 90° at frequencies A and C respectively, positive at frequency D and negative at frequency B . We show calculations for different incident angles.

Figure 4.4 shows the resulting intensities for a Gaussian beam obliquely incident on an MnF_2 crystal, at the frequencies marked as A , B , C , and D on Fig. 5.1. At frequency A , corresponding to the magnon-polariton resonance frequency ω_0 , propagation into the antiferromagnet is essentially normal to the surface, as expected from Figs. 4.2(a) and 4.3. Frequency B is in the negatively refracting frequency range, and Fig. 4.4(b) confirms this behaviour. At frequency C , close to the zero in $\text{Re}(\mu_{zz})$, the power flow should be nearly parallel to the surface, but, in practice, it is seen that there is very high absorption so there is no effective

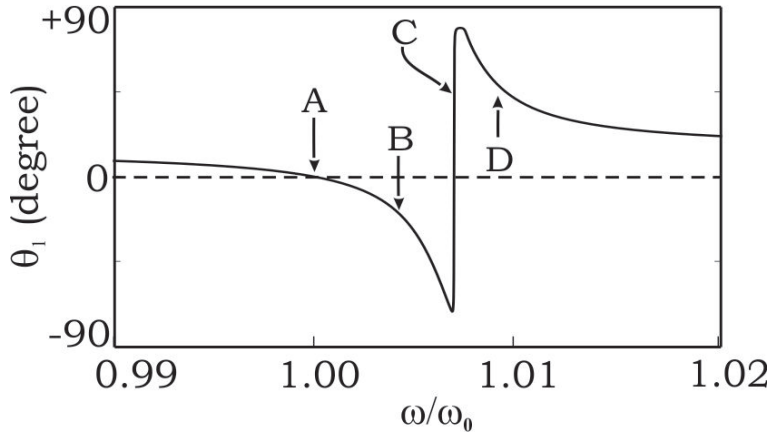


Figure 4.3: Angle of refraction θ_2 in MnF_2 for various angles of incidence from vacuum.

propagation. Positive refraction is observed at frequency D .

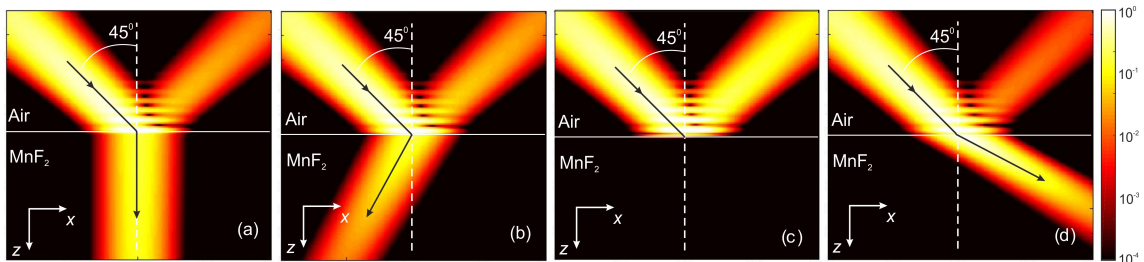


Figure 4.4: Contour plots showing intensities (in terms of the magnitude of the time-averaged Poynting vector) for a beam obliquely incident from vacuum on an MnF_2 crystal ($\theta_1 = 40^\circ$). (a) Frequency A ($\omega/\omega_0 = 1.00$), (b) frequency B ($\omega/\omega_0 = 1.004$), (c) frequency C ($\omega/\omega_0 = 1.006$) and (d) frequency D ($\omega/\omega_0 = 1.008 = \omega_s$).

All the plots in Fig. 4.4, except that corresponding to frequency C , show propagation into the antiferromagnet with extremely low absorption.

It is important to point out that the type of negative refraction shown in Fig. 4.4 differs from that seen in metamaterial and described by Veselago [8]. In such structures \mathbf{S} and \mathbf{k} travel in opposite directions whereas in the present case both always propagate in the forward direction. In metamaterials, the vector \mathbf{k} is in the direction of the phase velocity and opposite to the group velocity which does not happen in antiferromagnets where the phase velocity behaves in a similar manner as that one seen in positive refractive isotropic media. Thus, in antiferromagnetic crystals the group velocity of incident beam undergoes negative refraction, while the phase velocity undergoes positive refraction.

4.3 Effects of externally applied fields

One of the most exciting features of using indefinite permeability to obtain hyperbolic dispersion, and hence negative refraction, is that the permeability itself can be easily tuned by the application of an external magnetic field \mathbf{B}_0 , as discussed in Chapter 2 and shown in Fig 4.5. Considering an externally applied field perpendicular to the plane of incidence, along y , the immediate effect of such a field would be to cant the spins toward the field direction. As discussed previously, the main effect of canting is to raise the z -polarised resonance frequency ω_0 to a higher value ω_r . The external field also induces nonzero off-diagonal components in the permeability tensor given by Eq. 2.24.

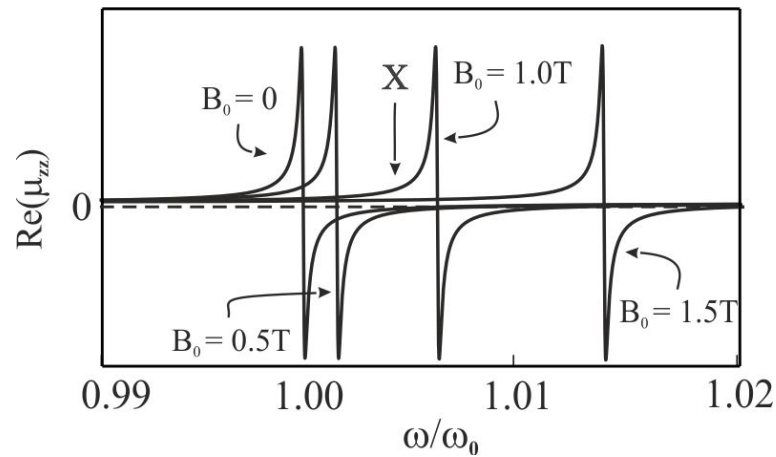


Figure 4.5: Effect of various external applied fields \mathbf{B}_0 on the real part of μ_{zz} for an MnF_2 single crystal as a function of frequency (expressed in terms of ω_0) around the magnon-polariton resonance frequency.

In this case, the dispersion relation equation has to be modified in order to include the off-diagonal permeability tensor components μ_{xz} , and it is now given by:

$$k_{zz}^2 \mu_{zz} + k_x^2 \mu_{xx} = \frac{\omega^2}{c^2} \varepsilon (\mu_{xx} \mu_{zz} + \mu_{xz}^2). \quad (4.9)$$

Examples of isofrequency curves, which relate the principal components of the wavevector at a chosen frequency (C), are shown in Fig. 4.6 for different values of externally applied field. The shape of the isofrequency plot gradually changes from a hyperbolic shaped curve to elliptical, which can be translated as the negatively refracted beam changing into positively refracted.

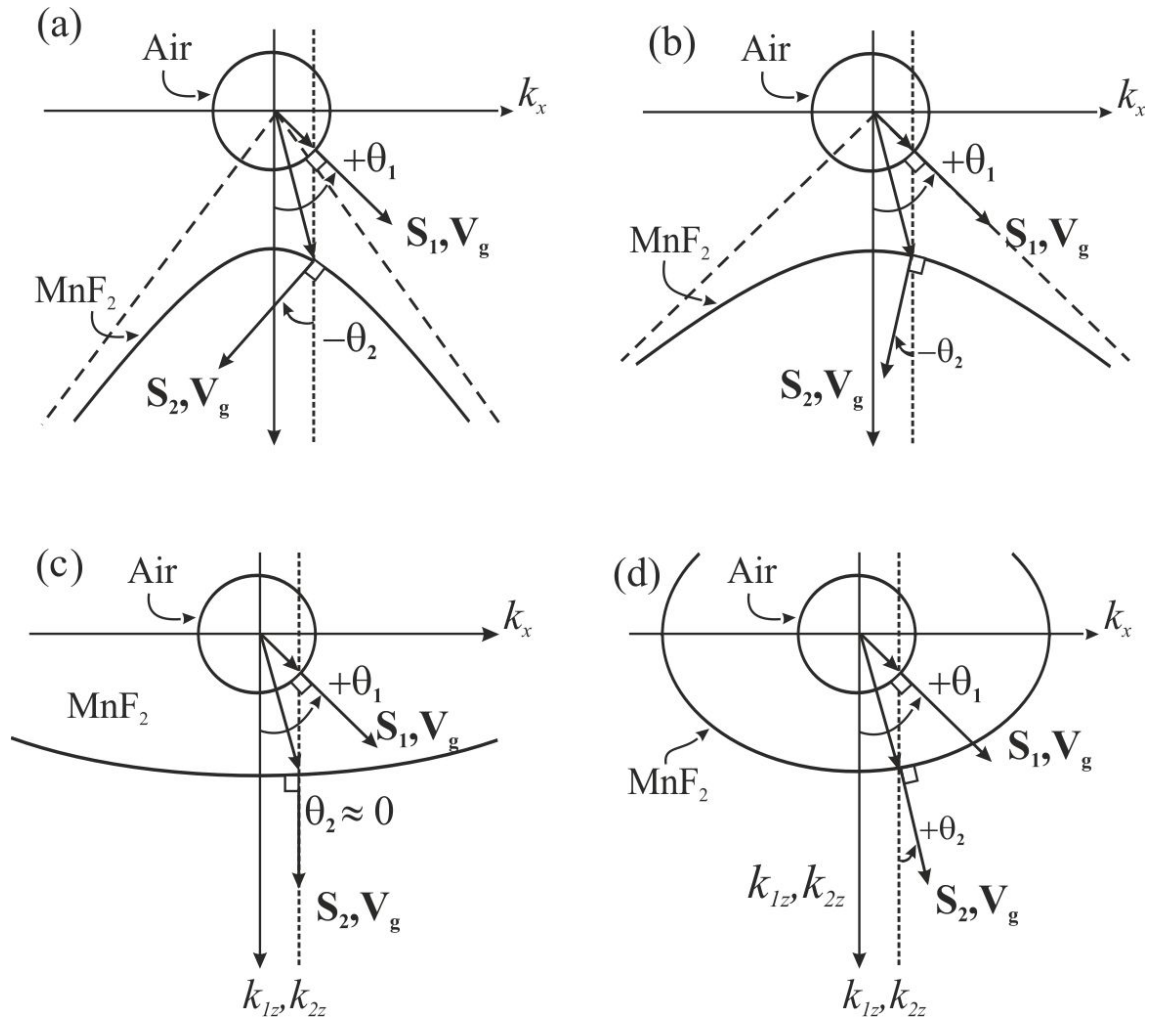


Figure 4.6: Real parts of the wave-vector component k_{1z} (red lines) and k_{2z} (blue lines) as a function of k_x for transmission in a MnF_2 crystal having its extraordinary axis directed along x , at a frequency $\omega/\omega_0 = 1.004$ for (a) $B_0 = 0.0$, (b) $B_0 = 0.5$ T, (c) $B_0 = 1.0$ T and (d) $B_0 = 1.5$ T.

In order to analyze the behaviour of the power flow when an external field is applied Eq. 4.8 should therefore be modified. In this situation the Poynting vector components will be changed to

$$\langle S_{2x} \rangle = \frac{|E_y|^2}{2\omega\mu_0} \text{Re} \left(\frac{k_x \mu_{xx} - k_{2z} \mu_{xz}}{\mu_{xx} \mu_{zz} + \mu_{xz}^2} \right), \quad (4.10)$$

$$\langle S_{2y} \rangle = 0, \quad (4.11)$$

$$\langle S_{2z} \rangle = \frac{|E_y|^2}{2\omega\mu_0} \text{Re} \left(\frac{k_{2z} \mu_{zz} + k_x \mu_{xz}}{\mu_{xx} \mu_{zz} + \mu_{xz}^2} \right) \quad (4.12)$$

The angle of refraction can still be calculated using the geometrical relation given by Eq. 4.8. Even though the angle is affected by the new off-diagonal components, the basic effect on the angle of refraction is to shift the features to higher frequency. The resulting values, assuming an incident angle of $\theta_1 = 40^\circ$, are shown in Fig. 4.7 for a series of both positive and negative applied fields (positive fields being directed along $+y$ and negative fields along $-y$).

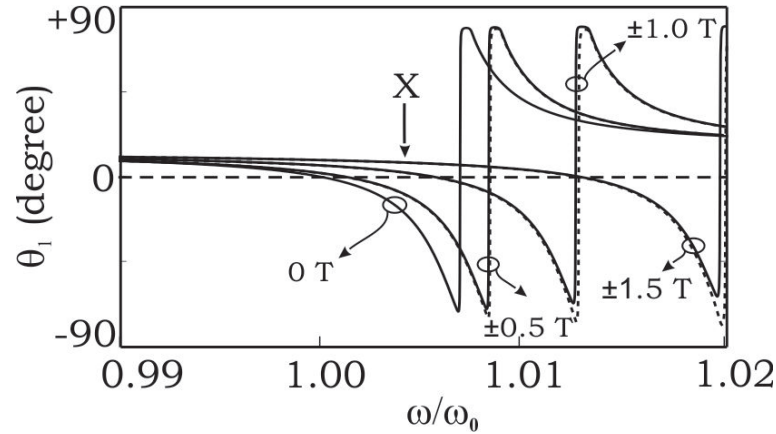


Figure 4.7: Angle of refraction θ_2 as a function of frequency in MnF_2 for an incident angle of $\theta_1 = 45^\circ$.

We now look at how the angle of refraction can be tuned by varying the applied magnetic field. Since the θ_2 curves in Fig. 4.7 depend on \mathbf{B}_0 , at any given frequency the angle of refraction will depend on the magnitude of the applied field. We consider the frequency marked as X ($\omega/\omega_0 = 1.004$) in Fig. 4.7. As can be seen from the figure, at this frequency the angle of refraction should vary from negative to positive as the applied field is increased, confirming the behaviour predicted by the isofrequency curves shown in Fig. 4.6.

We can verify the predicted behavior by studying that of a Gaussian beam incident on the surface of the antiferromagnet for various values of applied field, using the same type of analysis used in obtaining Fig. 4.4. The results for various positive values of \mathbf{B}_0 are shown in Fig. 4.8 (results for negative \mathbf{B}_0 are essentially the same, as expected from Fig. 4.7). Figure 4.8 confirms that the angle of refraction can be tuned from negative to positive using an applied external magnetic field, and that, in the case of the chosen frequency C, propagation into the antiferromagnet occurs without significant absorption.

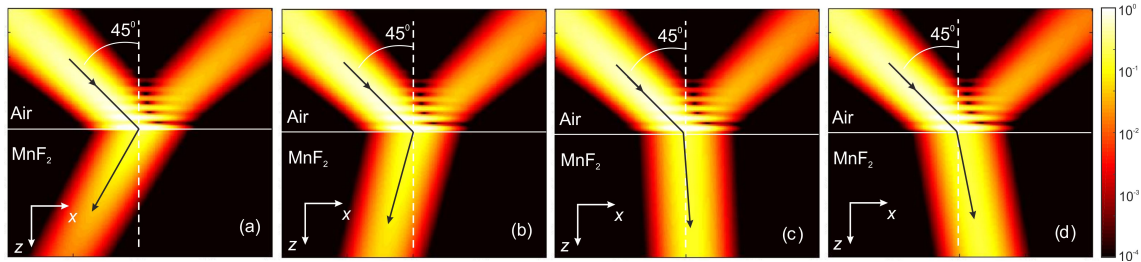


Figure 4.8: Intensity profile (time averaged power density) of a Gaussian beam obliquely incident at an angle of $\theta_1 = 45^\circ$, passing through an MnF_2 slab at frequency $\omega/\omega_0 = 1.004$ for (a) $B_0 = 0.0$, (b) $B_0 = 0.5$ T, (c) $B_0 = 1.0$ T and (d) $B_0 = 1.5$ T.

4.4 Snell's Law and Negative Refraction

Snell's law, which describes quantitatively the bending of a wave as it enters a medium, is perhaps one of the oldest and most well known of electromagnetic phenomena [75]. Snell's law is one of the basis for direct measurement of a medium's index of refraction n .

The phenomenon of refraction, happens at a boundary between two media due to the change in the speed of the travelling wave as it crosses from one medium to the other. This can be related by

$$n_1 \sin \theta_1 = n_2 \sin \theta_2, \quad (4.13)$$

where n_1 and n_2 represent the index of refraction in vacuum and within the medium respectively, $n = c/v$ and v is the speed of the travelling wave. This is the Law of Refraction, also known as Snell's Law¹. From this principle it has been shown that rather than going straight through, the ray entering a higher-index medium bends toward the normal. The reverse is also true; that is, on entering a medium having a lower index, the ray will bend away from the normal.

However, only recently, the implications of a negative n have been discussed. The real implications of this, have been studied by Pendry [32] who showed that such medium could focus all rays at the same point in the center of the slab, with no

¹Willebrord Snel van Royen was a Dutch astronomer and mathematician. In 1613 he became a professor of mathematics at the University of Leiden and in he rediscovered the law of refraction in 1621.

aberration if

$$\theta_1 = -\theta_2. \quad (4.14)$$

This is possible in the special case when $n_2 = -1$ and $n_1 = 1$.

4.4.1 Effective index of refraction in Antiferromagnets

We have explored in Section 4.1.1 the behaviour of the angle of refraction in antiferromagnetic crystals due to its hyperbolic dispersion. It is, therefore, useful to compare results with Snell's law.

In order to calculate the angle of refraction θ_2 within the antiferromagnetic slab, we use the same approach as proposed in the previous sections, which is based on the power flow direction \mathbf{S}_2 . In Fig. 4.9(a) we show both values of θ_2 in MnF_2 , calculated using Eq. 4.8 (blue solid lines) and for a metamaterial with $n = -1$ using Eq. (4.14).

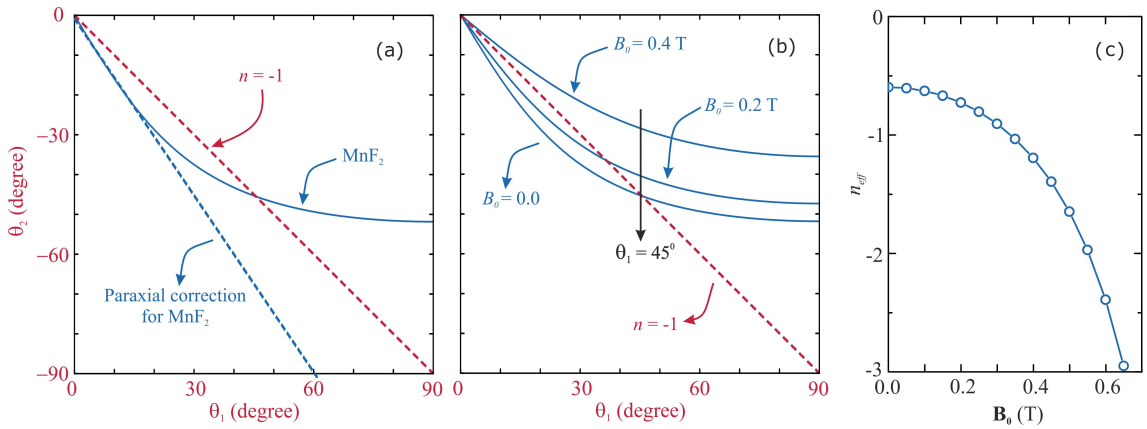


Figure 4.9: Angle of refraction θ_2 as a function of angle of incidence θ_1 . The red dashed line shows the behaviour of a medium with $n = -1$. (a) The solid line shows the angle of refraction calculated using Eq. 4.8 and the blue dashed line gives the result of using a paraxial approximation represented by Eq. 4.16 at the interface between air and a MnF_2 in the absence of an external field. (b) Effect of various external fields \mathbf{B}_0 on θ_2 in MnF_2 .

In an anisotropic medium such as antiferromagnets, the relationship between θ_1 and θ_2 can be found by combining Eqs. (4.1), (4.9), (4.10) and (4.12) with Snell's Law given by Eq. (4.14). In the absence of absorption this gives

$$\sin^2 \theta_2 = \frac{\mu_{xx} \sin^2 \theta_1}{\mu_{xx} \sin^2 \theta_1 (\mu_{xx} - \mu_{zz}^2) + \varepsilon \mu_{zz} (\mu_{xx} \mu_{zz} + \mu_{xz}^2)} \quad (4.15)$$

There is therefore not, in general, a linear relationship between θ_1 and θ_2 as would be expected for isotropic media. Nevertheless, in the small angle (paraxial) limit, we can take the sines of the two angles to be in the small angle limit ($k_x \ll \omega/c$) so that Eq. (4.15) reduces to

$$\frac{\sin^2 \theta_2}{\sin^2 \theta_1} = \frac{\mu_{xx}}{\varepsilon \mu_{zz} (\mu_{xx} \mu_{zz} + \mu_{xz}^2)} \quad (4.16)$$

The resulting curve for MnF_2 using Eq. (4.16) is shown as blue dashed lines in Fig. 4.9(a). Despite the large discrepancies at high angles when compared to the result of Eq. (4.8) (solid blue line), the paraxial approximation holds good at incident angles of 20° or less.

In Fig. 4.9(b), we show the effect of small externally applied fields so that all-angle negative refraction still possible at the chosen frequency $\omega/\omega_0 = 1.005$, however, the module of the angle is somewhat smaller.

The changes in the angle may be described by the the medium's index of refraction which can be found from Eq. (4.16), which gives the effective index n_{eff} for the antiferromagnet,

$$n_{eff} = \frac{\sqrt{\varepsilon \mu_{zz} (\mu_{xx} \mu_{zz} + \mu_{xz}^2)}}{\mu_{xx}}. \quad (4.17)$$

The resulting value of n_{eff} is show in Fig. 4.9(c) at the frequency frequency $\omega/\omega_0 = 1.005$. We can also see how the effective index of refraction increases in module as μ_{zz} become smaller in magnitude.

4.5 Figure of Merit

The degree of absorption in indefinite (hyperbolic) media is most often represented by a figure of merit (FOM) [76, 77] defined as $\text{FOM} = |\text{Re}(k_{2z})| / \text{Im}(k_{2z})$. Note that, according to this definition, the FOM is dependent on incident angle [15]. The FOM is plotted in Fig. 4.10 as a function of frequency for various magnetic fields \mathbf{B}_0 . Firstly we look at the case where $B_0 = 0$, the minimum in the FOM is slightly above frequency C , in a narrow frequency region which, in the absence of damping, would correspond to $0 < \mu_{zz} < (1/\varepsilon) \sin^2 \theta$, with k_{2z} imaginary and no propagation into the antiferromagnet. In the absence of damp-

ing, therefore, the FOM would be zero within this narrow frequency range, and infinite outside it (i.e., in the propagating regions). In the propagating regions, a finite FOM implies absorption. In the case of MnF_2 , the FOM is large at all frequencies except those close to frequency C , in line with the results of Fig. 4.3 which shows $\theta_2 = 90^\circ$. Of particular interest is that, in the negatively refracting region, the FOM is several orders of magnitude higher than typically reported for metamaterial structures, so propagating efficiency is high.

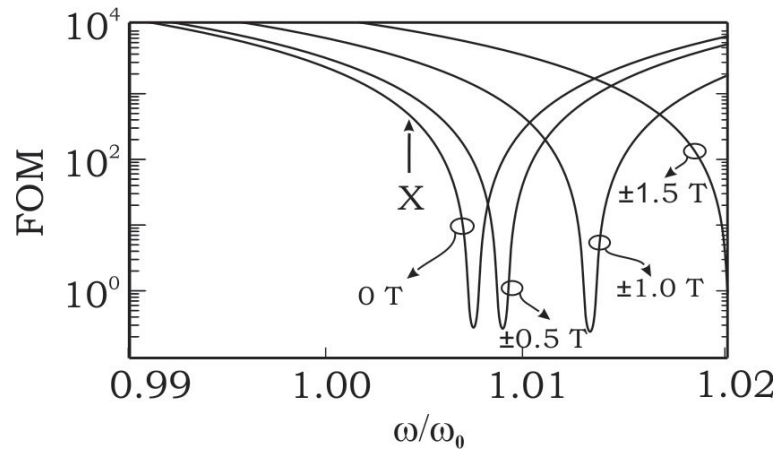


Figure 4.10: Figure of merite (FOM) as a function of applied field B_0 . Frequency X (8.98 cm^{-1}).

The effect of an external magnetic field \mathbf{B}_0 on the curves is effectively to shift its features to higher frequencies by the application of an external field, but are otherwise unchanged to any significant degrees of magnitude, despite the increased complexity that might be expected from the new features that appear in μ_{xx} and μ_{xz} . Thus the refracting behaviour is very similar to that discussed before for $B_0 = 0$, and, in addition, the application of an applied field does not adversely affect the FOM to any noticeable extent.

4.6 Nonreciprocity

In analyzing the effect of reversing the direction of \mathbf{B}_0 [in effect, changing the sign of μ_{xz} , and hence μ_{zx}], we note that, in the limit of zero damping (i.e., zero absorption), μ_{xx} and μ_{zz} would both be real and μ_{xz} would be imaginary. As in the zero field case, k_{2z} would be either wholly real or wholly imaginary, being real if there were propagation within the antiferromagnet and imaginary where

there is not (corresponding to a narrow frequency region just above the zero in μ_{zz}). In the former case, which is that of interest when considering refraction, it is straightforward to see from Eqs. 4.7 that none of the Poynting vector components would depend on the sign of μ_{xz} . The angle of refraction θ_2 would therefore be independent of the sign of \mathbf{B}_0 , and we would say that it is reciprocal with respect to field reversal. In practice, therefore, any nonreciprocal effects in the power flow direction are associated with the imaginary part of k_{2z} . At frequencies at which propagation is expected, the imaginary part is due to absorption.

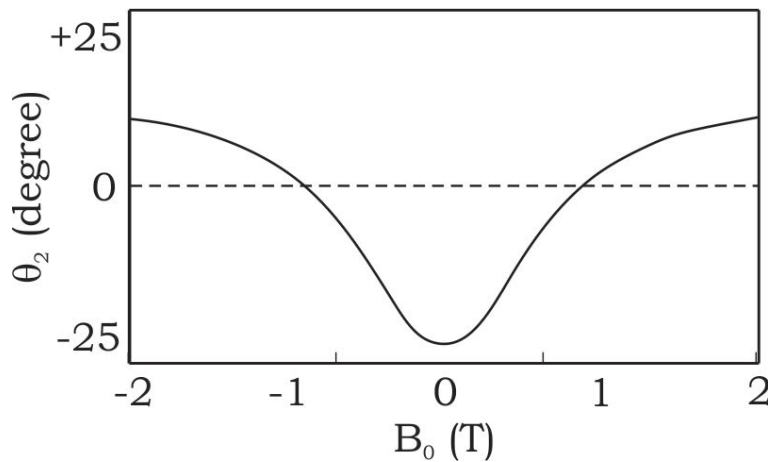


Figure 4.11: Angle of refraction θ_2 in MnF_2 as a function of applied field B_0 at frequency X (8.98 cm^{-1}).

The above analysis is in agreement with the results in Fig. 4.7. For most of the spectrum, reversing the sign of \mathbf{B}_0 has negligible effect. However, near the relevant minimum in the FOM (close to the zero in μ_{zz}), at which there is a significant imaginary contribution to k_{2z} , some nonreciprocity is seen. Nevertheless, the behavior at such frequencies is similar to that shown in Fig. 3(b), and it is not realistic to speak of refraction in the normal sense. In the regions in which it makes sense to discuss refraction, positive or negative, it is reasonable to say that refraction is reciprocal. Any nonreciprocal behavior present is simply due to absorption. This is similar to the type of nonreciprocity observed in the intensity of the reflected beam. Nonreciprocity in this intensity also only exists in the presence of absorption. We can see from Fig. 4.11 that the behaviour of the angle of refraction for both positive and negative fields is of reciprocal nature.

4.7 Conclusion

Negative refraction of this kind has been experimentally demonstrated in several systems varying from artificial structures to natural media [41, 42], mostly dielectric media. In magnetic structures, however, this phenomenon has been demonstrated in ferrites [78]. Such a hyperbolic material works in microwave ranges, and it can be tuned to sub-THz range by applying proper bias magnetic field. Here the frequencies studied are at higher frequencies due to antiferromagnetic resonance being in the THz region. Other materials are also potential candidates for experimental studies. For example, one can extend such properties to far infrared ranges by using CoF_2 , NiF_2 , KNiF_3 and FeF_2 [78].

In this chapter, it was shown that a uniaxial antiferromagnet should act as a negatively refracting medium due to its indefinite permeability. We have demonstrated how natural magnetic crystals can act as hyperbolic media and the implications of this phenomenon upon the transmitted beam. Furthermore, the refracting angle can be tuned by the application of an external magnetic field perpendicular the easy axis (which leads to spin canting). In this particular material, losses are expected to be very low due to the temperature in which the material become antiferromagnetic (bellow T_N), and the refracted beam should propagate with high efficiency.

Tunable Focusing

5.1 Hyperbolic dispersion	68
5.1.1 Refraction of a Gaussian Beam through an Antiferromagnetic Slab	69
5.2 Image formation in the paraxial limit	71
5.3 Caustics and field tunable focusing	74
5.4 Conclusions	76

The phenomenon of refraction is responsible for devices that can focus or (and) shape radiation, such as lenses [2]. Negative refraction, therefore, opens up new possibilities for optical imaging [32]. This intriguing phenomenon has attracted great attention, specially in terms of possibilities to construct lenses made from planar slabs, which are able to bring light rays to a focus, without physical curvature [32][79]. The most well-known example of such lens associated with negative refraction is that discussed by Veselago [8], who theoretically investigated the properties of an isotropic medium with $\epsilon < 0$ and $\mu < 0$. Such focusing is possible because the index of refraction is given by $n = \sqrt{\epsilon\mu}$, which is negative in metamaterials [80].

Over the past decade, all-angle negative refracting behaviour has been demonstrated in highly anisotropic media, such as the one proposed in Chapter 4, which suggests that these type of media would be a suitable candidate for slab lensing in the same way as proposed by Veselago. Recent works on layered and nanowire structures report negative refraction of the power flow (which determines the ray direction). Negative refraction in such media is not isotropic, but it does

occur for all incident angles, and slab lenses made of such medium have been demonstrated [81]. At far infrared frequencies, the anisotropic dielectric response associated with optical phonons in certain crystals appears particularly promising in this respect. Recent transmission experiments using crystal quartz have yielded results pointing to all-angle negative refraction based on this property [41], suggesting that this material may be suitable for slab lenses and that subwavelength imaging may be possible in the correct configuration [42].

In Chapter 4, we have observed how all-angle negative refraction is not only possible but it can also be tuned in magnetic crystals by simply applying a large enough external field \mathbf{B}_0 . In this Chapter, we concentrate on the effects of small applied fields so that the angle of refraction is always negative at a given frequency, however, its value may be modified. Based on this principle we investigate transmission across an antiferromagnetic slab which may be used as a Veselago lens, very much in the same way as the one presented earlier in Fig. 1.4(c). Magnetic crystals, however, not only focus radiation but also allow one to modify the focal length of the slab with an externally applied magnetic field. In addition, a rich caustic structure emerges at low temperatures, when damping should be small. These materials also produce slab focusing at higher temperatures, although the caustic structure disappears.

5.1 Hyperbolic dispersion

Before we proceed, it is useful for the following discussion, to be reminded of some familiar concepts. We start with the field dependent permeability tensor component μ_{zz} shown in Fig. 5.1.

The effect of an external field can be directly seen in the dispersion relation plots in Fig. 5.2. These relate the principal components of the wavevector at a given frequency and some examples can be seen in Fig. 5.2 and have been studied in details in Section 4, however, we now concentrate on the effect of small fields. The isofrequency surfaces can be used to explain the negative refraction behaviour in MnF_2 . Here we examine this behaviour in a single frequency, ($\omega/\omega_0 = 1.005$), where these plots are always hyperbolic even when small fields are externally

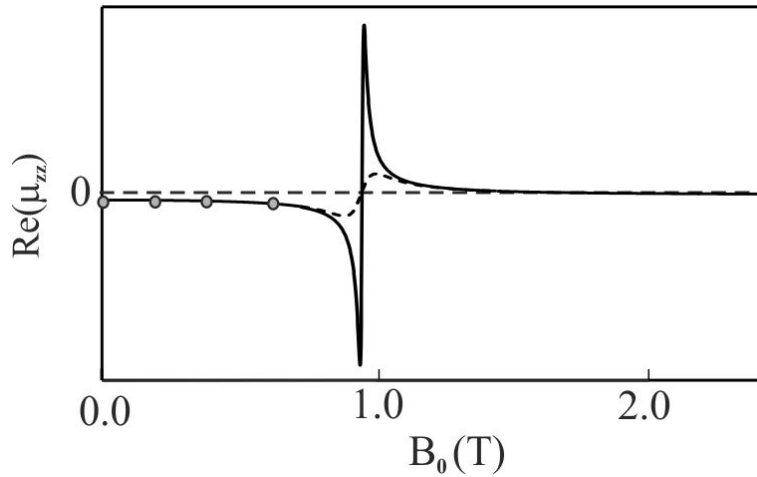


Figure 5.1: Real part of μ_{zz} for an MnF_2 single crystal as a function of an externally applied field \mathbf{B}_0 varying from 0.0 to 2.5 T.

applied.

The calculations are shown for different values of externally applied field. In air the linear dispersion displays isotropic behaviour of propagating waves, which implies a circular isofrequency curve given by Eq. 4.2. The circular isofrequency curve of air distorts to an ellipse for an anisotropic medium with positive ϵ and μ components. However, when we have extreme anisotropy, as occurs in MnF_2 close to the magnon-polariton resonance, such that $\mu_{xx} \cdot \mu_{zz} < 0$, the isofrequency curve opens into a hyperbola (shown as green lines in Fig. 5.2).

The group velocity, and hence the Poynting vector, is perpendicular to the constant ω plots, and are shown in Fig. 5.2 as red arrows. Therefore, the x component of the Poynting vector (\mathbf{S}_2) inside the antiferromagnet is always in the opposite direction to that of the incident beam (\mathbf{S}_1).

When a small external field \mathbf{B}_0 is applied the isofrequency curve becomes flatter than the equivalent zero field curve, as shown in Figs. 5.2(b), 5.2(c) and 5.2(d). This is due to changes in the permeability tensor component μ_{zz} , which, for fields less than 1 T, is negative and field dependent, in line with Fig. 5.2(a).

5.1.1 Refraction of a Gaussian Beam through an Antiferromagnetic Slab

Negative refraction of a Gaussian beam at oblique incidence can be seen directly in In Fig. 5.3. We calculate refraction of a beam of finite width, with a Gaussian

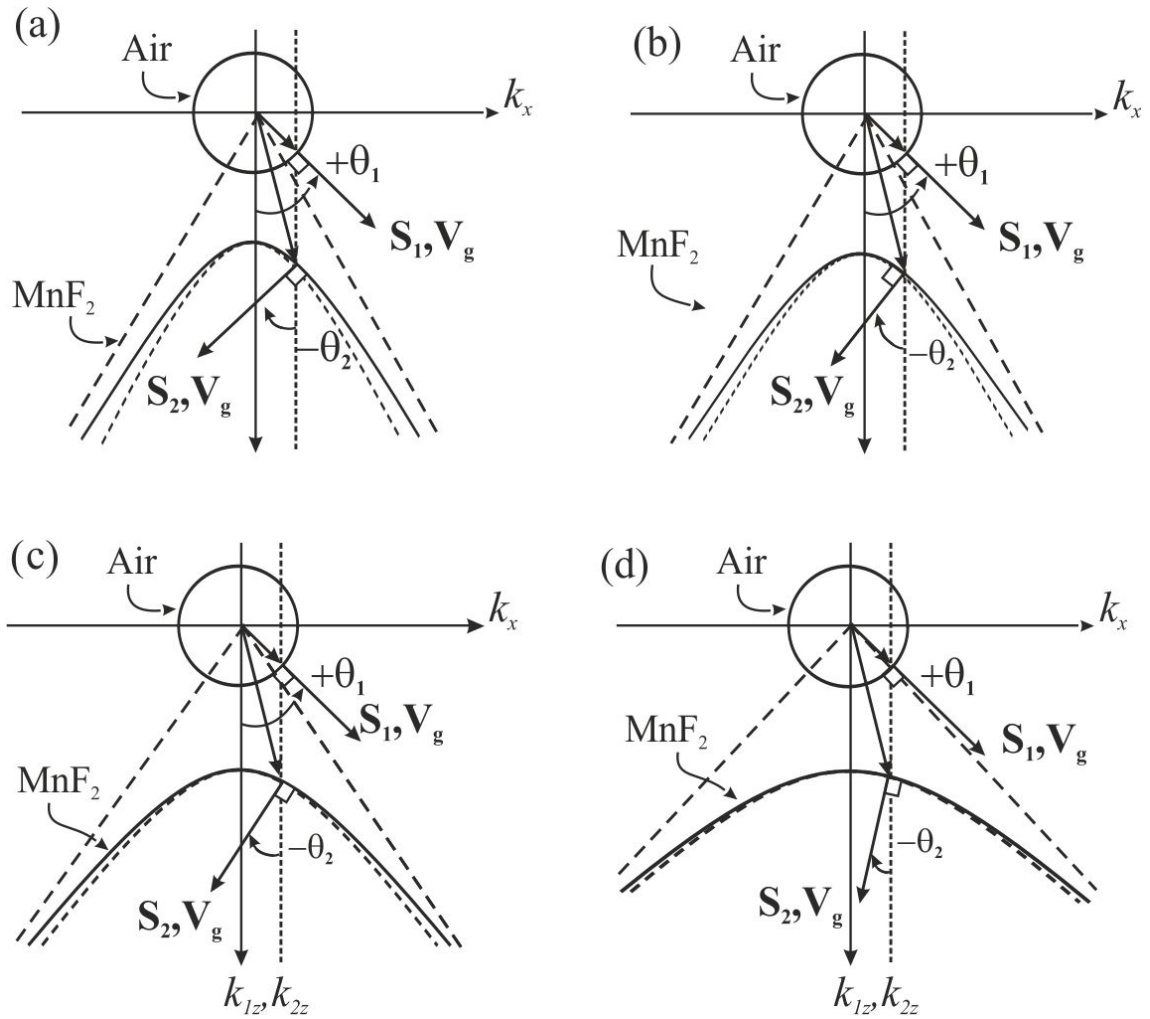


Figure 5.2: Real parts of the wave-vector component k_{1z} (blue lines) and k_{2z} (green lines) as a function of k_x (expressed in units of k_0), for transmission in a MnF_2 crystal having its extraordinary axis directed along x , in s-polarisation at a frequency $\omega/\omega_0 = 1.005$. (a) $B_0 = 0.0$, (b) $B_0 = 0.2$ T and (c) $B_0 = 0.4$ T. Dashed lines: $T = 0.06 T_N$. Solid lines: $T = 0.42 T_N$.

profile in x and z , passing through a MnF_2 crystal 10λ thick, where λ is the free-space wavelength. The angle of incidence is set to 45° (marked as a black arrow in Fig. 4.17(b)), and the Gaussian beam is focused at the slab surface.

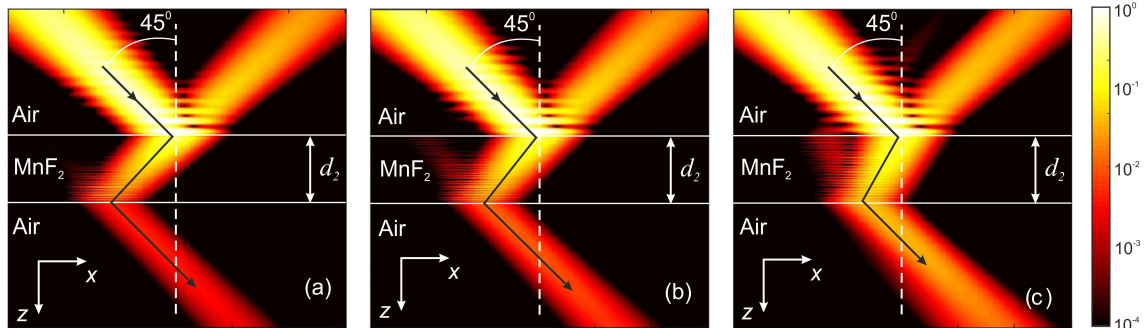


Figure 5.3: Intensity profile (time averaged power density) of a Gaussian beam obliquely incident at an angle of incidence $\theta_1 = 45^\circ$, passing through an MnF_2 slab at frequency $\omega/\omega_0 = 1.005$ where $\omega_0 = 8.67 \text{ cm}^{-1}$ ($T = 0.06 \text{ T}_N$). (a) $B_0 = 0.0$, (b) $B_0 = 0.2 \text{ T}$ and (c) $B_0 = 0.4 \text{ T}$. The intensity scale is in arbitrary units.

We show how the angle of refraction θ_2 can be tuned using an external magnetic field due to its effect on the permeability tensor components. For $B_0 = 0.0$ at $\omega/\omega_0 = 1.005$, negative refraction is seen as a displacement of the transmitted beam in the negative x direction (see Fig 5.3(a)). Note that the behaviour for all \mathbf{B}_0 values in the chosen range, is qualitatively similar. The direction of the refracted beam is consistent with the arrows shown in Fig. 5.2, which are perpendicular to the hyperbolic equifrequency plots. However the angle of refraction becomes smaller as the field is increased. The direction of the power flow (black arrows) could equally well be calculated using the power flow analysis described in E.

5.2 Image formation in the paraxial limit

Now we turn to the image formation by an antiferromagnetic slab lens. We start by considering the simplest situation, in which the paraxia approximation holds true. We consider the geometry depicted in Fig. 5.4(a), showing the ray path of a single ray emanating from a source S positioned at $x = z = 0$. The ray is negatively refracted in at the $z = d_1$ interface, and crosses the z axis at a distance L from the interface, within the slab. The ray is once again negatively refracted at the other side of the slab, crossing the z axis at a distance d_3 .

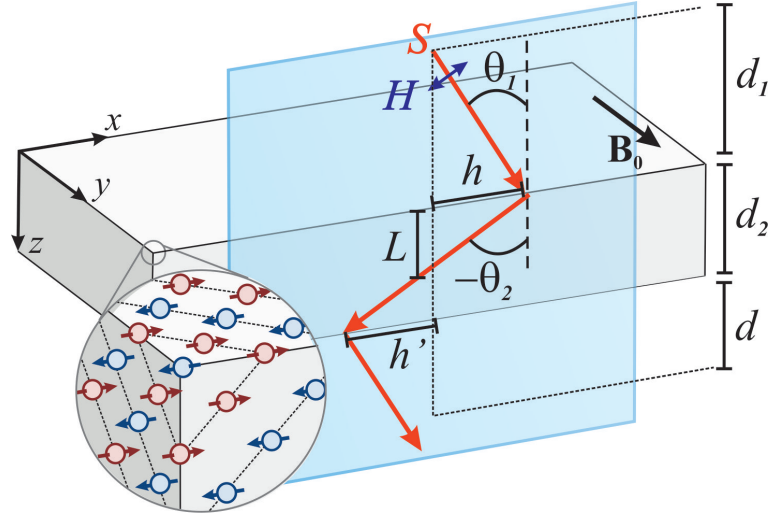


Figure 5.4: Path of a single ray from a source S passing through a slab of thickness d_2 .

As a result of negative refraction of this type, if a point source, emanating radiation in all directions, is placed close to an antiferromagnetic flat lens with parallel sides it is possible to obtain focusing within the lens, with a second focus on the other side of it. Thus an object placed on one side of the lens can form an image on the other side in a manner similar to that described by Pendry [32] for media with $\epsilon < 0$ and $\mu < 0$. In the paraxial limit i.e. small angles of incidence, focusing, i.e. image formation, effectively occurs at a single focal point as seen from Fig. 5.5(a).

Therefore, the lens equation for this type of system simply relates the image distance d to the object distance d_1 , the thickness d_2 of the lens and its effective index of refraction n_{eff} for use in Snell's law. It can be obtained either by geometric optics [31] or wave optics [82]. From the geometry shown in Fig. 5.4 one we can obtain the following relation at the first interface,

$$n_{eff} = \frac{\theta_1}{\theta_2} = \frac{h/d_1}{-h/L} = -\frac{L}{d_1}. \quad (5.1)$$

In a similar manner we can obtain at the second interface

$$n_{eff} = \frac{h'/d}{-h'/(d_2 - L)} = -\frac{d_2 - L}{d}. \quad (5.2)$$

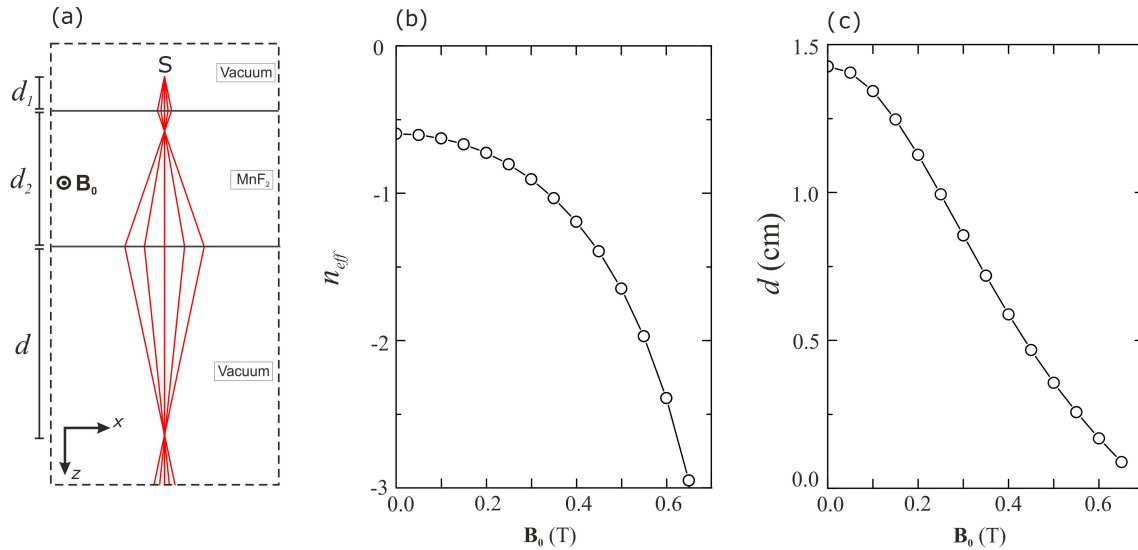


Figure 5.5: (a) Schematic of focusing due to a source S placed above an MnF_2 slab in the absence of an external field ($B_0 = 0.0$). The incident angle is restricted to the range -10^0 to $+10^0$. The distance d_1 is equal to 0.25 cm and d_2 is equal to 1.0 cm. The extraordinary axis is directed along x and incident radiation at $\omega/\omega_0 = 1.005$. Effect of an externally applied magnetic field \mathbf{B}_0 are shown for (b) the effective index of refraction n_{eff} and (c) the image distance d .

Eliminating L from both equation we get

$$d = -d_1 - \frac{d_2}{n_{eff}}. \quad (5.3)$$

The form of these equations are equivalent to those shown for lenses made of nonmagnetic hyperbolic media [31]. However, an exciting feature of magnetic crystals is the fact that n_{eff} strongly depends on μ_{zz} , whose value is highly reliant on external applied fields, as seen from Fig. 2.5(b). One consequence of a nonzero field is that the image position can be tuned as the angle of refraction depends on the effective index of refraction. The effects of a field \mathbf{B}_0 on the distance d between the image and the lens is illustrated in Fig. 5.5(c), which shows d decreasing as the strength of the field \mathbf{B}_0 increases. It is also worth mentioning another consequence of an externally applied field: the off-diagonal components in the permeability tensor become non-zero (i.e. gyromagnetic), and these off-diagonal components also affect n_{eff} , [49] although in practice the effect is negligible.

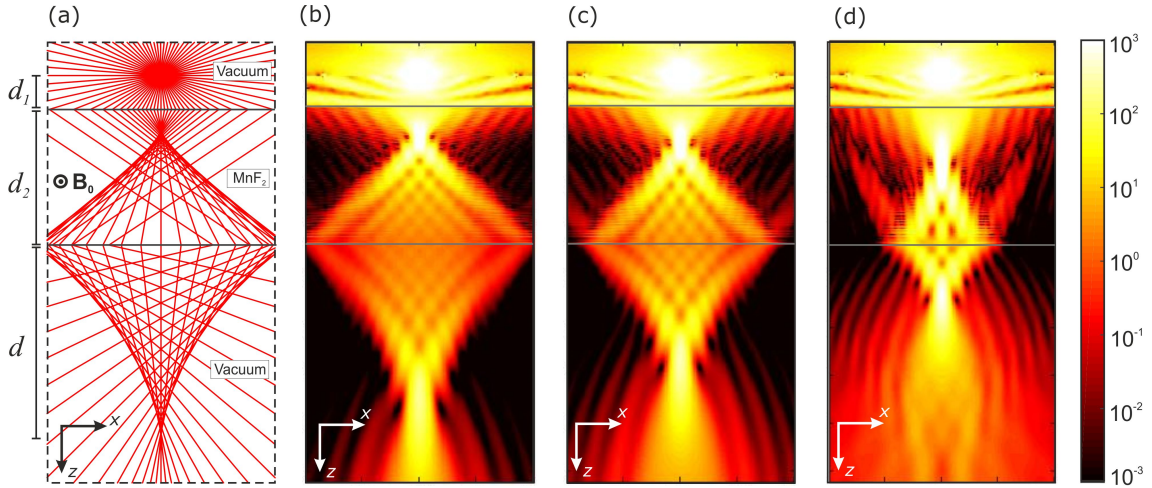


Figure 5.6: s-polarisation image formation at $T = 0.06 T_N$ due to a line source placed above an MnF_2 slab. The distance d_2 is $20\lambda'$ (≈ 1.0 cm), where λ' represents the wavelength within the antiferromagnet at normal incidence (about half the free-space wavelength). The distance d_1 is equal to $d_2/4$ (≈ 0.25 cm). The extraordinary axis is directed along x and the frequency of the incident radiation is $\omega/\omega_0 = 1.005$. (a) Schematic showing the path of multiple rays passing through an MnF_2 slab for $B_0 = 0.0$. (b) Power flow intensity for the setup shown in (a). Effect of a magnetic field on the intensity profile for (c) $B_0 = 0.2$ T and (d) $B_0 = 0.4$ T. The intensity scale is in arbitrary units. The intensity scale is in arbitrary units.

5.3 Caustics and field tunable focusing

Although the image formed by an antiferromagnetic lens is real, it is not perfect. In a hyperbolic medium the focusing of peripheral rays occurs at positions which cannot be described by the paraxial approximation. In order to illustrate this, we show, in Fig. 5.6(a), a ray diagram representing focusing over a wide range of incident angles. Marginal rays are focused after the paraxial focus within the slab, and before the paraxial focus outside the slab. This leads to an envelope of interfering refracted rays, i.e., caustics.

In Fig. 5.6(b) we show how the behaviour of the power flow, given by the time-average Poynting vector $\langle \mathbf{S}_2 \rangle$ of radiation emanating from the line source, directed along y , at a frequency $\omega/\omega_0 = 1.005$ and temperature $0.06 T_N$, in the absence of an externally applied field. Due to high levels of transmission for all incident angles, intersecting rays produces a network of constructive and destructive interference within the caustic envelope, both inside and outside the slab. This is most visible when damping is extremely low (as would be expected at low temperatures for good crystals). The network of intensities discussed here are

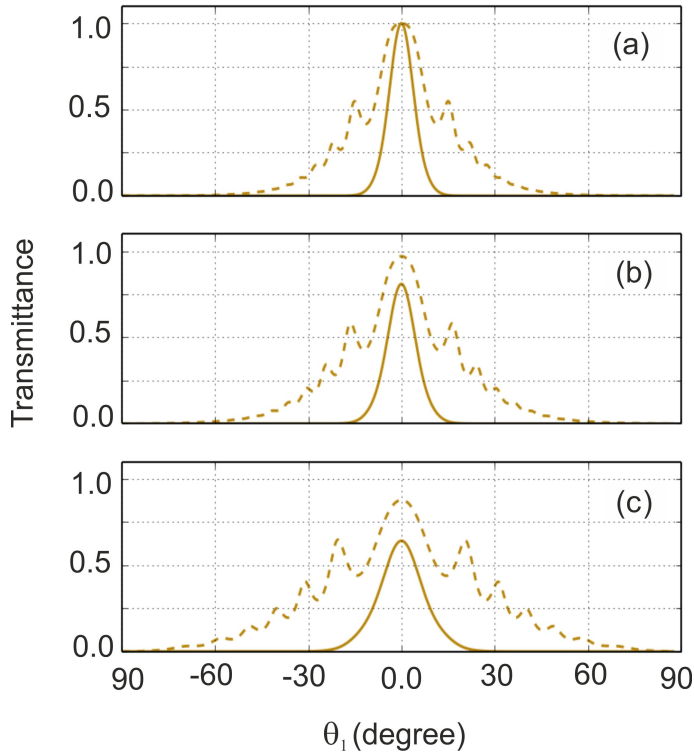


Figure 5.7: Calculation of transmittance as a function of incidence angle (θ_1) for an MnF_2 slab of thickness $d_2 = 20\lambda'$ (≈ 1.0 cm) whose easy axes lies along x . The incident radiation, at a frequency $\omega/\omega_0 = 1.005$, is s-polarised. (a) $B_0 = 0.0$, (b) $B_0 = 0.2$ T and (c) $B_0 = 0.4$ T. Dashed lines: $T = 0.06 T_N$. Solid lines: $T = 0.42 T_N$.

examples of caustic curves analogous to those discussed in the classic works by Nye [83]. These caustics are a result of the non-perfect focusing due to hyperbolic behaviour of antiferromagnets. The shape of these caustics can be modified by changing the magnitude of the external applied field \mathbf{B}_0 . Nevertheless, despite the complications of the caustics due to imperfect focusing at high angles, there is a high intensity sharp focus at the cusp. Figures 5.6(c) and 5.6(d) show how the image is moved closer to the lens by simply applying an external field, as predicted by Fig. 5.5(c).

As well as investigating image formation at $0.06T_N$, we have also considered higher temperatures an example is shown for $0.42T_N$, leading to a significant increase in magnon damping within the antiferromagnet. The effect of this is to reduce transmission at higher angles, as shown in Fig. 5.7, which compares the angular dependence of transmittance at the two temperatures. The figure shows that, at the higher temperature, efficient transmission only occurs within the range $\pm 20^\circ$. This behaviour can affect the properties of a lens made of

an antiferromagnet, the result of which can be seen in the sketch in Fig. 5.8(a) which shows exclusively the focusing of small angle incident rays, leading to paraxial-type behaviour.

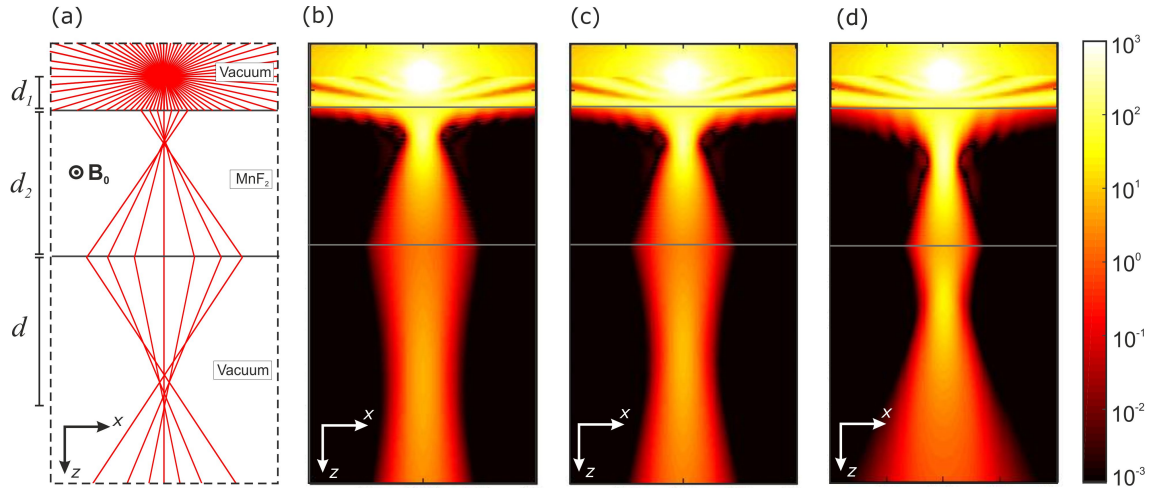


Figure 5.8: s-polarisation image formation at $T = 0.42 T_N$ due to a line source placed above of an MnF_2 slab. The distance d_2 is $20\lambda'$ (≈ 1.0 cm) and d_1 is equal to $d_2/4$ (≈ 0.25 cm). The extraordinary axis is directed along x and incident radiation at $\omega/\omega_0 = 1.005$. (a) Schematic showing the path of multiple rays passing through an MnF_2 slab for $B_0 = 0.0$. (b) Power flow intensity for the setup shown in (a). Effect of a magnetic field on the intensity profile for (c) $B_0 = 0.2$ T and (d) $B_0 = 0.4$ T. The intensity scale is in arbitrary units.

Since, at high angles of incidence there is little propagation inside the slab, there is not much interference emanating from these rays with higher damping, and the envelope of refracted rays forming a well defined caustics fold is lost, as seen from the power flow behaviour shown in Fig. 5.8(b). However, the radiation focusing is still present as a strong cusp and the tunable image position is also unaffected by the temperature change although, due to the loss of high angular components the effect of the field is less obvious as seen in Figs. 5.8(c) and 5.8(d). Nevertheless, these components will be more prominent in the case of thinner slabs, leading to the restoration to of much of the structure shown in Fig. 5.6.

5.4 Conclusion

In this Chapter it was shown that antiferromagnetic crystals are strong candidates for slab lensing studies in the THz region (around the magnon-polariton frequencies). We concentrated our calculations to fairly thick slabs when compared to

those in most studies based on multilayer structures [37, 84]. Even though they are highly transparent, better transmission should be possible with thinner slabs (specially for the cases in which the temperature is increased).

Furthermore, the focusing achieved by these materials can be tuned by using an externally applied field \mathbf{B}_0 . Changing the focal point of a hyperbolic lens has been shown by Dumelow and co-workers when the frequency is changed and the value of the permeability tensor components change. However, changing the frequency of radiation in the THz region means changing the source, which is not always possible in experiments, therefore changing the focal point with an external field is a far simpler approach. In the same way, by changing the overall object-image distance one could be able to investigate embedded objects without knowing its real distance from the detector or source.

At low temperatures, when damping is low enough to enable transmission of all incident angles, a rich caustics structure can be seen. However the key element, focusing of radiation, can be obtained even if the temperature is increased. In both cases, the transmission levels still show more efficiency than those demonstrated in artificial hyperbolic multilayers due to fabrication issues [15]. It is also worth mentioning that the focusing achieved by our lenses, i.e., focusing inside and outside the lens, is different from spherical lenses as the radiation in conventional lenses is guided to a focus due to their shape.

This work clearly needs extending to other frequencies with other materials, and there appear to be various possibilities for experimental studies in either ferrimagnetic or ferromagnetic crystals [78].

Easy Axis Orientation Dependence

6.1 Easy axis transformation	80
6.2 Rotated Hyperbolic dispersion	81
6.3 Implications on the angle of refraction	82
6.4 Orientation dependence on focusing	85
6.5 Concluding Remarks	86

The concept of anisotropy in natural crystals has been of interest for some considerable time [85]. However, the understanding of hyperbolic media and how they are connected to the anisotropy of a medium is fairly new [3]. Up to now, the research on hyperbolic media has mostly been concentrated on geometries in which the direction of the anisotropy is polarised either parallel or perpendicular to propagation of electromagnetic waves [86, 37, 84, 87]. However, the anisotropy polarisation direction can be decisive when fully investigating optical effects in hyperbolic media. For instance, in non-magnetic media, if the anisotropy is not polarised along one of these direction, in general, there will appear nonzero off-diagonal components in the permeability tensor which are essentially real. Off-diagonal components of this type can often be brought in unintentionally in experimental works. However, even the small contribution of these kind of resonant component can lead to extremely increased absorption inside the crystal [39].

Some progress has been made using modest deviations of the anisotropy direction [88, 89, 90]. In such systems, there is no resonance associated with the anisotropy

which makes these systems particularly promising for transmission studies [91]. As there is no hyperbolic behaviour, all-angle negative refraction cannot be achieved, and hence slab lensing of the type shown in Chapter 5.

Throughout this work we have only considered the situation when the antiferromagnetic crystal's magnetisation direction lies parallel to the surface where radiation is incident. This chapter is dedicated to some preliminary results on the effect of easy axis rotations. If such rotations are allowed, the position where the image is formed can be modified not only along the z axis, similar to when an external magnetic field is applied, but in the present situation the image position can also change along the image plane.

6.1 Easy axis transformation

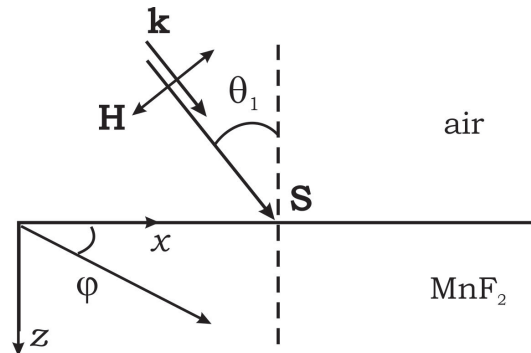


Figure 6.1: (a) Geometry of easy axis rotation along the xz plane by an angle φ .

We start by exploring the properties of magnetic polaritons in an antiferromagnetic crystal whose easy axis may be rotated in the xz plane by an angle φ such as shown in Fig. 6.1. For simplicity, we concentrate our analysis in the case when there are no externally applied fields. If a rotation takes place ($\varphi \neq 0$), the tensor shown in Eq. 2.12 has to be modified in terms of the rotation angle φ and it is now given by

$$\overset{\leftrightarrow}{\mu}'(\omega) = \begin{pmatrix} \mu'_{xx} & 0 & \mu'_{xz} \\ 0 & \mu'_{yy} & 0 \\ \mu'_{zx} & 0 & \mu'_{zz} \end{pmatrix} \quad (6.1)$$

Such tensor is obtained using $\overset{\leftrightarrow}{\mu}'(\omega) = \mathbf{T} \overset{\leftrightarrow}{\mu}(\omega) \mathbf{T}^{-1}$, where \mathbf{T} is a transformation matrix in the xz plane and \mathbf{T}^{-1} is its transposed. In the absence of an external field, $\mu_{xz} = \mu_{zx}$ by symmetry and the tensor components are

$$\mu'_{xx} = \mu_{xx} \cos^2 \varphi + \mu_{zz} \sin^2 \varphi \quad (6.1a)$$

$$\mu'_{zz} = \mu_{xx} \sin^2 \varphi + \mu_{zz} \cos^2 \varphi \quad (6.1b)$$

$$\mu'_{xz} = \mu'_{zx} = (\mu_{zz} - \mu_{xx}) \sin \varphi \cos \varphi. \quad (6.1c)$$

6.2 Rotated Hyperbolic dispersion

In order to analyse the properties of propagating waves in an antiferromagnetic crystal whose easy axis may be rotated along the xz plane, we proceed by combining Maxwell's equations once again, in the same way as done in Chapter 2. However, the permeability tensor has to be replaced by Eq. 6.1 and using Eqs. (2.25d) and (2.27) we obtain

$$\frac{1}{(\mu'_{xx}\mu'_{zz} - \mu'^2_{xz})} \left(\mu'_{zz} \frac{\partial^2}{\partial z^2} + \mu'_{xx} \frac{\partial^2}{\partial x^2} + \mu'_{xz} \frac{\partial^2}{\partial x \partial z} + \mu'_{zx} \frac{\partial^2}{\partial z \partial x} \right) E(x, y) = -\frac{\omega^2}{c^2} \varepsilon_{\parallel} E(x, y) \quad (6.2)$$

We take $E(x, y)$ as being given by Eq. (2.32) which yields

$$\mu'_{zz} k_{z2}^2 + 2\mu'_{xz} k_x k_{z2} + \mu'_{xx} k_x^2 = -\frac{\omega^2}{c^2} \varepsilon_{\parallel} (\mu'_{xx}\mu'_{zz} - \mu'^2_{xz}). \quad (6.3)$$

Note that when $\varphi \neq 0$ the off-diagonal components are equal ($\mu_{xz} = \mu_{zx}$), and differently from the case when $\mathbf{H}_0 = 0$, here these components are purely real when $\Gamma = 0$. And the result of same sign off-diagonal components is an extra term ($2\mu_{xz} i k_{\parallel} k_{z2}$) in the equation for dispersion relation

In previous chapters we have concentrated on the simple situation in which the crystal's easy axis lied parallel to both surface and incidence plane. This has also been the case for most studies in hyperbolic non-magnetic media. However, when an arbitrary direction ($0 < \varphi < 90^0$) is considered the propagation of rays

becomes more complex.

In Fig. 6.2 we show the effect of different rotations of the easy axis direction on the equifrequency plots. It is important to point out that all frequencies are now of interest in terms of exotic wave propagation properties, therefore, we show the effect of rotation on both hyperbolic and elliptical dispersion. At frequencies below ω_0 (here we used $\omega/\omega_0 = 0.995$), where all components of the permeability are positive, the elliptical dispersion rotates generating negative refraction for a small range of incident angles. In this case, propagation is allowed to all incident angles regardless of the rotation angle φ .

At frequencies between ω_{TO} and ω_{LO} the hyperbolic dispersion rotates in similar manner as the elliptical case [See Fig 6.2(b)]. However if the rotation angle is too high such as the one shown for 45° , the propagation of small angles of incidence disappears giving way to a broad “reststrahl” region, i.e., total reflection region similar to the one discussed in Chapter 3.

When the easy axis is rotated 90° so that it is along z , the hyperbolic isofrequency plots also rotates the same amount. In the region between ω_0 and ω_s , there is a forbidden band as the hyperbola branches now point to the direction perpendicular to the propagation.

6.3 Implications on the angle of refraction

In this section we restrict our analysis to small rotation angles of the crystal’s easy axis, since at high angles propagation is drastically affected by losses inside the material. These losses are induced by the off-diagonal components shown in Eq. 6.1, which are real and φ dependent, making k_{z2} complex even when no damping is included.

As mentioned before, the angle of refraction can also be calculated from geometry in terms of the power flow direction, and it is known to be

$$\tan \theta_2 = \frac{\langle S_{2x} \rangle}{\langle S_{2z} \rangle}, \quad (6.4)$$

where the components x and z of the power flow can be obtained from the resulting time-average Poynting vector $\langle \mathbf{S}_2 \rangle = 1/2 \text{Re}(\mathbf{E} \times \mathbf{H}^*)$. Using a similar

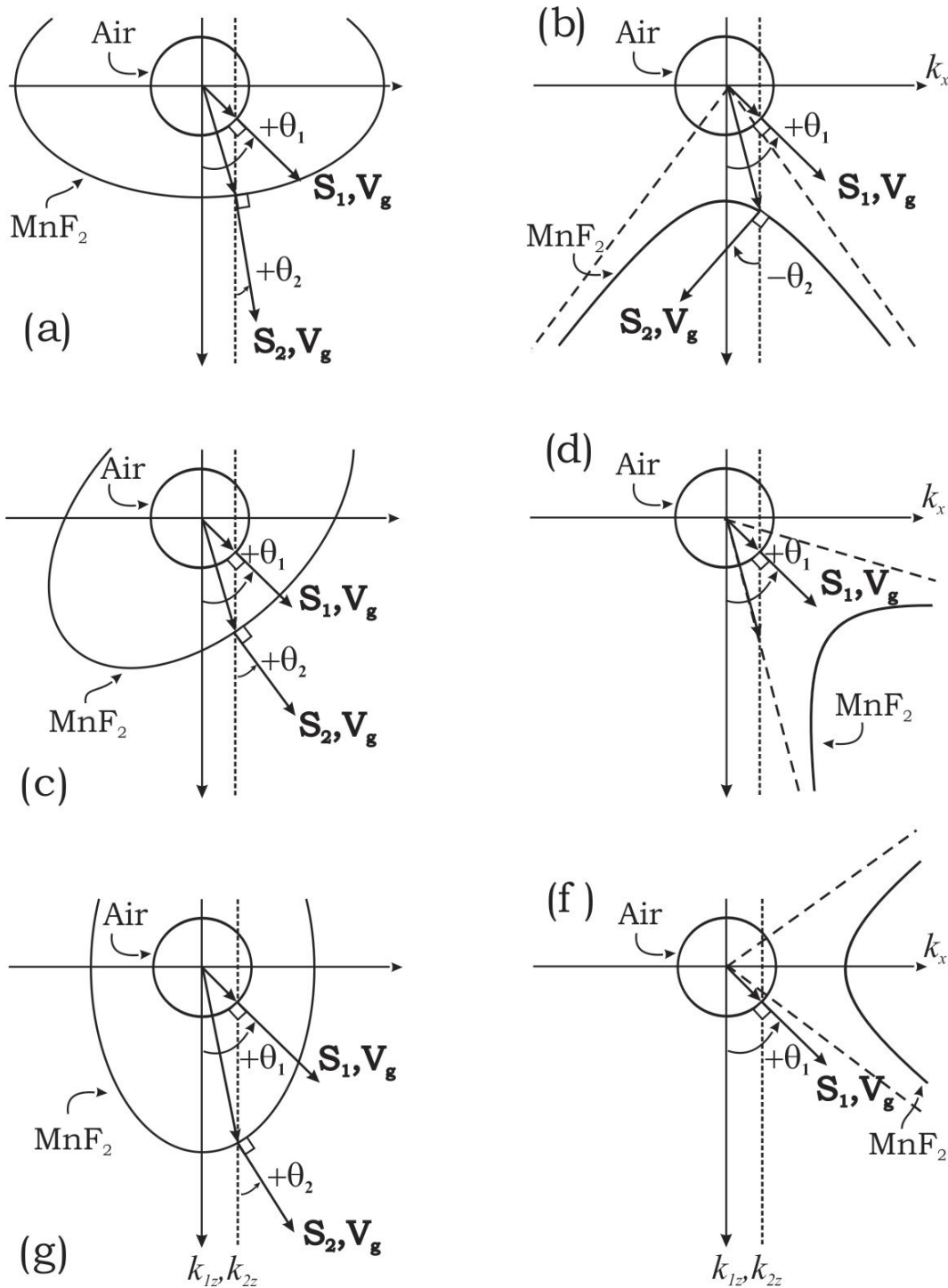


Figure 6.2: Real parts of the wave-vector component k_{1z} (air) and k_{2z} (MnF_2) as a function of k_x for transmission in a MnF_2 crystal having its extraordinary axis rotated along the xz plane by (a)-(b) $\varphi = 0$, (c)-(d) $\varphi = 45^\circ$ and (e)-(f) $\varphi = 90^\circ$. The curves on the left hand-side are for a frequency below ω_0 and at the right hand-side we see frequencies above ω_0 .

approach as the one shown in Appendix E, these components can be written as

$$\langle S_{2x} \rangle = \frac{|E_y|}{2\omega\mu_0} \text{Re} \left(\frac{k_x \mu'_{xx} + k_{2z} \mu'_{xz}}{\mu'_{xx} \mu'_{zz} - \mu'^2_{xz}} \right), \quad (6.5a)$$

and

$$\langle S_{2z} \rangle = \frac{|E_y|}{2\omega\mu_0} \text{Re} \left(\frac{k_z 2\mu'_{zz} + k_x \mu'_{xz}}{\mu'_{xx}\mu'_{zz} - \mu'^2_{xz}} \right). \quad (6.5b)$$

We have dealt with off-diagonal components of this form before in Chapter 4, however, the field induced components are imaginary which has little effect on the angle of refraction θ_2 . These components are also not equal when a non-zero field is considered and this yields different signs in Eq. 6.5 and 6.5b. Even though an external field is responsible for shifting the resonance frequency, the way the beam is negatively refracted at the new frequency region is unaffected. In the case when $\varphi = 0 \Rightarrow \mu_{xz} = 0$, that the angle of refraction depends strictly on μ_{xx} and μ_{zz} . Therefore, if $\mu_{xx} > 0$ and $\mu_{zz} < 0$, all-angle negative refraction is seen. However, if $\varphi \neq 0 \Rightarrow \mu_{xz} \neq 0$, the angle of refraction is not as straightforward, it now depends not only on μ_{xx} and μ_{zz} but also on the other resonant off-diagonal component μ_{xz} which are real. As seen from Eq. 6.4, in combination with Eqs. 6.5 and 6.5b, if $\varphi \neq 0$ the angle of refraction cannot be predicted by a simple combination of signs.

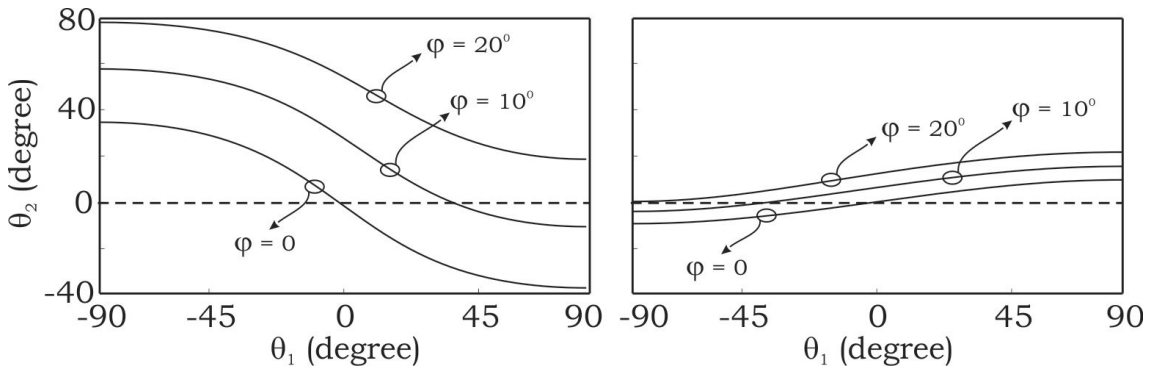


Figure 6.3: Effect of a nonzero rotation angle φ on the angle of refraction θ_2 and a function of the incident angle θ_1 at (a) $\omega < \omega_0$ (b) $\omega_0 < \omega < \omega_s$.

The effect of φ on the angle of refraction is shown in Fig. 6.3 for two different frequencies. At frequencies below ω_0 such as the example $\omega/\omega_0=0.995$ shown in Fig. 6.3(b) the angle of refraction always has the same sign as the incident angle. When the easy axis is rotated by 10° for a range of $-\theta_1$ negative refraction can be seen. If greater rotation is applied, $\varphi = 20^\circ$, for all values of $-\theta_1$ negative refraction is possible. In any rotated case no similar behaviour is possible for $+\theta_1$.

In the frequency regime $\omega_0 \leq \omega \leq \omega_s$, the effect of φ is show in Fig. 6.3(a). If

$\varphi = 0$ all-angle negative refraction can be seen as discussed in Chapter 4 and the same in magnitude so that $|\theta_2(+\theta_1)| = |\theta_2(-\theta_1)|$. However when $\varphi = 10^0$ this condition does not hold true so that $|\theta_2(+\theta_1)| \neq |\theta_2(-\theta_1)|$, and ultimately, when a greater angle of rotation is seen $\varphi = 20^0$ all angles of refraction are positive regardless of the sign of θ_1 .

6.4 Orientation dependence on focusing

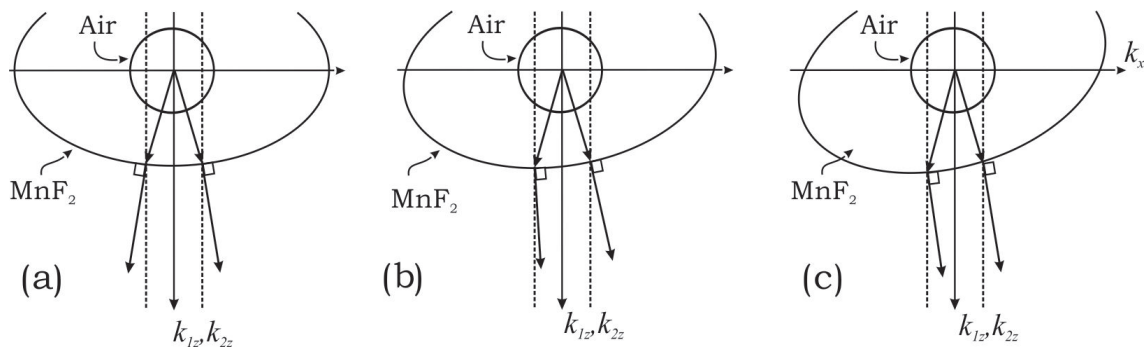


Figure 6.4: Real parts of the wave-vector component k_{1z} (air) and k_{2z} (MnF_2) as a function of k_x for transmission in a MnF_2 crystal at a frequency $\omega < \omega_0$ having its extraordinary axis rotated along the xz plane by (a) $\varphi = 0$, (b) $\varphi = 10^0$ and (c) $\varphi = 20^0$.

We now turn this analysis to the implications on the focusing by a slab lens made of an antiferromagnetic crystal. We start by analyzing the elliptical dispersion rotated by small angles as shown in Fig. 6.4. When $\varphi = 0$ the incident ray for positive and negative angles diverge from each other. When φ is nonzero, negative refraction is seen for $-\theta_1$. However, no focusing is possible as not all angles are negatively refracted, in fact, in a range between -90^0 and 90^0 all rays are channeled to the same side of the material. Therefore, this situation is not of interest for slab lensing.

For hyperbolic dispersion, focusing can be seen for $\varphi = 0$. When φ is nonzero, the hyperbolic dispersion rotates as shown in Fig. 6.5. The angles now have different magnitudes, so that there is a difference in the path lead by the different rays, which means focusing happens at a different position in both x and z axes. We now examine how focusing from a line source placed above an MnF_2 slab would work. If the crystal's easy axis lies along an arbitrary direction in the xz plane the propagation of waves can be considerably affected and at $\omega/\omega_0=1.04$

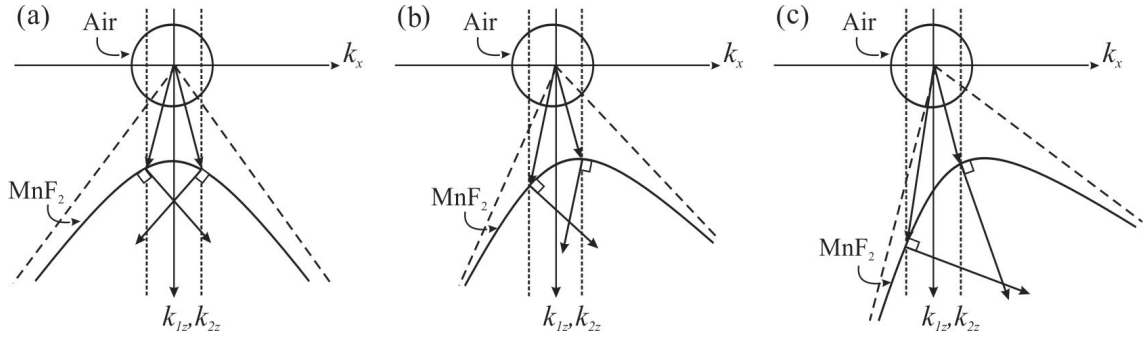


Figure 6.5: Real parts of the wave-vector component k_{1z} (air) and k_{2z} (MnF_2) as a function of k_x for transmission in a MnF_2 crystal at a frequency $\omega_0 < \omega < \omega_s$ having its extraordinary axis rotated along the xz plane by (a) $\varphi = 0$, (b) $\varphi = 10^\circ$ and (c) $\varphi = 20^\circ$.

the main effect of a rotation in the easy axes is to shift the position of the paraxial focus. Differently from magnetic media when external fields are applied, the position of the image changes along the optical axes as seen from Fig. 6.6(b).

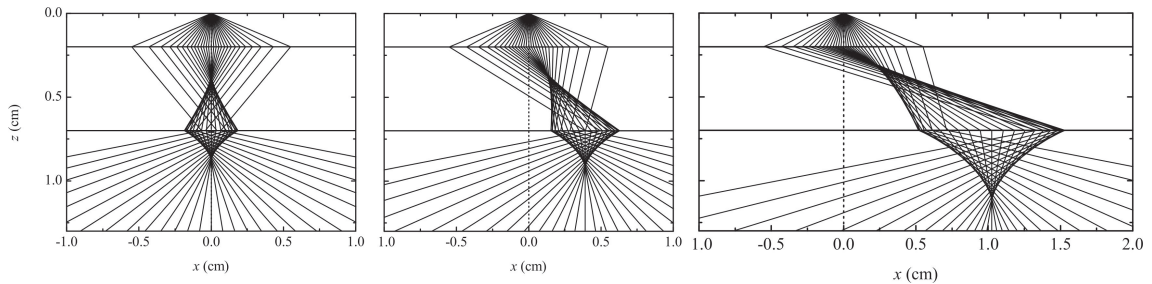


Figure 6.6: Schematic of Image formation due to a line source placed above of an MnF_2 slab at a frequency $\omega_0 < \omega < \omega_s$ having its extraordinary axis rotated along the xz plane by (a) $\varphi = 0$, (b) $\varphi = 10^\circ$ and (c) $\varphi = 20^\circ$.

If the angle of rotation φ suffer great rotation as seen from Fig. 6.6(c) the transmission is extremely affected and the focusing is not as evident any more, even though the power flow is channelled to one single side of the slab.

6.5 Concluding Remarks

Here, it was shown how focusing in hyperbolic media is extremely dependent on the crystal orientation. When crystal's axes are rotated along the xz plane the permittivity tensor, which is usually diagonal, is replaced by a new tensor with non-diagonal elements. For the simple case of anisotropy such as simple dielectric crystals the new off-diagonal components are symmetrical $\varepsilon_{xz} = \varepsilon_{zx}$ and essentially real.

We stress here that our results can be applied to any hyperbolic system, artificial or natural, magnetic or dielectric. However in more complicated case such as gyrotropic media, characterized by non-diagonal $\overleftrightarrow{\epsilon}(\omega)$ and (or) $\overleftrightarrow{\mu}(\omega)$ dyadics, no such simplification is generally possible. Gyrotropic effects are given by imaginary non-diagonal elements and after rotated they are non-symmetric. This means, not only rotation of the paraxial focus can be achieved but tunability is also possible when external fields are applied.

Such analysis may also be crucial when performing experiments using focusing in hyperbolic media since a slight rotation on the crystals axes may change dramatically the results expected.

Conclusions and Open Questions

7.1 Summary of this thesis	89
7.2 Outlook	91
7.2.1 Subwavelength Imaging	91
7.2.2 Depth Probe Possibilities	92
7.2.3 Other Systems to be Investigated	93

7.1 Summary of this thesis

The overarching theme of this thesis was an investigation of how novel optical effects in hyperbolic magnetic crystals are affected by externally applied magnetic fields. Particularly, it was investigated the situation where the external field lies perpendicular to the easy axis direction in antiferromagnetic crystals, inducing spin canting. Here, the main findings of this work are summarized.

In **Chapter 3**, it was shown how lateral displacements are possible on the surface of an antiferromagnetic crystal. Large reciprocal displacements can be seen close to the magnon-polariton frequency in the absence of an external field. This class of hyperbolic media are particularly interesting when an effects of an external field \mathbf{B}_0 are considered. For instance, as seen in Section 3.3, the appearance of off-diagonal components on the permeability tensor, and hence breaking in the crystal's time reversal symmetry induced by the spins canting towards the field direction, leads to nonreciprocal reflection. This nonreciprocity weigh up

on lateral displacements, making D change in magnitude, depending on the direction of \mathbf{B}_0 . Not only that, but the canting of spins also leads to Goos-Hänchen shifts even at normal incidence. Even though lateral displacements on the surface of natural crystals have been previously predicted [27], as discussed in Chapter 1, nonmagnetic media are not field reliant, and therefore, do not display nonreciprocal shifts.

In **chapter 4** it was presented a discussion of the implication of magnetic crystals working as hyperbolic media. Special attention was given to the effects on the angle of refraction, which becomes negative around these frequencies. Negative refraction of all angles was one of the first phenomena to be associated with hyperbolic dispersion in artificial structures [3], and recently, it has also been shown in natural crystals [41]. However, the vast majority of the studies have somewhat been limited to nonmagnetic structures. In this context, magnetic crystals such as antiferromagnets, open up a vast range of new possibilities. Differently from nonmagnetic systems, the angle of refraction in magnetic media can be tuned across different frequencies by just applying an external field.

Another important characteristic of this type-media is its transmission efficiency. The efficiency of negative refractive media is often described by the figure of merit (FOM), which in natural magnetic crystals such as MnF_2 is dramatically higher than artificial materials previously studied [15].

In **Chapter 5** it was shown the consequences of using a hyperbolic magnetic crystal as a slab lens as well as the effect of temperature changes on these systems. The key point here is that for hyperbolic magnetic media, not only can a caustic structure be seen, but focusing can also be achieved in a slab lens. Similar focusing has been reported in other natural hyperbolic media such as quartz crystals [42] and triglycine sulphate [31]. In both cases this occurs for TM-polarised radiation with a distinct image position that varies with frequency, due to the way that phonons couple with the electric part of the electromagnetic radiation. However, natural magnetic media are field reliant which allows tunable image formation at a single frequency without changing the crystal structure or the physical shape of the lens. The effects of temperature were also discussed. For low temperatures, and hence low damping, a rich caustic structure can be observed

inside and outside the lens. We believe that the method to obtain caustics which we have reported should be possible in any hyperbolic media given a low enough temperature. Whereas the caustics disappear when the temperature increases, the tunable focusing is still possible.

The effect of the easy axis orientation was discussed in **Chapter 6**. Even though such effects are usually unwanted when performing experiments, due to the induction of absorption. If a slight rotation of the easy axes takes place, the focusing through a slab lens can dramatically change. In such case the sign of the angle of refraction is not as straightforward as the situations previously studied, and can be said to be nonreciprocal $|\theta_2(+\theta_1)| = |\theta_2(-\theta_1)|$. It is also important to note that if there is rotation, negative refraction becomes possible at frequencies where the dispersion is elliptical.

Finally, we stress that the analysis and general principles presented in this thesis apply equally well to other types of hyperbolic media, both natural or artificial.

7.2 Outlook

The scope of the work presented in this Thesis is limited to MnF_2 crystals acting as a hyperbolic material which can be used to achieve novel tunable optical effects, therefore, a number of obvious extensions of this work can be foreseen. It is described below some directions in which preliminary work has been performed and further investigation are necessary.

7.2.1 Subwavelength Imaging

Slab lenses, such as the ones presented in Chapters 5 and 6, are not often linked to subwavelength imaging. These type of lenses are most often restricted to focusing in the far-field limit. However, slab lenses made of hyperbolic materials can be used to induce reproduction of near-field images [92].

We expect that our intriguing findings can benefit near-field and subwavelength imaging. Normally, for free space or isotropic media, k_z is real but when k_x becomes large, k_z becomes imaginary, i.e., the propagation of waves in the z direction is evanescent: it decays exponentially with z . However, in the case

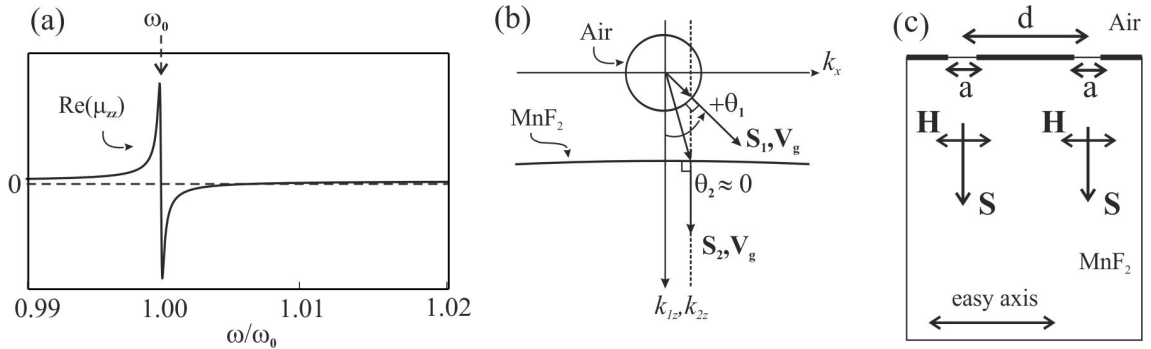


Figure 7.1: (a) Real part of the principal component of the permeability tensor of MnF_2 around the magnon-polariton frequency. (b) Real part of the wavevector component k_{2z} as a function of k_x (expressed in units of k_0), for transmission in an MnF_2 crystal having its easy axes directed along x , at the resonance frequency ω_0 ($\omega/\omega_0 = 1.00$). (c) Schematic showing the general setup of imaging due to a two-slit source at the surface of a slab of MnF_2 at frequency ω_0 .

of indefinite permeability such as the one shown in Fig. 7.1(a), at a frequency $\omega = \omega_0$, k_z is real for all k_x values, even for very large ones. Therefore what would normally be evanescent waves, now become propagating waves.[16, 42] In this case, the emitted evanescent waves of a light source placed near a slab, with arbitrarily large in-plane wave vectors can excite propagating modes in the slab, which will transfer the near-field information to the opposite interface of the slab, as shown experimentally in the analogous indefinite permittivity case based on the phonon polariton response in hexagonal boron nitride[93]. As the equifrequency curve is nearly flat (see Fig. 7.1(b)) at the magnon resonance frequency itself, all components should transmit across within the slab with the same phase and a faithful reproduction of subwavelength details of the object should be possible as shown in the sketch in Fig. 7.1(c).[42] The use of an external field should allow some fine tuning as the resonance frequency can be shifted when applying such a field.

7.2.2 Depth Probe Possibilities

In this work, we have concentrated on using an external magnetic field to adjust the image position for a fixed source position. However, the external field is effectively tuning the overall object-image distance. Thus, one could, in principle, consider a slightly different configuration in which a detector (or detector array) were placed at the surface of the slab (or a fixed distance from it). Assuming that

there were an illuminated object at a certain unknown distance from the other side of the slab, this distance could then be measured by scanning the applied magnetic field and determining the field at which the image became well focused on the detector. In this case, the lens would act as a type of depth probe, suitable for investigating embedded objects.

7.2.3 Other Systems to be Investigated

In this thesis only slab lenses made from MnF_2 , a material that shows particularly low magnon damping at low temperature, have been discussed. However, this material belongs to an important group of antiferromagnetic salts, such as FeF_2 and CoF_2 , which should also display similar behaviour at temperatures far enough below their Néel temperatures.[46] Antiferromagnets whose Néel temperatures fall above room temperature are hard to come by (although there are exceptions, such as nickel oxide), and, in addition, magnon damping is likely to severely limit transmission at higher temperatures. Nevertheless, alternative magnetic crystals, such as ferrites, display field-tunable hyperbolic dispersion, similar to that discussed here, associated with the ferromagnetic resonance.[78] Such materials may well be suitable for use as tunable slab lenses at room temperature in the same way as shown here for MnF_2 at low temperature.

Appendices

On the Reflectivity off a semi-infinite Antiferromagnet

For the interpretation of optical effects, such as Goos-Hänchen shifts, on the surface of antiferromagnetic crystals, formulas for the reflectivity and transmission are needed. To derive these equations we need to consider the dispersion relation, hence wave vector inside and outside the material, combined with the boundary conditions at the surface of the crystal.

For different geometries of the antiferromagnetic crystal, the reflectivity and transmission can be calculated as a function of the angle of incidence, however, one of the main determiners of these coefficients is the direction of polarisation. Here we summarize the main technique used to obtain the equation for transmission and reflection used throughout this thesis, we concentrate on the case when the incident wave is transverse electric (TE) polarized.

A.1 Boundary Conditions

Here we treat the geometry of a surface of an antiferromagnetic crystal whose x axis is aligned along the sublattice magnetisation directions. The incidence plane is xz and a magnetic field is applied perpendicular to both incidence plane and anisotropy direction (along y) as shown in Fig. A.1.

We now assume that the electric field of the propagating electromagnetic waves is polarised perpendicular to the incidence plane (TE) and along y . We consider that the radiation is incident from air with ϵ_1 and μ_1 . In the antiferromagnet, however, these quantities are frequency dependent and in the presence of an external field

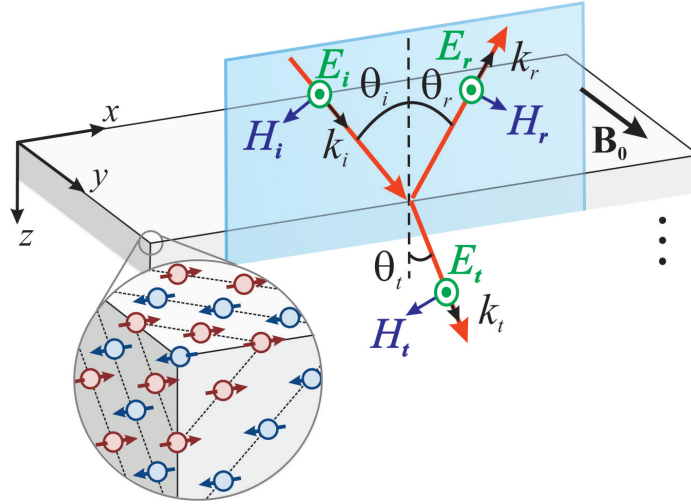


Figure A.1: Reflection geometry. The material occupies the lower half plane, $z > 0$, and the surface is in the xz plane. The saturation magnetisation is along x and the external field \mathbf{B}_0 is perpendicular to both the incidence plane and the easy axis (along y). The angle of incidence, θ_i , is the angle the wavevector of the incident wave makes with the normal to the surface. H_i and H_r represent the incident and reflected magnetic fields, respectively, which are polarized in the xz plane. E_i and E_r represent the incident and reflected electric fields, respectively, which are polarized in the y axis.

\mathbf{B}_0 the permeability tensor given by

$$\overset{\leftrightarrow}{\boldsymbol{\mu}}(\omega) = \begin{pmatrix} \mu_{xx} & 0 & \mu_{xz} \\ 0 & \mu_{xx} & 0 \\ -\mu_{xz} & 0 & \mu_{zz} \end{pmatrix} \quad (\text{A.1})$$

and the dielectric tensor

$$\overset{\leftrightarrow}{\boldsymbol{\varepsilon}}(\omega) = \begin{pmatrix} \varepsilon_{\perp} & 0 & 0 \\ 0 & \varepsilon_{\parallel} & 0 \\ 0 & 0 & \varepsilon_{\perp} \end{pmatrix}. \quad (\text{A.2})$$

The reflectivity as a function of the angle of incidence results from the boundary conditions in the surface ($z = 0$). The boundary conditions require the continuity of the tangential components of \mathbf{E} and \mathbf{H} ,

$$E_{iy} + E_{ry} = E_{ty}, \quad (\text{A.3})$$

$$H_{ix} + H_{rx} = H_{tx}, \quad (\text{A.4})$$

and the normal components \mathbf{B} and \mathbf{D} ,

$$B_{iz} + B_{rz} = B_{tz}, \quad (\text{A.5})$$

$$D_{iz} + D_{rz} = D_{tz}. \quad (\text{A.6})$$

Where i , r and t denote incident, reflected and refracted waves, respectively. The amplitudes of the transmitted and reflected waves can be found in terms of the incident wave. In more general situation when there is rotation of the incidence plane, and hence mixed polarisation modes, or when there are more than one wave propagating in the material (birefringence, corresponding to two k_{2z} 's), there are more than one refracted field inside the crystal. This means that all equations from A.3 to A.6 emanate independent equations.

We consider the simple geometry shown in Fig. A.1, in which the polarisation and resonances lie in the xz plane. In this case, the boundary condition on continuity of normal \mathbf{B} across the interface can be expressed as a linear combination of the boundary condition on tangential \mathbf{E} , so this does not yield any new relations. We, therefore, chose the boundary conditions for the continuity of tangential \mathbf{E} and normal \mathbf{H} , since they are the only independent equations.

Maxwell's equations can be employed in order to obtain the \mathbf{H} fields in terms of \mathbf{E} . For that we use

$$\mathbf{k} \times \mathbf{E} = \mu_0 \mu \omega \mathbf{H}. \quad (\text{A.7})$$

◦ In the first medium, $z \leq 0$ where $\mu = \mu_1$ we make

$$\begin{vmatrix} \hat{i} & \hat{j} & \hat{k} \\ k_{ix} & 0 & k_{iz} \\ 0 & E_{iy} & 0 \end{vmatrix} = \mu_0 \mu_1 \omega \begin{pmatrix} H_{ix} \\ 0 \\ H_{iz} \end{pmatrix}. \quad (\text{A.8})$$

So that the components of \mathbf{H} are given by

$$H_{xi} = \frac{-k_{iz} E_{iy}}{\mu_0 \mu_1 \omega} \quad (\text{A.9}) \quad H_{zi} = \frac{k_{ix} E_{iy}}{\mu_0 \mu_1 \omega} \quad (\text{A.10})$$

◦ In the antiferromagnetic crystal, $z \geq 0$ where $\boldsymbol{\mu} = \overset{\leftrightarrow}{\boldsymbol{\mu}}(\omega)$ we make

$$\begin{vmatrix} \hat{i} & \hat{j} & \hat{k} \\ k_{tx} & 0 & k_{tz} \\ 0 & E_{ty} & 0 \end{vmatrix} = \mu_0 \omega \begin{pmatrix} \mu_{xx} & 0 & \mu_{xz} \\ 0 & \mu_{xx} & 0 \\ -\mu_{xz} & 0 & \mu_{zz} \end{pmatrix} \begin{pmatrix} H_{tx} \\ 0 \\ H_{tz} \end{pmatrix}. \quad (\text{A.11})$$

Here, the components of \mathbf{H} are given as a function of the permeability tensor components, being

$$H_{xt} = \frac{-E_{iy}(k_{tz}\mu_{zz} + k_{tx}\mu_{xz})}{\mu_0\omega(\mu_{xx}\mu_{zz} + \mu_{xz}^2)} \quad (\text{A.12}) \quad H_{zt} = \frac{E_{iy}(k_{tx}\mu_{xx} - k_{tz}\mu_{xz})}{\mu_0\omega(\mu_{xx}\mu_{zz} + \mu_{xz}^2)} \quad (\text{A.13})$$

Furthermore, boundary conditions dictate that k_x value holds both sides of the interface so that $k_{ix} = k_{tx} = k_x$. If we now eliminate in Eq. (A.4) the magnetic field by the electric field according to Eqs. (E.4) and (A.12), we get

$$\frac{-k_{iz}E_{iy}}{\mu_0\mu_1\omega} + \frac{k_{rz}E_{ry}}{\mu_0\mu_1\omega} = \frac{-E_{iy}(k_{tz}\mu_{zz} + k_x\mu_{xz})}{\mu_0\omega(\mu_{xx}\mu_{zz} + \mu_{xz}^2)}, \quad (\text{A.14})$$

rearranging the terms we obtain

$$\frac{E_{ry}}{E_{iy}} + \frac{E_{ty}}{E_{iy}} \frac{(k_{tz}\mu_{zz} + k_x\mu_{xz})}{k_{iz}(\mu_{xx}\mu_{zz} + \mu_{xz}^2)} = 1 \quad (\text{A.15})$$

From Eq. (A.3) we have

$$-\frac{E_{ry}}{E_{iy}} + \frac{E_{ty}}{E_{iy}} = 1 \quad (\text{A.16})$$

Combining Eqs. (A.16) with (A.15) in a matrix form we have

$$\begin{pmatrix} 1 & \frac{(k_{tz}\mu_{zz} + k_x\mu_{xz})}{k_{iz}(\mu_{xx}\mu_{zz} + \mu_{xz}^2)} \\ -1 & 1 \end{pmatrix} \begin{pmatrix} \frac{E_{ry}}{E_{iy}} \\ \frac{E_{ty}}{E_{iy}} \end{pmatrix} = \begin{pmatrix} 1 \\ 1 \end{pmatrix}. \quad (\text{A.17})$$

The complex reflection coefficient r for reflection from an antiferromagnet in the present geometry is therefore given by

$$r = \frac{E_{ry}}{E_{iy}} = \frac{k_{iz}(\mu_{xx}\mu_{zz} + \mu_{xz}^2) - k_{tz}\mu_{zz} - k_x\mu_{xz}}{k_{iz}(\mu_{xx}\mu_{zz} + \mu_{xz}^2) + k_{tz}\mu_{zz} + k_x\mu_{xz}}, \quad (\text{A.18})$$

and the transmission t is

$$t = \frac{E_{ty}}{E_{iy}} = \frac{2k_{iz}(\mu_{xx}\mu_{zz} + \mu_{xz}^2)}{k_{iz}(\mu_{xx}\mu_{zz} + \mu_{xz}^2) + k_{tz}\mu_{zz} + k_x\mu_{xz}}. \quad (\text{A.19})$$

On the Transmission Across an Antiferromagnet Film

In order to analyse optical effects related to transmission of radiation passing through an antiferromagnetic slab, such as negative refraction and focusing, we need to obtain the suitable equations for reflection and transmission considering multiple reflection at the different interfaces.

The boundary conditions here are obtained in a similar manner to that done in Chapter A. The system studied throughout this work is a layered Air/Antiferromagnet/Air such as the one shown in Fig. B.1, which allows an external magnetic field \mathbf{B}_0 perpendicular to the incidence plane and the anisotropy axes. In a layered system, multiple reflections generate partial rays which interfere with one another. Therefore the overall intensities of reflectivity and transmission have to consider their role and it can be calculated using a transfer matrix method [64, 94].

B.1 Boundary Conditions

At the top of each layer all rays can be considered as a single wave, with the variation of the electric fields directed along the y axis, given by E_{nt}^u and E_{nr}^u . We can also represent the equivalent fields E_{ni}^l and E_{nr}^l at the bottom of the layer as depicted in Fig B.1.

From the continuity of \mathbf{E} along y we have to modify Eq. (A.3) since there is a

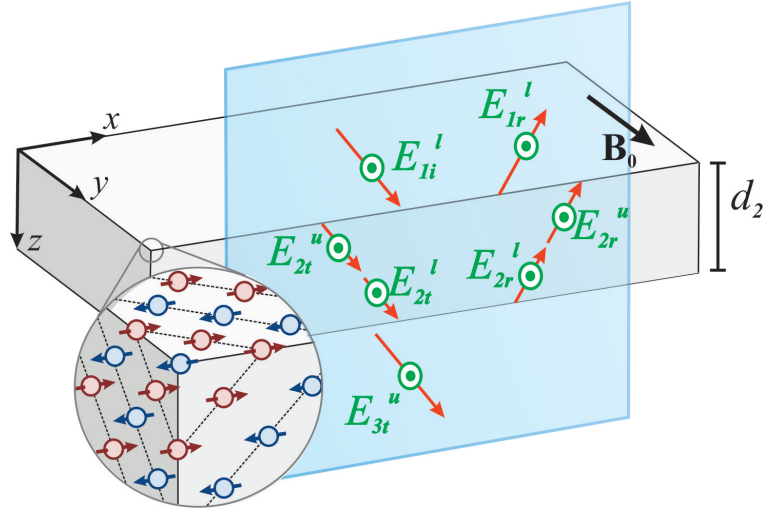


Figure B.1: Reflection geometry. The material occupies the lower half plane, $z > 0$, and the surface is in the xz plane. The saturation magnetisation is along x and the external field \mathbf{B}_0 is perpendicular to both the incidence plane and the easy axis (along y). The angle of incidence, θ_i , is the angle the wavevector of the incident wave makes with the normal to the surface. H_i and H_r represent the incident and reflected magnetic fields, respectively, which are polarized in the xz plane. E_i and E_r represent the incident and reflected electric fields, respectively, which are polarized in the y axis.

reflected wave at the second interface, so that

$$E_{ni}^l + E_{nr}^l = E_{(n+1)t}^u + E_{(n+1)r}^u \quad (\text{B.1})$$

and from the continuity of tangential \mathbf{H} at the first interface we obtain

$$-\frac{k_{z1}}{\mu_0 \omega \mu_1} (E_{1i}^l - E_{1r}^l) = -\frac{\mu_{zz} k_{z2} + \mu_{xz} k_x}{\omega \mu_0 (\mu_{xx} \mu_{zz} - \mu_{xz}^2)} (E_{2t}^u - E_{2r}^u), \quad (\text{B.2})$$

and at the second interface it gives

$$-\frac{\mu_{zz} k_{z2} + \mu_{xz} k_x}{\omega \mu_0 (\mu_{xx} \mu_{zz} - \mu_{xz}^2)} (E_{2t}^l - E_{2r}^l) = -\frac{k_{z1}}{\mu_0 \omega \mu_1} (E_{3i}^u - E_{3r}^u). \quad (\text{B.3})$$

B.2 Transfer Matrix

Here we use Eq. (B.1) in Eq. (B.2) we can isolate E_{1i}^l and E_{r1}^l in terms of E_{2t}^u and E_{r2}^u , and this can be put in a matrix form as follows

$$\begin{pmatrix} E_{1i}^l \\ E_{r1}^l \end{pmatrix} = \underbrace{\begin{pmatrix} \frac{1}{2} + X & \frac{1}{2} - X \\ \frac{1}{2} - X & \frac{1}{2} + X \end{pmatrix}}_{\mathbf{M}_1} \begin{pmatrix} E_{2t}^u \\ E_{r2}^u \end{pmatrix}, \quad (\text{B.4})$$

where X is given, in terms of the wave vectors and permeability tensor components, by

$$X = \frac{\mu_1(k_{2z}\mu_{zz} + k_x\mu_{xz})}{k_{1z}(\mu_{xx}\mu_{zz} + \mu_{xz}^2)}. \quad (\text{B.5})$$

As in the second interface we have now the opposite media structure from the first interface (Antiferromagnet/Air), the matrix is now written as

$$\begin{pmatrix} E_{2i}^l \\ E_{2r}^l \end{pmatrix} = \underbrace{\begin{pmatrix} \frac{1}{2} + X^{-1} & \frac{1}{2} - X^{-1} \\ \frac{1}{2} - X^{-1} & \frac{1}{2} + X^{-1} \end{pmatrix}}_{\mathbf{M}_2} \begin{pmatrix} E_{3t}^u \\ E_{3r}^u \end{pmatrix} \quad (\text{B.6})$$

In the case we are studying here, the antiferromagnetic layer is considered as being finite having thickness d_2 , which can be used to relate the fields at its top and bottom

$$E_{2r}^u = E_{2r}^l e^{-ik_{2z}d_2} \quad (\text{B.7})$$

and

$$E_{2t}^l = E_{2r}^u e^{ik_{2z}d_2} \quad (\text{B.8})$$

In a matrix form this gives

$$\begin{pmatrix} E_{2r}^u \\ E_{2r}^l \end{pmatrix} = \underbrace{\begin{pmatrix} e^{-ik_{2z}d} & 0 \\ 0 & e^{ik_{2z}d} \end{pmatrix}}_{\mathbf{F}} \begin{pmatrix} E_{2r}^l \\ E_{2r}^u \end{pmatrix}. \quad (\text{B.9})$$

In this case, however, the third layer is semi-infinite, i.e. $E_{3r}^t = 0$ since there is only transmission in this layer.

The three matrices above can be multiplied together over the structure relating all the fields presents in this system as sown bellow

$$\begin{pmatrix} E_{1i}^l \\ E_{1r}^l \end{pmatrix} = \mathbf{M}_2 \times \mathbf{F} \times \mathbf{M}_1 \begin{pmatrix} E_{3t}^u \\ 0 \end{pmatrix}. \quad (\text{B.10})$$

Since there's no upward wave propagating in the last layer ($n = 3$) the overall matrix may be express in the form

$$\begin{pmatrix} E_{1i}^l \\ E_{1r}^l \end{pmatrix} = \underbrace{\begin{pmatrix} r_{11} & r_{12} \\ r_{21} & r_{22} \end{pmatrix}}_{\mathbf{R}} \begin{pmatrix} E_{3t}^u \\ 0 \end{pmatrix}, \quad (\text{B.11})$$

where \mathbf{R} is a matrix resulting from the multiplication of all matrices across the system and its components can be related to find the reflectivity coefficient as being

$$r = \frac{r_{21}}{r_{11}}. \quad (\text{B.12})$$

and the transmission

$$t = \frac{1}{r_{11}}. \quad (\text{B.13})$$

On the Parameters used

The antiferromagnetic ordering of spins appears in MnF_2 at temperatures below its Néel temperature $T_N = 67$ K, with a zero field resonance frequency ω_0 given by Eq. 2.9. In this work, we have used the field parameters reported by Remer et al. [66], i.e. $B_A = 0.787$ T, $B_E = 55.0$ T, who also report $M_s = 6.0 \times 10^5$ A/m and $\varepsilon = 5.5$.

Within the temperature range considered here, the variation in the resonance frequency ω_0 is fairly small. Therefore, for simplicity, we just model it as a change in the gyromagnetic ratio γ . Thus, at a temperature of $0.06T_N$, we have $\gamma/2\pi c = 0.928$ cm^{-1}/T , corresponding to a resonance frequency of $\omega_0/2\pi c = 8.67$ cm^{-1} , whereas at a temperature of $0.42T_N$ we have $\gamma/2\pi c = 0.877$ cm^{-1}/T , corresponding to a resonance frequency of $\omega_0/2\pi c = 8.19$ cm^{-1} . The corresponding damping parameters used here are [66] $\Gamma/\omega_0 = 8 \times 10^{-5}$ at $0.06T_N$ and $\Gamma/\omega_0 = 6.5 \times 10^{-4}$ at $0.42T_N$.

On the Intensity profile Claculations

In order to analyse the behaviour of electromagnetic waves propagating or (and) reflecting through an antiferromagnetic crystal it is useful to look at the behaviour of a finite beam. We construct a Gaussian beam incident upon an antiferromagnetic surface, either semi-infinite crystal or finite slab, using analytical solutions of the electric field inside and outside the material. By studying the distribution of the time-averaged flow on the interface where the reflected Gaussian beam emerges, we can describe quantitatively the amount of lateral displacement of the beam position. using the same approach, we can also determine the behaviour of the propagating wave, which may be negatively refracted.

D.1 Semi-infinite crystal

In the case of reflection of a finite beam, we can base our analysis on plane wave reflection by considering such a beam as a sum of plane waves. In this approach, we consider the electric field (directed along y) associated with the incident beam as a Fourier sum of plane waves in the form

$$E_i(x, z) = \int_{-k_0}^{k_0} \psi(k_x) e^{i(k_x x + k_{1z} z)} dk_x, \quad (\text{D.1})$$

where $k_0 = \omega/c$, k_x is the in-plane component of the wavevector associated with a particular plane wave and $\psi(k_x)$ is the Gaussian spectrum which carries the information on the shape of the beam centered at $x = 0$ and $z = 0$ and is given

by [95, 45, 49]

$$\psi(k_x) = -\frac{g}{2 \cos \theta_1 \sqrt{\pi}} \exp \left[-\frac{g^2 (k_x - k_0 \sin \theta_1)^2}{4 \cos^2 \theta_1} \right]. \quad (\text{D.2})$$

Here $2g$ represents the beam width at its waist and θ_1 the incident angle of the central plane wave.

The electric field distribution the incident beam at the surface, which we define to be at $z = 0$, is given by

$$E_i(x, 0) = \int_{-k_0}^{+k_0} \psi(k_x) e^{ik_x x} dk_x, \quad (\text{D.3})$$

and the electric field distribution of the corresponding reflected beam at the surface is

$$E_r(x, 0) = \int_{-k_0}^{+k_0} r(k_x) \psi(k_x) e^{ik_x x} dk_x. \quad (\text{D.4})$$

$r(k_x)$ represents the complex reflection coefficient, which we can represent as

$$r(k_x) = \rho(k_x) e^{i\phi(k_x)}, \quad (\text{D.5})$$

where $\rho(k_x)$ is the reflection amplitude and $\phi(k_x)$ is the associated phase change on reflection.

D.2 Finite slab

When travelling through a slab as proposed in Chapter 5, the fields have to be separated for each of the three distinct layers n , and can be represented as

$$E_{ty} = \int_{-\infty}^{\infty} E_{nt}(k_x) e^{ik_{nz}z} e^{ik_x x} dk_x, \quad (\text{D.6})$$

$$E_{ry} = \int_{-\infty}^{\infty} E_{nr}(k_x) e^{-ik_{nz}z} e^{ik_x x} dk_x, \quad (\text{D.7})$$

The coefficients E_{nt} and E_{nr} are for radiation propagating in the direction of increasing and decreasing z respectively. In the first layer ($z < 0$ and $n = 1$),

which is the layer at which the radiation is incident we have

$$E_{1i} = \psi(k_x) \quad (\text{D.8})$$

and

$$E_{1r} = r(k_x)\psi(k_x) \quad (\text{D.9})$$

where $r(k_x)$ is given by Eq. (B.12).

In addition, there is no propagation in the negative z direction in the final layer, so we can make

$$E_{3t} = t(k_x)\psi(k_x), \quad (\text{D.10})$$

where $t(k_x)$ is given by Eq. (B.13).

$$E_{3r} = 0 \quad (\text{D.11})$$

The other coefficients for $n = 2$ are obtained using standard transfer matrix techniques in a manner as described in Chapter A.

When simulating a Gaussian beam travelling through an antiferromagnetic slab we simply replace $\psi(k_x)$ by the one given by Eq. (3.11).

D.2.1 Line point source

In order to model focusing in an antiferromagnet as shown in Chapter 5 a source radiating in all directions in the xz plane must be used. In order to achieve this, we consider an oscillating line of electric current I directed along the y axis placed at $x = 0$ and $z = 0$. The analysis is essentially the same as that used for the Gaussian beam as described previously, but with $\psi(k_x)$ now given by

$$\psi(k_x) = \frac{\omega\mu_0 I}{4\pi k_{1z}}. \quad (\text{D.12})$$

D.2.2 Goos-Hänchen shift on reflection of a finite beam

In the case of reflection of a finite beam, we can still base our analysis on plane wave reflection by considering such a beam as a sum of plane waves. Such a plane wave spectrum approach has been usefully applied to analyzing Goos-Hänchen shifts by McGuirk and Carniglia [22]. Here we summarize the resulting theory for application to the present case.

In this approach, we consider the electric field (directed along y) associated with the incident beam as a Fourier sum of plane waves in the form

$$E_i(x, z) = \int_{-k_0}^{k_0} \psi(k_x) e^{i(k_x x + k_{1z} z)} dk_x, \quad (\text{D.13})$$

where k_x is the in-plane component of the wavevector associated with a particular plane wave and $\psi(k_x)$ is a distribution function representing the shape of the beam. The electric field distribution of the incident beam at the surface, which we define to be at $z = 0$, is given by

$$E_i(x, 0) = \int_{-k_0}^{+k_0} \psi(k_x) e^{ik_x x} dk_x, \quad (\text{D.14})$$

and the electric field distribution of the corresponding reflected beam at the surface is

$$E_r(x, 0) = \int_{-k_0}^{+k_0} r(k_x) \psi(k_x) e^{ik_x x} dk_x. \quad (\text{D.15})$$

$r(k_x)$ represents the complex reflection coefficient, which we can represent as

$$r(k_x) = \rho(k_x) e^{i\phi(k_x)}, \quad (\text{D.16})$$

where $\rho(k_x)$ is the reflection amplitude and $\phi(k_x)$ is the associated phase change on reflection. If this phase change varies with k_x , interference between the reflected plane waves will be different from that for the incident waves, leading to a change in the reflected beam profile. This typically manifests itself as a lateral shift of the reflected beam [29, 22, 21] associated with derivative of $\phi(k_x)$. To see this, consider a wide beam. In this case, k_x assumes a narrow range of values centred around $k_x = k_{x0}$, where $k_{x0} = k_0 \sin \theta_1$, the angle θ_1 being the effective

incident angle of the overall beam. If we now expand ρ and ϕ as a Taylor series around $k_x = k_{x0}$, Eq. (D.15) can be approximated to

$$E_r(x) = r(k_{x0}) \int_{-k_0}^{+k_0} \psi(k_x) \exp \left[k_x \left(x + \frac{d\phi}{dk_x} \Big|_{k_x=k_{x0}} \right) \right] dk_x, \quad (\text{D.17})$$

where $r(k_{x0})$ is the reflection coefficient of a plane wave whose angle of incidence is θ_1 . The integral representing the profile of the reflected beam in Eq. (D.17) is the same as that for the incident beam in Eq. (D.14) except that x has been replaced by $x + D$. Thus the reflected beam has, in effect, been shifted along the surface by a distance D , given by

$$D = - \frac{d\phi}{dk_x} \Big|_{k_x=k_{x0}}. \quad (\text{D.18})$$

On the Power Flow

Electromagnetic waves propagate through a given medium as a combination of interpenetrating electric and magnetic fields with similar energies. The flux of electromagnetic power is therefore calculated as a combination of both these fields and can be described by the Poynting vector equation

$$\mathbf{S} = \mathbf{E} \times \mathbf{H}, \quad (\text{E.1})$$

where \mathbf{E} and \mathbf{H} are the electric and magnetic fields respectively.

The Poynting vector gives a variety of information about the behaviour of propagating electromagnetic waves including the direction of propagation. Throughout this work, it is considered plane waves transporting energy so that the instantaneous value of the power flow is given by the time averaged Poynting vector $\langle \mathbf{S} \rangle$ of \mathbf{S} at a given time.

In order to analyse the behaviour of propagating waves at an interface between air and an antiferromagnetic crystal is therefore necessary to solve Eq. (E.1) for both media. It is useful to start by doing the cross product

$$\mathbf{E} \times \mathbf{H} = \begin{vmatrix} \hat{i} & \hat{j} & \hat{k} \\ 0 & E_y & 0 \\ H_y & 0 & H_z \end{vmatrix}. \quad (\text{E.2})$$

This yields

$$\mathbf{S} = \hat{i}E_yH_z - \hat{k}E_yH_x \quad (\text{E.3})$$

with components

$$S_x = E_y H_z \quad (\text{E.4}) \quad S_z = -E_y H_x. \quad (\text{E.5})$$

Inside the antiferromagnet, the components of \mathbf{H} have to be replaced as to include the components of the dynamic permeability tensor. These components have been derived in Appendix A are give by Eqs. (A.12) and (A.13), in the general case where an external applied field \mathbf{B}_0 is considered, and the final components for the time averaged power flow are given by

$$\langle S_{2x} \rangle = \frac{|E_y|^2}{2\omega\mu_0} \text{Re} \left(\frac{k_x \mu_{xx} - k_{2z} \mu_{xz}}{\mu_{xx} \mu_{zz} + \mu_{xz}^2} \right), \quad (\text{E.6})$$

$$\langle S_{2y} \rangle = 0, \quad (\text{E.7})$$

$$\langle S_{2z} \rangle = \frac{|E_y|^2}{2\omega\mu_0} \text{Re} \left(\frac{k_{2z} \mu_{zz} + k_x \mu_{xz}}{\mu_{xx} \mu_{zz} + \mu_{xz}^2} \right) \quad (\text{E.8})$$

Bibliography

- [1] S. L. Chuang. *Physics of Photonic Devices, 2nd Edition*. Springer-Verlag, New Jersey, US, 2009.
- [2] Eugene Hecht. *Optics*. Addison-Wesley, Reading, Massachusetts, second edition, 1987.
- [3] D. R. Smith, W. J. Padilla, D. C. Vier, S. C. Nemat-Nasser, and S. Schultz. Composite medium with simultaneously negative permeability and permittivity. *Phys. Rev. Lett.*, 84:4184, 2000.
- [4] R. A. Shelby, D. R. Smith, and S. Schultz. Experimental verification of a negative index of refraction. *Science*, 292:77–79, apr 2001.
- [5] Vladimir M. Shalaev, Wenshan Cai, Uday K. Chettiar, Hsiao-Kuan Yuan, Andrey K. Sarychev, Vladimir P. Drachev, and Alexander V. Kildishev. Negative index of refraction in optical metamaterials. *Opt. Lett.*, 30(24):3356–3358, Dec 2005.
- [6] Vladimir M. Shalaev. Optical negative-index metamaterials. *Nature Photonics*, 1(1):41–48, JAN 2007.
- [7] O. F. Siddiqui, M. Mojahedi, and G. V. Eleftheriades. Periodically loaded transmission line with effective negative refractive index and negative group velocity. *IEEE Transactions on Antennas and Propagation*, 51(10):2619–2625, Oct 2003.
- [8] V. G. Veselago. The electrodynamics of substances with simultaneously negative values of ϵ and μ . *Sov. Phys. Usp.*, 10(4):509–514, 1968.
- [9] Michio Kaku. *Physics of the Impossible: A scientific Exploration Into the World of Phasers, Force Fields, Teleportation and Time Travel*. Doubleday Publishing, London, parallel worlds edition, 2008.

- [10] WenXuan Tang, ZhongLei Mei, and TieJun Cui. Theory, experiment and applications of metamaterials. *Science China Physics, Mechanics & Astronomy*, 58(12):1–11, 2015.
- [11] D. Schurig, J. J. Mock, B. J. Justice, S. A. Cummer, J. B. Pendry, A. F. Starr, and D. R. Smith. Metamaterial electromagnetic cloak at microwave frequencies. *Science*, 314(5801):977–980, 2006.
- [12] Y. Zhou, X. Y. Chen, Y. H. Fu, G. Vienne, A. I. Kuznetsov, and B. Luk'yanchuk. Fabrication of large-area 3d optical fishnet metamaterial by laser interference lithography. *Applied Physics Letters*, 103(12), 2013.
- [13] Z. Duan, F. Wang, X. Tang, Y. Wang, Y. Gong, and M. Chen. Overview of vacuum electron devices for biomedical applications. In *RF and Wireless Technologies for Biomedical and Healthcare Applications (IMWS-BIO), 2015 IEEE MTT-S 2015 International Microwave Workshop Series on*, pages 156–157, Sept 2015.
- [14] Prashant Shekhar, Jonathan Atkinson, and Zubin Jacob. Hyperbolic metamaterials: fundamentals and applications. *Nano Convergence*, 1(1):1–17, 2014.
- [15] Anthony J. Hoffman, Leonid Alekseyev, Scott S. Howard, Kale J. Franz, Dan Wasserman, Viktor A. Podolskiy, Evgenii E. Narimanov, Deborah L. Sivco, and Claire Gmachl. Negative refraction in semiconductor metamaterials. *Nature Materials*, 6(12):946–950, DEC 2007.
- [16] A. Poddubny, I. Iorsh, P. Belov, and Y. Kivshar. Hyperbolic metamaterials. *Nat Photon*, 7:948–957, Nov 2013.
- [17] David R. Smith and David Schurig. Electromagnetic wave propagation in media with indefinite permittivity and permeability tensors. *Phys. Rev. Lett.*, 90(7):077405, feb 2003.
- [18] Lorenzo Ferrari, Chihhui Wu, Dominic Lepage, Xiang Zhang, and Zhaowei Liu. Hyperbolic metamaterials and their applications. *Progress in Quantum Electronics*, 40:1 – 40, 2015.

- [19] David R. Smith, David Schurig, Marshall Rosenbluth, Sheldon Schultz, S. Anantha Ramakrishna, and John B. Pendry. Limitations on subdiffraction imaging with a negative refractive index slab. *Appl. Phys. Lett.*, 82(10):1506–1508, mar 2003.
- [20] F. Goos and H. Hänchen. Ein neuer und fundamentaler versuch zur totalreflexion. *Ann. Physik*, 436(6):333–346, 1947.
- [21] K. Artmann. Berechnung der seitenversetzung des totalreflektierten strahles. *Ann. Physik*, 437:87–102, 1948.
- [22] M. McGuirk and C. K. Carniglia. An angular spectrum representation approach to the Goos-Hänchen shift. *J. Opt. Soc. Am.*, 67(1):103–107, jan 1977.
- [23] Walter J. Wild and C. Lee Giles. Goos-Hänchen shifts from absorbing media. *Phys. Rev. A*, 25(4):2099–2101, apr 1982.
- [24] P. T. Leung, Z. W. Chen, and H.-P. Chiang. Large negative Goos-Hänchen shift at metal surfaces. *Opt. Commun.*, 276(2):206–208, aug 2007.
- [25] M. Merano, A. Aiello, G. W. 't Hooft, M. P. van Exter, E. R. Eliel, and J. P. Woerdman. Observation of Goos-Hänchen shifts in metallic reflection. *Opt. Express*, 15(24):15928, 2007.
- [26] T. Tamir and H. L. Bertoni. Lateral displacement of optical beams at multilayered and periodic structures. *J. Opt. Soc. Am.*, 61(10):1397–1413, Oct 1971.
- [27] R Macêdo and T Dumelow. Beam shifts on reflection of electromagnetic radiation off anisotropic crystals at optic phonon frequencies. *Journal of Optics*, 15(1):014013, 2013.
- [28] F. Lima, T. Dumelow, J. A. P. da Costa, and E. L. Albuquerque. Lateral shift on normal incidence reflection off an antiferromagnet. *Europhys. Lett.*, 83(1):17003, july 2008.
- [29] F. Lima, T. Dumelow, E. L. Albuquerque, and J. A. P. da Costa. Power flow associated with the Goos-Hänchen shift of a normally incident electromagnetic beam reflected off an antiferromagnet. *Phys. Rev. B*, 79(15):155124, 2009.

- [30] F. Lima, T. Dumelow, E. L. Albuquerque, and J. A. P. da Costa. Non-reciprocity in the Goos-Hänchen shift on oblique incidence reflection off antiferromagnets. *J. Opt. Soc. Am. B*, 28(2):306–313, Feb 2011.
- [31] Thomas Dumelow, José Alzimir Pereira da Costa, and Valder Nogueira Freire. Slab lenses from simple anisotropic media. *Phys. Rev. B*, 72:235115, Dec 2005.
- [32] J. B. Pendry. Negative refraction makes a perfect lens. *Phys. Rev. Lett.*, 85(18):3966–3969, oct 2000.
- [33] B. Wood, J. B. Pendry, and D. P. Tsai. Directed subwavelength imaging using a layered metal-dielectric system. *Phys. Rev. B*, 74:115116, Sep 2006.
- [34] P. West, S. Ishii, G. Naik, N. Emani, V.M. Shalaev, and Alexandra Boltasseva. Searching for better plasmonic materials. *Laser & Photonics Reviews*, 4(6):795–808, 2010. Featured on materials science news site materialsViews.com 2010-10-21, Laser & PHoton.Rev. 4(6)/2010 Cover.
- [35] Harish N. S. Krishnamoorthy, Zubin Jacob, Evgenii Narimanov, Ilona Kretzschmar, and Vinod M. Menon. Topological transitions in metamaterials. *Science*, 336(6078):205–209, 2012.
- [36] Nader Engheta. Pursuing near-zero response. *Science*, 340(6130):286–287, 2013.
- [37] Pavel A. Belov and Yang Hao. Subwavelength imaging at optical frequencies using a transmission device formed by a periodic layered metal-dielectric structure operating in the canalization regime. *Phys. Rev. B*, 73:113110, Mar 2006.
- [38] Pavel A. Belov, Yang Hao, and Sunil Sudhakaran. Subwavelength microwave imaging using an array of parallel conducting wires as a lens. *Phys. Rev. B*, 73:033108, Jan 2006.
- [39] Boardman, Allan D., Egan, Peter, and McCall, Martin. Optic axis-driven new horizons for hyperbolic metamaterials. *EPJ Applied Metamaterials*, 2:11, 2015.

- [40] Karolina Korzeb, Marcin Gajc, and Dorota Anna Pawlak. Compendium of natural hyperbolic materials. *Opt. Express*, 23(20):25406–25424, Oct 2015.
- [41] R. Rodrigues da Silva, R. Macêdo da Silva, T. Dumelow, J. A. P. da Costa, S. B. Honorato, and A. P. Ayala. Using phonon resonances as a route to all-angle negative refraction in the far-infrared region: The case of crystal quartz. *Phys. Rev. Lett.*, 105(16):163903, Oct 2010.
- [42] R. Estevâm da Silva, R. Macêdo, T. Dumelow, J. A. P. da Costa, S. B. Honorato, and A. P. Ayala. Far-infrared slab lensing and subwavelength imaging in crystal quartz. *Phys. Rev. B*, 86:155152, Oct 2012.
- [43] Noritaka Kuroda, Koichi Tsugawa, and Hiroyuki Yokoi. Negative refraction of infrared waves and rays in sapphire α - Al_2O_3 . *Journal of the Physical Society of Japan*, 81(11):114706, 2012.
- [44] V. Dvorak and P. Kuzel. Negative index of refraction in anisotropic nonmagnetic materials. *Ferroelectrics*, 338:195–203, 2006.
- [45] R. Macêdo, R. Rodrigues da Silva, T. Dumelow, and J. A. P. da Costa. MgF_2 as a material exhibiting all-angle negative refraction and subwavelength imaging due to the phonon response in the far infrared. *Optics Communications*, 310(0):94 – 99, 2014.
- [46] D. L. Mills and E. Burstein. Polaritons: the electromagnetic modes of media. *Rep. Prog. Phys.*, 37(7):817–926, jul 1974.
- [47] Front matter. In Eudencilson L. Albuquerque and Michael G. Cottam, editors, *Polaritons in Periodic and Quasiperiodic Structures*, pages iii –. Elsevier Science, Amsterdam, 2004.
- [48] Nathan Marcuvitz Leopold B. Felsen. *Radiation and Scattering of Waves*. Wiley-IEEE Press, New Jersey, 1973.
- [49] R. Macêdo and T. Dumelow. Tunable all-angle negative refraction using antiferromagnets. *Phys. Rev. B*, 89:035135, Jan 2014.

- [50] Allan H. Morrish. *The Physical Principles of Magnetism*. Wiley-IEEE Press, Canada, 1965.
- [51] Simon Foner. High-field antiferromagnetic resonance in Cr_2O_3 . *Phys. Rev.*, 130:183–197, Apr 1963.
- [52] Fred M. Johnson and Arthur H. Nethercot. Antiferromagnetic resonance in MnF_2 . *Phys. Rev.*, 114:705–716, May 1959.
- [53] Kamsul Abraha and David R. Tilley. Theory of far infrared properties of magnetic surfaces, films and superlattices. *Surf. Sci. Rep.*, 24(5-6):129–222, 1996.
- [54] Michael G. Cottam, editor. *Linear and Nonlinear Spin Waves in Magnetic Films and Superlattices*. World Scientific, Singapore, 1994.
- [55] D Bloor and D H Martin. Antiferromagnetic resonance in the extreme infra-red. *Phys. Soc. Proc.*, 78(5):774, 1961.
- [56] Charles Kittel. *Introduction to Solid State Physics*. John Wiley & Sons, Inc., New York, 6th edition, 1986.
- [57] Simon Foner. 9 - antiferromagnetic and ferrimagnetic resonance. In George T. Rado and Harry Suhl, editors, *Magnetism*, pages 383 – 447. Academic Press, 1963.
- [58] C. Kittel. Theory of antiferromagnetic resonance. *Phys. Rev.*, 82:565–565, May 1951.
- [59] Takeo Nagamiya. Theory of antiferromagnetism and antiferromagnetic resonance absorption, ii. *Progress of Theoretical Physics*, 6(3):350–355, 1951.
- [60] N. S. Almeida and D. L. Mills. Dynamical response of antiferromagnets in an oblique magnetic field: Application to surface magnons. *Phys. Rev. B*, 37(7):3400–3408, Mar 1988.
- [61] R. E. Camley and D. L. Mills. Surface polaritons on uniaxial antiferromagnets. *Phys. Rev. B*, 26:1280–1287, 1982.

- [62] Robert E. Camley. Nonreciprocal surface waves. *Surf. Sci. Rep.*, 7(3-4):103–188, jul 1987.
- [63] R. L. Stamps, B. L. Johnson, and Robert E. Camley. Nonreciprocal reflection from semi-infinite antiferromagnets. *Phys. Rev. B*, 43(4):3626–3636, feb 1991.
- [64] Thomas Dumelow and Robert E. Camley. Nonreciprocal reflection of infrared radiation from structures with antiferromagnets and dielectrics. *Phys. Rev. B*, 54(17):12232–12237, nov 1996.
- [65] Thomas Dumelow, Robert E. Camley, Kamsul Abraha, and David R. Tilley. Nonreciprocal phase behavior in reflection of electromagnetic waves from magnetic materials. *Phys. Rev. B*, 58(2):897–908, jul 1998.
- [66] L. Remer, B. Lüthi, H. Sauer, R. Geick, and R. E. Camley. Nonreciprocal optical reflection of the uniaxial antiferromagnet MnF_2 . *Phys. Rev. Lett.*, 56(25):2752–2754, jun 1986.
- [67] Douglas E. Brown, Thomas Dumelow, Terence J. Parker, Kamsul Abraha, and David R. Tilley. Nonreciprocal reflection by magnons in FeF_2 : a high resolution study. *Phys. Rev. B*, 49(17):12266–12269, may 1994.
- [68] Kamsul Abraha, Douglas E. Brown, Thomas Dumelow, Terence J. Parker, and David R. Tilley. Oblique incidence far-infrared reflectivity study of the uniaxial antiferromagnet FeF_2 . *Phys. Rev. B*, 50(10):6808–6816, sep 1994.
- [69] Morten R. F. Jensen, Terence J. Parker, Kamsul Abraha, and David R. Tilley. Experimental observation of magnetic surface polaritons in FeF_2 by attenuated total reflection. *Phys. Rev. Lett.*, 75(20):3756–3759, nov 1995.
- [70] H. M. Lai, S. W. Chan, and W. H. Wong. Nonspecular effects on reflection from absorbing media at and around Brewster's dip. *J. Opt. Soc. Am. A*, 23(12):3208–3216, Dec 2006.
- [71] J. B. Götte, A. Aiello, and J. P. Woerdman. Loss-induced transition of the Goos-Hänchen effect for metals and dielectrics. *Opt. Express*, 16(6):3961–3969, mar 2008.

- [72] O. Ivanov and D. Sementsov. Negative shift of a light beam reflected from the interface between optically transparent and resonant media. *Optics and Spectroscopy*, 89:737–741, 2000.
- [73] Rui Wang, Jingbo Sun, and Ji Zhou. Indefinite permittivity in uniaxial single crystal at infrared frequency. *Appl. Phys. Lett.*, 97(3):031912, 2010.
- [74] I. V. Lindell, S. A. Tretyakov, K. I. Nikoskinen, and S. Ilvonen. Bw media with negative parameters, capable of supporting backward waves. *Microwave and Optical Technology Letters*, 31(2):129–133, 2001.
- [75] D. R. Smith, J. B. Pendry, and M. C. K. Wiltshire. Metamaterials and negative refractive index. *Science*, 305(5685):788–792, 2004.
- [76] Xudong Wang, Yong-Hong Ye, Chao Zheng, Yao Qin, and Tie Jun Cui. Tunable figure of merit for a negative-index metamaterial with a sandwich configuration. *Opt. Lett.*, 34(22):3568–3570, Nov 2009.
- [77] Mohamed A. K. Othman, Caner Guclu, and Filippo Capolino. Graphene-based tunable hyperbolic metamaterials and enhanced near-field absorption. *Opt. Express*, 21(6):7614–7632, Mar 2013.
- [78] Chuwen Lan, Ke Bi, Ji Zhou, and Bo Li. Experimental demonstration of hyperbolic property in conventional material–ferrite. *Appl. Phys. Lett.*, 107(21), 2015.
- [79] S Anantha Ramakrishna. Physics of negative refractive index materials. *Rep. on Progr. in Phys.*, 68(2):449, 2005.
- [80] J. B. Pendry, A. J. Holden, D. J. Robbins, and W. J. Stewart. Magnetism from conductors and enhanced nonlinear phenomena. *IEEE Trans. Microwave Theory Tech.*, 47:2075, 1999.
- [81] Jie Yao, Kun-Tong Tsai, Yuan Wang, Zhaowei Liu, Guy Bartal, Yuh-Lin Wang, and Xiang Zhang. Imaging visible light using anisotropic metamaterial slab lens. *Opt. Express*, 17(25):22380–22385, Dec 2009.

- [82] Jessica Bénédicte, Emmanuel Centeno, and Antoine Moreau. Lens equation for flat lenses made with hyperbolic metamaterials. *Opt. Lett.*, 37(22):4786–4788, Nov 2012.
- [83] J F Nye. *Natural Focusing and Fine Structure of Light: Caustics and Wave Dislocations*. Institute of Physics Publishing: Bristol and Philadelphia, 1999.
- [84] K. J. Webb and M. Yang. Subwavelength imaging with a multilayer silver film structure. *Opt. Lett.*, 31(14):2130–2132, Jul 2006.
- [85] Erasmus Bartholin. *Experimenta crystalli islandici disdiacastici quibus mira & insolita refractio detegitur*. Hafniae: Paulli, Denmark, landmarks of science edition, 1969.
- [86] Yongmin Liu, Guy Bartal, and Xiang Zhang. All-angle negative refraction and imaging in a bulk medium made of metallic nanowires in the visible region. *Opt. Express*, 16(20):15439–15448, 2008.
- [87] Xuan Li, Sailing He, and Yi Jin. Subwavelength focusing with a multilayered fabry-perot structure at optical frequencies. *Phys. Rev. B*, 75:045103, Jan 2007.
- [88] Igor S. Nefedov, Constantinos A. Valagiannopoulos, Seed M. Hashemi, and Evgeny I. Nefedov. Total absorption in asymmetric hyperbolic media. *Scientific Reports*, 3:2662, oct 2013.
- [89] S. M. Hashemi and I. S. Nefedov. Wideband perfect absorption in arrays of tilted carbon nanotubes. *Phys. Rev. B*, 86:195411, Nov 2012.
- [90] I. Nefedov and L. Melnikov. Asymmetric hyperbolic metamaterials and their applications for light absorption and amplification. In *2015 17th International Conference on Transparent Optical Networks (ICTON)*, pages 1–3, July 2015.
- [91] Ayed Al Sayem, M R C Mahdy, and Md Saifur Rahman. Broad angle negative refraction in lossless all dielectric or semiconductor based asymmetric anisotropic metamaterial. *Journal of Optics*, 18(1):015101, 2016.
- [92] Huikan Liu, Shivanand, and Kevin J. Webb. Subwavelength imaging opportunities with planar uniaxial anisotropic lenses. *Opt. Lett.*, 33(21):2568–2570, Nov 2008.

- [93] Joshua D Caldwell et al. Sub-diffractive volume-confined polaritons in the natural hyperbolic material hexagonal boron nitride. *Nature Commun.*, 5(5221):5221, 2014.
- [94] Thomas Dumelow and David R. Tilley. Optical properties of semiconductor superlattices in the far infrared. *J. Opt. Soc. Am. A*, 10:633–645, apr 1993.
- [95] Jin Au Kong, Bae-Ian Wu, and Yan Zhang. Lateral displacement of a gaussian beam reflected from a grounded slab with negative permittivity and permeability. *Appl. Phys. Lett.*, 80(12):2084–2086, mar 2002.